January 2021

An Investigation Of Uncertainties In Intensity Modulated Radiation Therapy

Cory Knill
Wayne State University

AN INVESTIGATION OF UNCERTAINTIES IN INTENSITY MODULATED RADIATION THERAPY

by

CORY KNILL

DISSERTATION

Submitted to the Graduate School

of Wayne State University,

Detroit, Michigan

in partial fulfillment of the requirements

for the degree of

DOCTOR OF PHILOSOPHY

2021

MAJOR: MEDICAL PHYSICS

Approved By:

_____

Advisor Date

_____

_____

_____

_____

DEDICATION

When I was in grade 2, my father gave a presentation to my class where he described the three conditions necessary for fire: heat, fuel, and oxygen. Scientific passion, like fire, requires the basic knowledge and curiosity to fuel exploration, an idea that sparks an investigation, and the burning passion to see the investigation through. From an early age I benefited from a family that fueled my scientific vigor. From my Dad who set the scientific standard that I sought to attain. My Mom who unapologetically pursued advanced opportunities for me (that often led to delicious polish sausage as well). And my brothers, who's constant arguing amongst the siblings (often time on topics we knew nothing about), led to our quick thinking and analytical minds.

My family created the fuel that only needed a spark, which came from a question posed by a high school physics teacher, Ms. Deyo. The question was simple, which ball would get to the end first: 1) a ball rolling down a straight ramp, 2) a ball rolling down a ramp that had a depression in the middle that came up to meet the original ramp for the final length of the run. Every student had to collectively discuss and solve the problem and then one student would be selected to explain the solution to Ms. Deyo and field any questions she had. Everyone's grade depended on the one student's answer. I was picked, the spark was lit, and my passion for physics began to burn.

Throughout my career, the passion has continued to grow, supported by friends, family, and colleagues who challenged and accompanied me along this great journey of exploration. I am forever grateful for those who have helped and struggled with me along the way. I look back fondly on our shared experiences that have led me to this point and anxiously await our exciting scientific endeavors in the years to come.

ACKNOWLEDGMENTS

I would like to thank my research committee for their guidance and thoughtful discussions throughout my PhD work. I would also like to thank all my research collaborators, whose skills, effort, and expertise greatly enhanced the PhD research. I would like to thank my family, whose support has kept me motivated throughout the PhD process. Finally, I would like to thank my loving wife Annie, and my kids Jack and Aidy, whose constant smiles and love provided the much-needed levity during the drafting of this thesis.

TABLE OF CONTENTS

Dedication……ii

Acknowledgments……iii

List of Tables……v

List of Figures……vii

CHAPTER 1 INTRODUCTION……1

CHAPTER 2 RADIATION-IMAGING COINCIDENCE OPTIMIZATION ON A VERSA HD……18

CHAPTER 3 AN ANALYSIS OF CONFIDENCE LIMITS USED IN AAPM TASK GROUP NO. 119……32

CHAPTER 4 IMRT QA MEASUREMENTS – PTW's 1000 SRS……44

CHAPTER 5 IMRT QA ANALYSIS – INCLUDING STRUCTURES IN GAMMA INDEX CALCULATIONS……63

CHAPTER 6 SINGLE-ISOCENTER MULTI-TARGET IMRT CRANIAL SRS COMMISSIONING……88

CHAPTER 7 CONCLUSION……109

APPENDIX A Computer Coding in Medical Physics……116

REFERENCES……125

ABSTRACT……138

AUTOBIOGRAPHICAL STATEMENT……139

LIST OF TABLES

Table 1: WL results showing the linac isocenter coincidence across all energies, coincidence between the couch rotation axis and linac isocenter, and overall radiation-imaging coincidence for all gantry, collimator, and couch angles. 28

Table 2: Tolerance A: Easily achievable on all Versa HDs. Tolerance B: lower expected limit of what is achievable. 31

Table 3: Three distributions were fitted to gamma index pass rate data for 111 Head and Neck IMRT QAs. Confidence limits were calculated for each distribution and Kolmogorov-Smirnov goodness-of-fit tests were performed. 39

Table 4: Changes in gamma pass rates from complex ion recombination corrections. The average (Avg.), standard deviation (σ), and maximum (Max.) changes were calculated from the per-plan changes in pass rates. 55

Table 5: Comparison of the 3D gamma pass rate results obtained after simple and complex ion recombination corrections. The average (Avg.), standard deviation (σ), and maximum (Max.) changes were calculated from the absolute values of per-arc changes in pass rates. 55

Table 6: Changes made to MLC and beam penumbras to create the modified treatment machines. 65

Table 7: Various parameters used in the gamma index calculations. 67

Table 8: r^2 values correlating pass rate with plan deviations. Pass rates were calculated using different masks to determine which points were included in the analysis. 76

Table 9: Correlation coefficients between DVH deviations and gamma pass rates calculated using a structure mask threshold with the inclusion of some points outside the structure. The falloff term represents how far outside the structure mask that points are included in the calculation 78

Table 10: Pearson r-correlation coefficients (r-values) between per-plan IMRT QA pass rates and deviations in maximum dose to the spinal cord for various gamma analysis passing criteria. 82

Table 11: Pearson r-correlation coefficients (r-values) between per-plan IMRT QA pass rates and deviations in dose to 95% of the PTV for various gamma analysis passing criteria. 83

Table 12: Measured scatter factors at 100cm SSD and 10cm depth. Field size is nominal setting on the VersaHD. Bracketed numbers show the 2*sigma uncertainty in the last digit. 94

Table 13: Measured multi-leaf collimator (MLC) transmission and dynamic leaf shifts. 97

Table 14: List of relevant DICOM Data Element tags in both hexadecimal and 8-bit formats, along with names and DICOM file types in which they are located. 118

LIST OF FIGURES

Figure 1: TCP and NTCP models showing tissue response to radiation. Also plotted is the probability of tumor control without complications. 2

Figure 2: Isodose line comparison between 3D (A) and IMRT (B) treatment techniques. IMRT isodose lines better conform to the target (red), while avoiding the normal tissue (green). 5

Figure 3: Number of PubMed articles with the term "Intensity Modulated Radiation Therapy" in the title. 6

Figure 4: Two examples of commercial MLCs. A) Varian's 120 Leaf Millennium MLC, B) Elekta's 160 leaf Agility MLC. 7

Figure 5: IMRT QA measuring devices: A) Single plane liquid filled chambers, B) Orthogonal plane diode array, C) Cylindrical diode array. 9

Figure 6: Measured dose from two differently size detectors compared with the true dose. Volume averaging increases with detector size. 12

Figure 7: IROC Houston H&N Phantom. TLD measurement devices shown in color. A) Axial, B) sagittal, C) coronal planes. 14

Figure 8: Half Beam Block (HBB) setup for steering beam centers. (A) Farmer chamber is taped on a block tray at the central axis in the GT direction, (B) the collimator is closed to the central axis to block half the field. 21

Figure 9: Correlating Half Beam Block (HBB) measurements with BB-beam center deviation results in the gun-target (GT) direction for Versa HD photon energies (6X, 10X, 15X, 6FFF, and 10FFF). The 0.0% HBB result corresponding to 0.87mm is the desired BB-beam center GT deviation. 23

Figure 10: Versa HD couch schematic showing the location of adjustment bolts A & B. The gun (G) and target (T) directions are also labeled, while the up (U) and down (D) directions are not shown. 26

Figure 11: Iterative adjustment of bending fine to achieve the ideal BB-beam center GT deviation (0.87mm). The 10X energy did not require adjustment. 28

Figure 12: Gamma Index pass rates for 111 Head and Neck IMRT QAs. Three distributions were fitted to the data (normal, truncated normal, and Weibull). Maximum Likelihood Estimators were used to obtain the optimal fitting parameters of the distributions. 34

Figure 13: Comparing the 95% confidence limits (CLs) for a normal and a truncated normal probability distribution. The normal CL is defined around the mean of the distribution. The truncated normal CL is defined by the truncation point and a lower bound. 37

Figure 14: The difference in confidence limits that were calculated using the Task Group # 119 method and the truncated normal method. The axis values are the μ and σ parameters, which describe the truncated normal distribution. 40

Figure 15: The difference in confidence limits that were calculated using the Task Group # 119 method and the Weibull method. The axis values are λ and k parameters, which describe the Weibull distribution. The shift parameter (θ) is set to zero. 41

Figure 16: 1000 SRS detector locations. Detectors are 2.3mm wide squares. Centroid spacing is 2.5mm in the center and 5.0mm in the peripheral. 45

Figure 17: 1000 SRS liquid filled ionization chamber collection efficiencies as a function of pulse dose and pulse frequencies delivered to the detector for (a) 6MV and (b) 10FFF. 53

Figure 18: Magnitude of ion recombination effects as a function of pulse frequency. All measurements are for multiples of 60Hz (100MU/min for 6X and 400MU/min for 10FFF) – they have been offset for improved visualization. The vertical axis is the percent change in ion collection efficiency for a given change in pulse dose. 54

Figure 19: Dosimetric effects of complex ion recombination corrections. (a) Measured and ion recombination corrected dose profiles along the central axis of the 1000 SRS compared to the TPS predicted dose. (b) Difference between measured and corrected profiles. The relative distance is plotted on the right vertical axis 56

Figure 20: Correlation between changes in 3D gamma analysis pass rates (ΔPR) from pulse dose corrections and (a) average MLC aperture size (AS), (b) average MU/min (RR). 3D gamma analysis was performed using a 1%/1mm criteria with a 10% dose threshold. 57

Figure 21: Schematic showing the workflow for a traditional versus structure-dependent gamma analysis 68

Figure 22: Binary structure masks used to delineate region included in the gamma calculation. (A) Overlay of the structures on a planar dose distribution, (B) PTV only structure, (C) Spine only structure, (D) traditional 10 percent mask, (E) PTV or Spine structure, (F) PTV and Spine Structure. 69

Figure 23: Effect of image dilation using the ball morphological structure element. (A) Original image, (B) dilated image, (C) dilated intensity falloff outside the original image for different ball height parameters. 70

Figure 24: Varying the gamma analysis dose and distance tolerances proportionally to the path length through planning structures. Target (PTV) in orange and spinal cord in blue. 73

Figure 25: Scaling the structure dependent passing criteria as a function of normalized structure thickness in the beams-eye-view projection of a treatment field. 74

Figure 26: Pearson r-correlation coefficients between per-plan IMRT QA Gamma Index pass rates and dose received by 95% of the PTV (PTV-D95%) and the maximum dose to the spinal cord. The distance criterion in the Gamma Index was set to 3mm, while the dose criteria and threshold criteria were varied. 75

Figure 27: Pearson r-correlation coefficients between per-plan IMRT QA Gamma Index pass rates and dose received by 95% of the PTV (PTV-D95%) and the maximum dose to the spinal cord. The threshold was set to 5%, while the dose and distance-to-agreement criteria were varied. 75

Figure 28: r^2-values comparing pass rates with plan deviations for different binary masks. (A) r^2-values with 3%/3mm, (B) r^2-values with 2%/2mm. 76

Figure 29: R^2-values for structure mask thresholds with falloff point inclusion. Dashed lines are structure masks with no falloff. Solid bars are 3cm falloff. Dotted bars are 2cm falloff. Striped bars are 1cm falloff. (a) 2%/2mm, (b) 3%/3mm. 77

Figure 30: Spine (A-C) and PTV (D-F) r^2-values for structure dependent importance weighting of each point in a 3%/3mm gamma calculation. 79

Figure 31: Spine (A-C) and PTV (D-F) r2-values for structure dependent importance weighting of each point in a 2%/2mm gamma calculation. 80

Figure 32: Per-plan IMRT QA pass rates versus deviations in maximum dose to the spinal cord for different gamma analysis passing criteria. 81

Figure 33: Per-plan IMRT QA pass rates versus deviations in maximum dose to the spinal cord for structure dependent gamma analysis passing criteria. 82

Figure 34:Per-plan IMRT QA pass rates versus deviations in the dose to 95% of the PTV for different gamma analysis passing criteria. 82

Figure 35: Per-plan IMRT QA pass rates versus deviations in the dose to 95% of the PTV for structure dependent gamma analysis passing criteria. 83

Figure 36: Comparison between per-plan Gamma Analysis pass rates for 0.5%/3mm/10% threshold and 3%/3mm/10% threshold analysis criteria. 84

Figure 37: Comparison between commissioning and calculated scatter factors at 100cm source-to-phantom distance and 10cm depth. All scatter factors were normalized to unity for a 10cm x 10cm field. 95

Figure 38: Comparison between commissioning and calculated 6FFF percent depth doses (PDDs) at 100cm source-to-phantom distance for selected field sizes. 96

Figure 39: Comparison between commissioning and calculated 6FFF diagonal profiles at 100cm source-to-phantom distance for select depths. 96

Figure 40: Difference between the measured and calculated 6FFF collimator penumbras at 100cm source-to-phantom distance, 10cm depth for a 3cm x 3cm field size. The discrepancy is smaller in the jaw direction (A) compared with the MLC direction (B). 97

Figure 41: Dose metrics for single-isocenter multi-target plans of different target sizes created with MBMS compared with Gamma Knife (GK)..... 98

Figure 42: Axial film results of the end-to-end test. (A) Isosdose overlay between Elements-predicted and film-measured dose. (B) Line profile between two targets (green line in (A)). 100

Figure 43: Plan comparisons between: (A) MBMS v1.5 and (B) MBMS v2.0. The updated algorithm removes the 12Gy dose-bridging. 101

Figure 44: Decision tree for treating cranial SRS targets with a combination of single-isocenter multi-target (SIMT), volumetric arc (VMAT), and stereotactic cones or Gamma Knife (GK) treatments. 107

Figure 45: Converting DICOM Data Element tags from hexadecimal to 8-bit. 117

Figure 46: In-room coordinate system used for structure rotations in the Matlab code. 122

Figure 47: Test fields and structures used to perform end-to-end testing on structure rotation Matlab code..... 124

CHAPTER 1 INTRODUCTION

The second leading cause of death in the United States is cancer; responsible for 591,666 or 22.53% of deaths in 2014[1]. Although the number of cancer deaths continue to increase each year, the percentage of deaths caused by cancer has fallen 12% over the past decade [2]. Data from the American Cancer Society shows that number of cancer deaths that are prevented each year has grown steadily since 1991[3]. One of the main drivers in improved cancer survival is the increase in computing power over the past decades, allowing for improved diagnosis techniques, characterization of individual cancers, and more complex treatments. As the diagnosis-treatment paradigm grows more complex, research tends to focus on subsets of the entire process.

The study of diagnosing and treating cancer begins with an examination of the human body, which exists in a homeostatic state with cells constantly dying (apoptosis, autophagy, etc.) and multiplying (mitosis). The balance of this state relies on the rate at which cell death and mitosis occur. Too much cell death and the body dies. Conversely, an uncontrolled high rate of mitosis leads to cancer. The goal of cancer therapies is then to move the body back towards a homeostatic state by killing the fast growing cancerous cells, while preserving the controlled cell growth of the normal tissue.

Amongst other cancer fighting techniques, radiation can be used to kill cancer cells. High energy radiation has the potential to ionize atoms within the body, causing fundamental damage to the cell and ultimately cell death. One issue with radiation is that it is indiscriminate towards cancerous and healthy cells. However, the cells themselves respond differently to radiation exposure. In the context of radiation therapy the groups of cells are looked at macroscopically. For cancerous cells this equates to tumor growth and for normal tissue this equates to physiological tissue or organ function. When radiation therapy is delivered the goal is to control tumor growth and limit the degradation in physiological functionality.

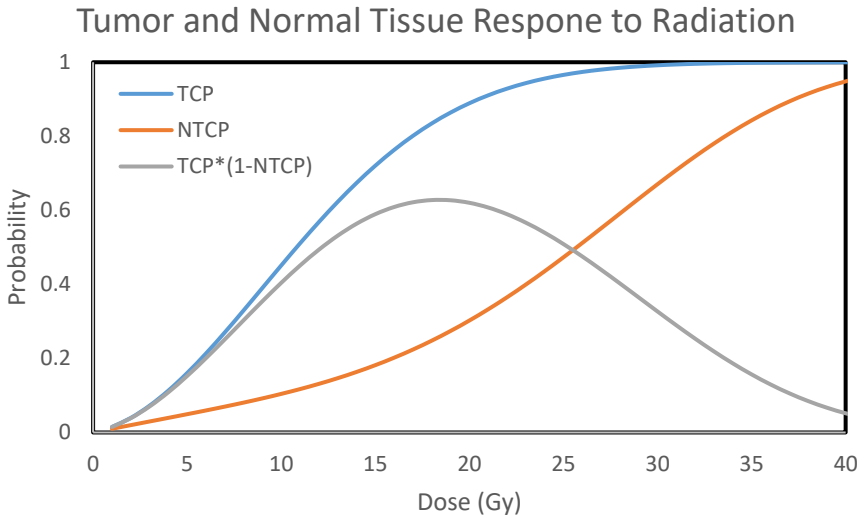

Figure 1: TCP and NTCP models showing tissue response to radiation. Also plotted is the probability of tumor control without complications.

Two terms are commonly used to describe the tumor and normal tissue response during radiation therapy:

1) tumor control probability (TCP) – "The probability that a given dose of radiation will provide tumor control or eradication considering the specific biological cells of the tumor."[4]

2) normal tissue complication probability (NTCP) – "The probability that a given dose of radiation will cause an organ or structure to experience complications considering the specific biological cells of the organ or structure."[4]

These two terms are derived from concepts regarding the number of proliferating cells surviving after irradiation, which is typically modelled with a Poisson like distribution[5]. Figure 1 shows a hypothetical example of the two probabilities plotted as a function of radiation dose. Within the two curves a region exists known as the therapeutic window, where dose is sufficient to control the tumor (high TCP), while sparing normal tissue (low NTCP). This region can best be seen by examining by plotting the probability of tumor control without complications (TCP * [1 – NTCP]).

In this simple example, the radiation therapy treatment would administer dose within this therapeutic window; the tumor would be controlled and the patient would not experience any side effects. However, the treatment becomes more complicated when patient-specific uncertainties are included within the figure. For an individual patient, the TCP and NTCP curves change from precise lines into probability distributions. Furthermore, the delivery of radiation dose itself is not exact, creating a third probably distribution. The result is that it becomes more difficult to administer dose within the therapeutic window.

Different techniques have been used to increase the chances of a successful treatment, including: widening the gap between the NTCP and TCP curves, and increasing the precision of the curves and the delivered dose. The TCP curves can be shifted to lower doses by combining radiation therapy with other forms of treatment (ex. chemotherapy, hormonotherapy, etc.). NTCP curves can be shifted to higher doses by delivery more conformal treatments, so that a given dose or radiation to the tumor delivers less dose to the surrounding tissue.

While widening the therapeutic window is an important part of radiotherapy research, this work focuses on increasing the precision of the delivered dose. As mentioned at the beginning, the diagnosis-treatment paradigm is quite complex, so it would be difficult to tackle the issue of precision from start to finish. A more attainable approach was used in this research by breaking the process into subsets and making focused improvements to increase the precision of the entire process. In the coming sections, the treatment process will be briefly outlined and broken into individual subsets for potential improvement in dose delivery precision.

There are three different types of radiation therapy:

1) Internal - temporary or permanent radioactive sources are implanted into the patient.

2) Systemic - radionuclide injections or oral administrations are given to the patient that spread throughout the entire body.
3) External - high energy beams are generated outside the body and directed toward the patient.

External beam radiation therapy is the most common treatment method. The technique involves generating radiation beams, with high enough energy to ionize atoms, and then directing them within the body. These beams can be comprised of electrons, photons, protons, neutrons, and other heaving ions. This research was focused on an advanced form of photon treatment called Intensity Modulated Radiation Therapy (IMRT).

IMRT is type of photon treatment that uses beams with spatially modulated dose distributions[6]. The technique improves upon the traditional 3-dimensional method of treating with uniform dose fields. Whereas 3D techniques create dose distributions that resemble simple geometric shapes (Figure *2*A), IMRT treatments can contain more complex distributions that conform to the cancer and better spare normal tissue (Figure *2*B). Due to the complexity of IMRT, an inverse planning method is often employed where a computer is given dosimetric objectives and an optimization algorithm is used to determine optimal beam parameters[7-9]. Conversely, 3D treatments are created using forward planning where beam parameters are set manually to achieve given dosimetric objectives[10]. IMRT was first proposed in the 1980's[11]. However, due to inverse planning's requirement for computing power, it is not surprising that the development of IMRT coincided with the technological advancement of computers in the mid 1990's[12].

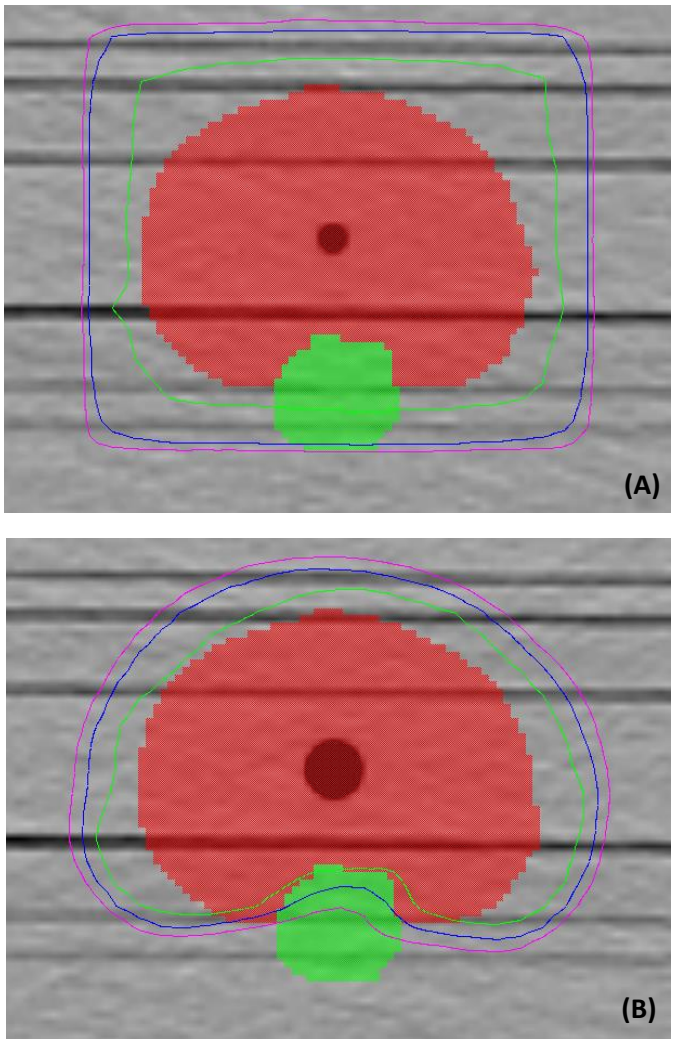

Figure 2: Isodose line comparison between 3D (A) and IMRT (B) treatment techniques. IMRT isodose lines better conform to the target (red), while avoiding the normal tissue (green).

Over the past two decades, IMRT techniques have continued to evolve. PubMed articles with the term "Intensity Modulated Radiation Therapy" in the title have been steadily increasing (Figure 3)[13]. Fueled by research, countless commercial solutions have been created providing clinical solutions for IMRT. Although the clinical solutions are diverse, the process for treating patients with IMRT is somewhat standardized.

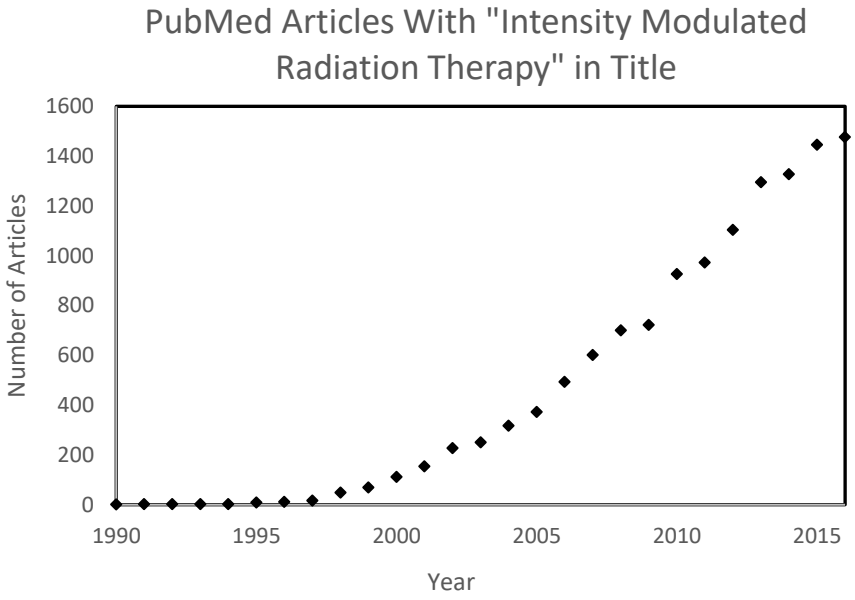

Figure 3: Number of PubMed articles with the term "Intensity Modulated Radiation Therapy" in the title.

The patient's treatment begins with a computed tomography (CT) scan to localize the tumor and normal tissue within the body. Commercial CT scanners provide multiple scanning options that typically include contrast-coincident scans for better organ delineation[14], reconstruction algorithms for artifact reduction and better image quality[15-18], 4D imaging capabilities to capture anatomy during cyclical physiological functions[19]. The end result is a CT, or series of CTs in the case of 4D imaging, which is sent to a treatment planning system (TPS) to design the therapy delivery.

Various commercial treatment planning systems are available for clinical use. Planning systems can be specific to a particular delivery system[20-22], specific to a treatment site[20, 23], or general planning solutions[24-30]. Apart from cosmetic differences, each planning system has their own solution for dose calculation and optimization. Dose calculation engines focus on speed and accuracy. Early dose engines were simple, often sacrificing accuracy for speed[31-33]. Developments in computing power and GPU-based computing[34, 35] have led to the clinical adaptation of more accurate dose engines[36, 37]. Optimization

algorithms focus on speed and flexibility to achieve acceptable solutions. A wide range of solutions exist for generating the optimization paramters[38, 39], performing the optimization[40]; evaluating and modifying the optimized solution[41]. Whatever technique is used, the TPS will generate a treatment plan that dictates how the delivery system should administer radiation to the patient.

The treatment plan generated by the TPS must conform to the physical limitations of the delivery systems. Perhaps the most important of those limitations is that of the multi-leaf collimator (MLC), which is responsible for creating the field modulation that characterizes an IMRT delivery. Various MLC designs exist, however they typically consist of independently moving collimating leaves responsible for radiation attenuation (Figure 4)[42-44]. Optimization algorithms contain checks to ensure plan deliverability, however due to complexity of the delivery system, an on-line check of the plan deliverability is often performed prior to the patient treatment.

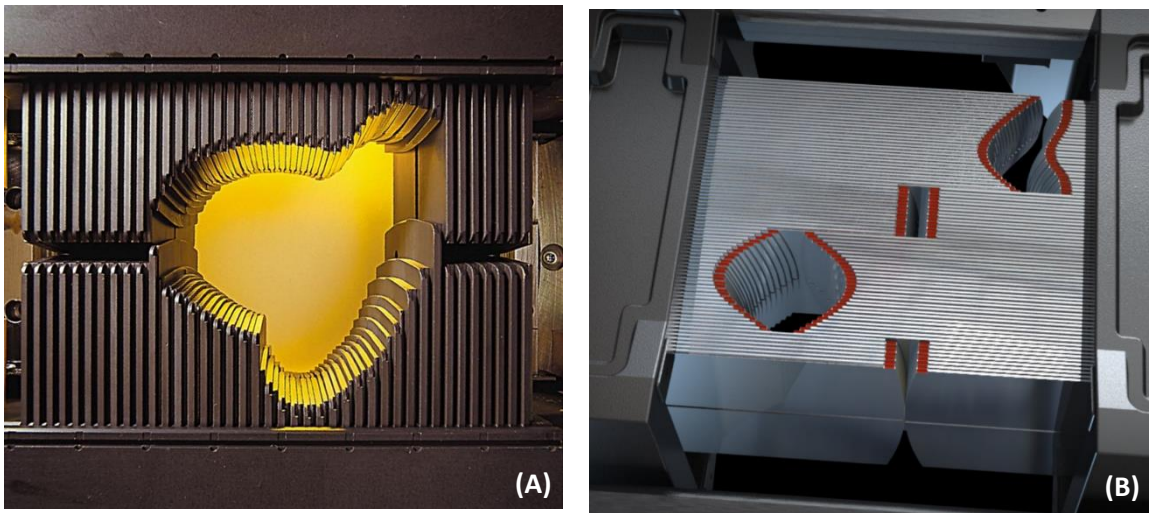

Figure 4: Two examples of commercial MLCs. A) Varian's 120 Leaf Millennium MLC, B) Elekta's 160 leaf Agility MLC.

The pre-treatment checks, colloquially referred to as IMRT QA, are typically performed by delivering the plan to devices that measure absolute and relative spatial dose distribution. The measured dose is compared to that predicted by the TPS to determine whether the treatment machine can

accurately deliver the plan generated by the TPS. The devices used to measure dose and the comparative methods are as diverse as the delivery and TPS systems themselves.

Historically, point dose measurements were performed with ion chambers[45], while spatial dose distributions were measured with radiographic film[46]. Ion chambers remain the gold standard for dose measurements, however the use of film has declined. Radiographic film requires dark rooms and chemical processors. The processing itself is sensitive to chemical composition and temperature, creating day-to-day variations in film response[47]. These shortcomings were overcome with the advent of processor-free radiochromic film[48]. Even without processing, Radiochromic film still requires the time consuming step of scanning prior to analysis.

Film is still in use today for precise stereotactic measurements as it offers the highest resolution of any dosimeter (sub-millimeter)[48], however real-time measuring devices have been widely adopted for routine IMRT QA. These devices are comprised of multi-detector arrays imbedded in water equivalent material. Geometries of the arrays, shown in Figure 5: IMRT QA measuring devices: A) Single plane liquid filled chambers, B) Orthogonal plane diode array, C) Cylindrical diode array, differ from single planes[49-53], to orthogonal planes[54], and cylindrical[55] configurations. Various detectors including open-air[50, 53] and liquid filled ion chambers[51], diodes[49, 54, 55], and EPIDs[52] have all been used. All detectors are connected to electrometers and computer software, which give direct readouts of the measurements and allow for fast comparison to the TPS.

Point dose measurements are compared to the TPS using a simple normalized difference formula. Conversely, planar dose measurements are compared to the TPS using more complex analysis techniques; the most popular of which is the Gamma Index. The Gamma Index combines dose differences with distance criteria to compare each individual detector measurement to the corresponding surrounding dose predicted by the TPS[56]. The Gamma Index itself is customizable by varying the analysis criteria[57, 58],

measurements included in the analysis[59, 60], and normalization methods[61]. In addition to the Gamma Index, other solutions have been developed that use different combinations of dose differences and distances to compare measurement planes to the TPS[62]. These analysis techniques have also been extended into three-dimension space to analyze 3D-dose reconstructions from planar measurements[63, 64]. Other pre-treatment checks analyze machine log files to check if the machine is in the correct state throughout the delivery[65]. Regardless of the pre-treatment check, if the results of the analysis meet a pre-determined threshold criteria, the treatment plan is deemed acceptable for delivery.

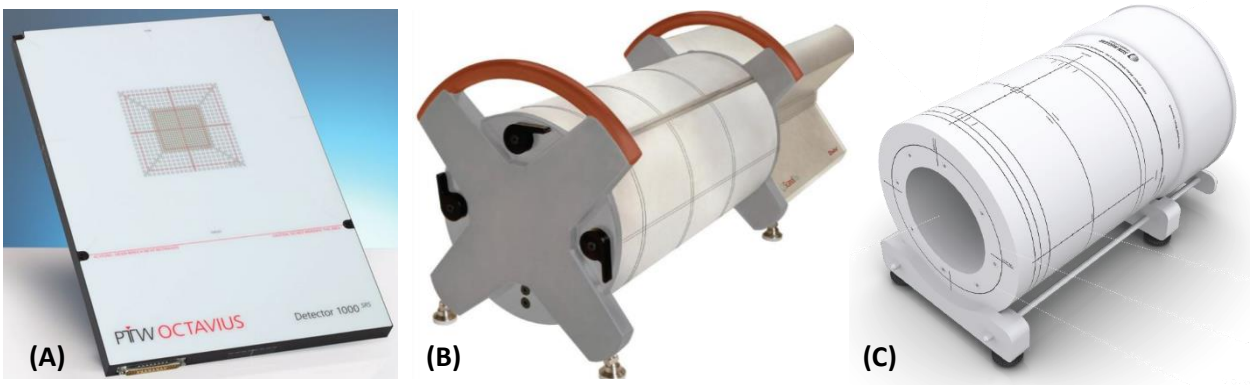

Figure 5: IMRT QA measuring devices: A) Single plane liquid filled chambers, B) Orthogonal plane diode array, C) Cylindrical diode array.

When delivering IMRT treatments to patients, the focus is on dosimetric accuracy to ensure treatment falls within the therapeutic window. Dosimetric accuracy relies on positioning the patient and the treatment volume in the same position as was planned in the TPS. The two major concerns with positioning are interfraction and intrafraction motion.

Interfraction motion can be caused by voluntary or involuntary motion. Voluntary motion occurs when a patient shifts position during treatment, usually due to discomfort. The first line of defense against voluntary motion is watching the patient outside the treatment room and halting the treatment if movement occurs. State and federal regulations mandate that the patients are monitored at all times, making this a necessity for all treatments. While gross patient movement are easily visible, small

movements are more difficult to detect. Small motion detection has been accomplished with systems that track patient anatomy[66], and internal[67] or external fiducial markers[68].

Although monitoring and detecting voluntary motion is important, prevention is usually sufficient for most treatments. To help prevent voluntary motion, immobilization devices have been designed, which place the patient in a comfortable position, while creating the most unobstructed path for the radiation to reach the target[69]. These devices are designed to be mostly radio-transparent, however beams passing through them can still be perturbed, causing dosimetric differences in the treatment[70].

A well immobilized patient will still have involuntary motion due to normal autonomic functions (breathing, heartbeat, etc.). One method to account for this motion, is to treat a larger volume, ensuring that regardless of the instantaneous phase of the autonomous motion, the tumor remains in the target area[71, 72]. The obvious issue is that this also delivers more dose to the normal tissue, reducing the therapeutic window. A less intuitive issue occurs with IMRT, due to the modulated nature of the fields and the harmonic nature of respiratory motion. Commonly referred to as the interplay effect, it occurs when the tumor moves into one area of the treatment volume, when the IMRT field is delivering the dose elsewhere within the target[73]. This effect can be mitigated by using lower dose rates and larger aperture sizes[74, 75].

The treatment volume can also be reduced by minimizing tumor motion or gating the treatment. Motion can be reduced through compression[76] and breath control, both forced[77] and voluntary[78]. Compression reduces tidal volume and the magnitude of tumor motion. Breath control has the patient pause during a specified respiratory phase (typically inspiration), which effectively eliminates respiratory-induced motion. Gating creates a window within the respiratory cycle where the beam will turn on, and can be used in parallel with breath hold or as a standalone technique[79].

While all these tools are useful for preventing intrafraction motion, the largest deviations can occur with the interfraction motion. Patient setups will naturally vary on a day-to-day basis, and can grow in magnitude from responses to treatment, such as weight loss, tissue irritation, and reduction in tumor volume. The immobilization devices that help to prevent intrafraction motion, will also provide a stable platform for reproducible interfraction setups. However, deviations are expected, therefore some form of pretreatment on-line imaging is typically performed to verify the correct patient position.

The on-line imaging systems consist of various combinations of planar radiographs, CTs[80, 81], RF trackers[82], ultrasound[83], and more recently MRIs[84]. Each system acquires information regarding the patient's position, which it compares to reference data generated from the planning CT. If a minor discrepancy is observed, the delivery systems are able to perform linear and rotation adjustments via robotic couches[85, 86] or delivery adjustments[87]. Major adjustment require manual repositioning of the patient or a re-simulation and a new plan. Once adjustments are made, and the patient is located in the correct position, the delivery is initiated and the aforementioned intrafraction positioning systems are used to monitor the patient.

From start-to-finish, an IMRT treatment involves many different sub-systems within a department. To ensure the entire system is functioning properly prior to treating the first patient, a lengthy commissioning process occurs. Multiple task group reports from the American Association of Physicists in Medicine (AAPM) have been published that outline recommended procedures for commissioning and ongoing quality assurance in a radiotherapy clinic[6, 18, 19, 88-109]. These reports address the commissioning of treatment techniques of varying complexity, starting from simple 3D treatments, to the most advanced stereotactic radio surgery (SRS) cases. A subset of these reports focus specifically on IMRT[6, 91, 96]. However, all of the reports should be considered when designing an IMRT commissioning process.

Generally, the commissioning tests that are performed specifically for IMRT implementation include: point dose measurements, planar measurements, TPS test patterns, MLC QA, end-to-end testing, and external credentialing. Although these tests are performed differently between institutions, the overall goal is to ensure accurate delivery of radiation through highly modulated and possibly moving MLC apertures.

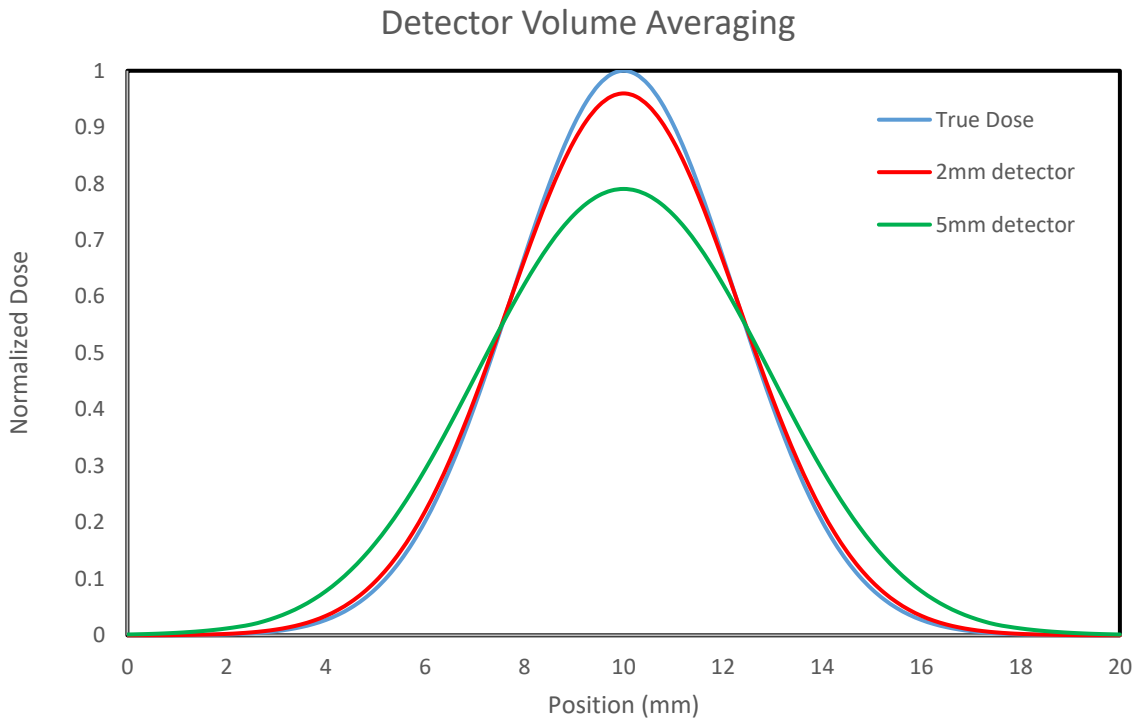

Figure 6: Measured dose from two differently size detectors compared with the true dose. Volume averaging increases with detector size.

The high degree of modulation may result in small aperture sizes, which could require specific point dose measurements for the TPS. These measurements are often more difficult than their large-field counterparts, as additional small field effects occur. The most common small field effect is volume averaging, which occurs when the detector size is on the same order of the measured dose feature[110]. As

the name suggests, the detector volume will tend to average the dose distribution causing an overall smoothing effect. An example of volume averaging is shown in Figure 6. For a field size (FWHM) of 15mm, a 2mm detector shows minor signs of volume averaging and the effect is prominently visible for a 5mm detector.

Other small field effects include: partial source shielding causing an overestimation of field size when using traditional FWHM metrics and a loss in charge particle equilibrium causing a change in detector response. All of these effects are sensitive to the detector selection and experimental setup[111]. One method that is used to account for these effects, is to perform Monte Carlo simulations to generate correction factors[112]. However, these simulations are complicated and must be done for each detector and each setup, making them unrealistic for ad hoc clinical measurements. Therefore, clinical measurements are often performed using a "daisy-chain" method, whereby different detectors are calibrated in sequentially smaller fields, and the measurements are referenced back to a precise large field dose measurement[113]. These corrections can often become more difficult for planar dose measurements when a detector under a moving MLC aperture may have a changing response.

In addition to small field planar measurements, IMRT commissioning involves a thorough analysis of dosimetric distributions surrounding the MLCs in large fields as well. The ability of the MLC leaves to move independently means often times an MLC leaf will extend into the middle of the field. As a result, the dosimetric penumbra from the leaf tip and leaf sides, as well as the transmission through the leaf, will have a greater effect on the high dose region of a field compared with a 3D treatment. Therefore, much more time is spent accurately modeling the MLC during commissioning. This typically involves measurements of more complex beam apertures which are compared to the TPS predicted dose.

Once the TPS modeling is complete, it is recommended to perform an end-to-end (E2E) test, which simulates the entire patient experience from simulation to treatment. E2E tests can either be analyzed

internally or externally. When the analysis is performed externally, an outside institution or company will send the clinic a phantom embedded with dosimeters (Figure 7) . The commissioning institution will acquire a CT of the phantom, plan an IMRT case to meet certain objectives, perform QA testing for the plan, deliver the plan to the phantom, and send the phantom and TPS dose back to the outside group. The outside group will process the phantom dosimeters and compare the measurements to the TPS dose. The qualitative results will be reported back to the institution. In some cases, they will also report a pass or fail result depending on how closely the measurements match the TPS.

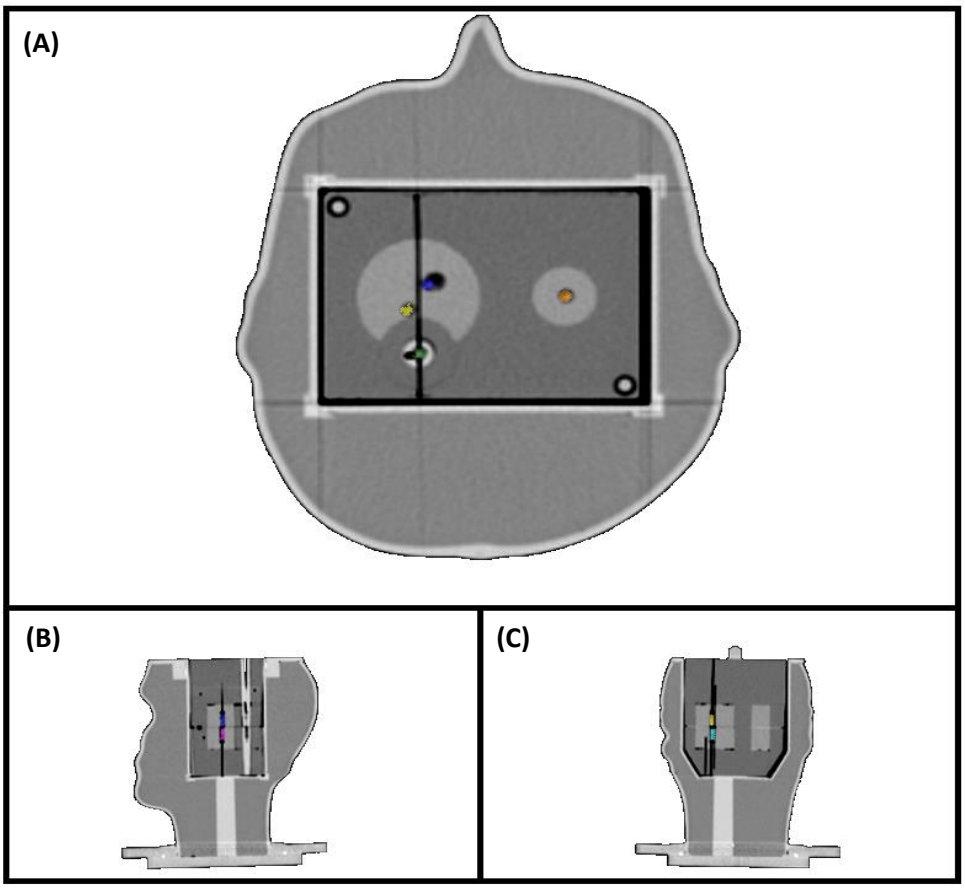

Figure 7: IROC Houston H&N Phantom. TLD measurement devices shown in color. A) Axial, B) sagittal, C) coronal planes.

This external analysis is important as it provides an independent check of an institution's processes and equipment. To ensure that institutions participating in clinical trials meet a minimum

delivery accuracy, the National Cancer Institute (NCI) requires that these tests be passed, prior to participating in radiation oncology clinical trials[114]. The Imaging and Radiation Oncology Core (IROC) in Houston, formerly known as the Radiological Physics Center, is one such group who provides these external E2E checks. A CT image of their H&N phantom is shown in Figure 7. They have published statistics of the passing rates for their tests, which show the difficulty in IMRT commissioning[115]. For example, in 2003, approximately 64% of the tests had a passing result. Fortunately, the cumulative passing rate rose steadily over the next ten years to a value of approximately 83%. The increase in pass rates was likely due to the increased familiarity with IMRT, and the availability of guidance documents. However, even with the increased pass rates, the number of institutions which still failed the test in 2013 was 11.5%, which highlights the difficulty in accurate IMRT dose delivery.

A major drawback to the external analysis is the delay in receiving results. Most institutions will also perform their own E2E tests with an internal analysis, providing immediate results, which are then used to guide commissioning. Only after rigorous internal testing is completed, the external test is performed. To provide guidance for clinical physicists performing these internal tests, AAPM TG Report No. 119 was published[96]. Distributed with the publication is a set of CTs and structure sets for a standardized solid water phantom, which is typically available in Radiation Oncology clinics. An example of these structures is shown in Figure *2*. IMRT plans are created on the CTs using planning objectives provided in TG 119. After plan generation, IMRT QA is performed using the recommended analysis and compared against other institutions results, which are published in the report. This allows a physicist to easily determine how their commissioning results compare with other institutions.

In addition to having a thorough commissioning process, routine QA of the delivery machine must be performed to ensure accurately delivery. Unlike the E2E tests which attempt to quantify the overall accuracy of the system, routine QA attempts to isolate individual components for testing. These routine QA tests are a subset of the commissioning tests, whose scope is designed to detect typical malfunctions

of the delivery system. AAPM TG Report No. 142 contains a comprehensive list of recommend tests and suggested passing tolerances[95]. The tolerances become tighter as delivery complexity increases, and increased precision is required. The overall goal is to maintain the same delivery accuracy as commissioning throughout the lifetime of the machine.

To maintain a high degree of accuracy for an IMRT delivery, uncertainties must be minimized throughout the commissioning, routine QA, simulation, planning, IMRT QA, setup, and delivery processes. The goal of this research was to look for subsets of the process for possible improvement. This work focused on research in these five areas:

1) Radiation-Imaging coincidence optimization: on-line imaging systems are calibrated to match the radiation center of the treatment machine. However, the radiation center will drift within the patient depending on the selection of machine parameters (mechanical settings and energy selection). A mismatch between the imaging and radiation centers will introduce uncertainty into the IMRT delivery. While this uncertainty cannot be completely eliminated, the imaging systems and radiation machines can be calibrated to reduce the uncertainty, thereby improving the radiation-imaging coincidence. A procedure was developed to optimize the radiation-imaging coincidence for an Elekta Versa HD (Elekta AB, Stockholm, Sweden) during commissioning. The procedural steps, along with their limitations, will be discussed.

2) End-to-end testing using AAPM Task Group No. 119 – The conclusion of this report relied on statistics calculated from the consortium data. Specifically, the data was modelled as a Gaussian distribution with an unrestricted domain. However, the data consisted of pass rates that were naturally truncated at 100%. Furthermore, the pass rates may be better modelled by a statistical distribution which is tailored to approximate failure data. Therefore, the accuracy of the statistical technique used to compare institutional results with the published consortium data was scrutinized.

3) IMRT QA Measurements – PTW's 1000 SRS device uses an array of liquid filled ionization chambers for measurements. Due to the lower ion mobility in the liquid compared with air-filled chambers, the 1000 SRS has increased ion recombination. The recombination is dependent on radiation pulse strength and duration. As the pulse characteristics change during an IMRT delivery, so too will the response of the detectors. The changing response of the detectors may lead to inaccurate measurements. The effect of changing detector response on IMRT QA measurements using the 1000 SRS was investigated.

4) IMRT QA Analysis – Typical Gamma Index calculations use a uniform set of passing criteria to analyze an entire measurement. The result is that all treatment areas and normal tissue are considered equally important during the analysis. However, clinical IMRT cases typically have one or two normal tissues with an expected dose on the edge of therapeutic window. Dosimetric accuracy is more critical for these tissues to prevent complications. The possibility of varying Gamma Index calculations across the field, specifically by using information taken from patient anatomical structures, was investigated.

5) IMRT cranial SRS commissioning: Brainlab's (Brainlab, Munich, Germany) Elements Multiple Brain Mets SRS (MBMS) is a dedicated treatment planning system for single-isocenter multi-target (SIMT) cranial stereotactic radiosurgery (SRS) treatments. Characterized by small treatment margins, hypofractionation, and large dose gradients, SRS treatments are a sub-class of IMRT deliveries that are perhaps the most sensitive to uncertainties throughout the commissioning to treatment process. The purpose of this work is to present the commissioning experience of MBMS on an Elekta Versa HD. The experience presented can be used to aid the future commissioning of Versa HDs in the Brainlab MBMS treatment planning system, to produce safe and accurate SIMT cranial SRS treatments.

CHAPTER 2 RADIATION-IMAGING COINCIDENCE OPTIMIZATION ON A VERSA HD

Introduction

The utilization rate for linac-based stereotactic body radiation therapy (SBRT) and stereotactic radiosurgery (SRS) for cancer treatment has increased throughout the 21st century.[116-119] Characterized by conformal doses and small margins, SBRT/SRS treatments are able to deliver precise doses to targets in fewer fractions compared with conventional radiotherapy options.[93] Medical physics practice guidelines address the need for heightened precision by creating tighter tolerances for machines that are being used for SRS/SBRT.[120] One such tolerance is the requirement that the on-board imaging system, used to align the patient, coincide with the radiation isocenter within 1mm. Borzov et al. have shown that the +/-1.0mm tolerance is reasonable to preserve the dosimetric delivery accuracy of SRS/SBRT[121].

Achieving coincidence of the radiation and imaging isocenter can be challenging on modern linear accelerators. This is due to the multiple photon energies available as well as the ability to use flattening filter free beams which must all coincide with a single imaging isocenter. Cross-energy calibration on Elekta's Versa HD (Elekta AB, Stockholm, Sweden) is of particular importance due to its larger gantry sag of 1.0mm compared with 0.5mm on Varian's TrueBeam (Varian Medical Systems, Pal Alto, CA). [122-125] The isocenter movement of 1.0mm on the Versa HD corresponds to a +/-0.5mm drift in radiation isocenter, which amounts to half the 1.0mm tolerance of the radiation-imaging isocenter coincidence for SRS/SBRT. Zhang et al. attempted to reduce the spread between the energies on an Elekta Versa HD using software included with the linac (Flexmap Wizard) to guide beam steering.[126] They were able to achieve radiation-imaging coincidence of less than 1.5mm for all energies, which was within their clinical tolerance.

Part of the difficulty in achieving a <1.0mm radiation-imaging isocenter coincidence across all energies is that this specification is not guaranteed by the linac manufacturers, and as such, there is no formal calibration procedure. With no direction from the vendors, it is left to physicists to develop a

procedure. In clinical practice, this calibration is best implemented with the installation engineer, prior to acceptance. However, there can often be hesitation from the installation engineer when asked to perform a calibration outside their agreed upon scope of work. Furthermore, if the physicist is unfamiliar with the procedure and its associated limitations, it may result in the physicist asking the engineer to achieve unrealistic tolerances. Therefore, in this work a formal procedure was developed to perform cross-energy isocenter calibrations during Versa HD installations. The cross-energy calibrations were performed along with couch and imaging calibrations to reduce the overall radiation-imaging isocentricity of the Versa HD and this procedure along with its limitations is discussed.

Materials and Methods

Calibration of the total radiation-imaging isocentricity of a machine is done by calibrating individual components. The following terms will be used to describe these individual components throughout this procedure:

1) Radiation beam center: center of the radiation beam that is dictated by where the electron source beam strikes the photon-generating target.
2) Collimator rotation axis: mechanical center of the collimator rotation.
3) Linac isocenter: average radiation center of a beam over all gantry and collimator rotations.
4) Couch rotation axis: mechanical center of the couch rotation.
5) Imaging isocenter: location of imaging system center or isocenter calibration and laser calibration.

In this procedure the radiation beam centers were adjusted to match the collimator rotation axis, followed by a calibration of the imaging isocenter to match the linac isocenter, and finally the couch rotation axis was adjusted to match the linac isocenter.

Prior to adjusting the radiation beam centers to match the collimator rotation axis, the linac was calibrated closely to its final geometric and beam settings during initial customer acceptance testing.

Briefly this included: adjusting percent depth doses (PDDs), profiles, collimator runout, and calibrating the MLCs and jaws to within the installation customer acceptance specifications. Importantly, the collimator mechanical isocentricity was tested and the collimating head, where the MLCs and jaws are mounted to the gantry, was adjusted to be within installation tolerances. With the linac close to clinical settings, the beam centers of each energy were steered to match the collimator rotation axis.

Steering Radiation Beam Centers to Match Collimator Rotation Axis

At this point in a traditional linac calibration, beam center steering would be performed with a half-beam block (HBB) test. The HBB setup would consist of taping a cylindrical ion chamber (e.g. Farmer-type ion chamber) in the gun-target direction to a block tray at the central axis of collimator rotation (Figure 8A) for an off-center 10x10 cm^2 field. The central axis of the farmer chamber is placed on the light-field crosshairs; small misalignments of the farmer chamber will not affect the overall result. One jaw is closed to the central axis to cover half of the field in either the gun or target direction and the opposing jaw remains open (Figure 8B). A voltage is applied to the farmer chamber, 100MU is delivered with the collimator at 0 degrees, and the resulting charge reading is recorded. The collimator is rotated 180 degrees and the measurement is repeated. If the radiation beam center was perfectly aligned with the collimator rotation axis then, these two measurements would be the same.

If the two measurements were different, an adjustment would be needed to the beam center to align it with the collimator rotation axis. This would typically be done by changing the current in the steering coils (adjusting bending fine on a Versa HD), which moves the location where the electron beam strikes the target and consequently the center of the resulting photon beam. After adjustments, the HBB test would be repeated until the two measurements agree within some threshold (<0.5% is often used). Some drawbacks to the HBB measurements are that these adjustments can be time consuming and will not give quantitative information of the distance between the beam centers and collimator axis. These

drawbacks will become exacerbated when performing the HBB test for the five photon energies on the Versa HD.

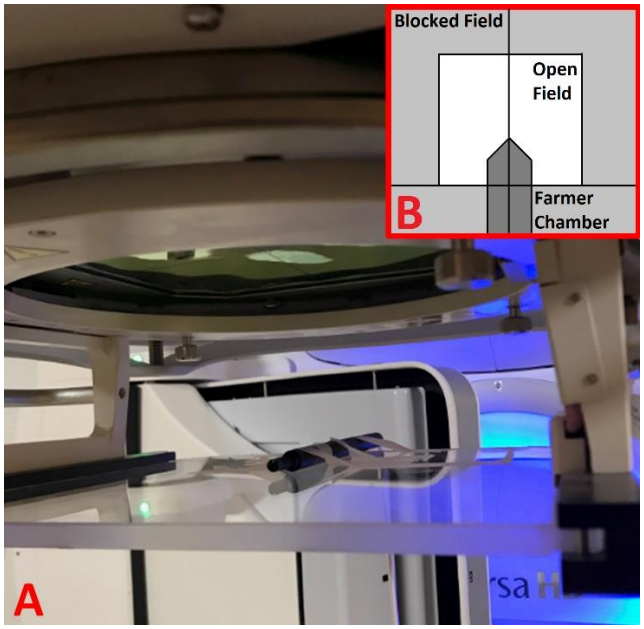

Figure 8: Half Beam Block (HBB) setup for steering beam centers. (A) Farmer chamber is taped on a block tray at the central axis in the GT direction, (B) the collimator is closed to the central axis to block half the field.

In the proposed linac calibration, to reduce the beam steering time and provide quantitative information regarding the distance from the beam centers to the collimator axis, a second test, a modified version of the Winston-Lutz test using only images at gantry, couch, and collimator angles of 0 degrees, was introduced into the calibration procedure.[127-129] By analyzing the Winston-Lutz images, the deviation between a BB, placed in the field, and the radiation beam centers could be determined (henceforth known as the BB-beam center deviation). The goal was to collect HBB measurements and BB-beam center deviations for various values of bending fine and correlate the results of the two tests to find the ideal bending fine settings needed for the BB-beam center deviation to match the HBB measurements. Adjustment could then be made to bending fine and the BB-beam center deviation could quickly be re-measured to providing quantitative information of the radiation-collimator alignment.

First, a HBB measurement was performed, using a Standard Imaging (Middleton, WI) Exradin A12 Farmer-type ion chamber, for all five photon energies at collimator angle 0 degrees without performing any beam adjustments. Next, four additional measurements were acquired for each energy with the bending fine parameter adjusted +/- 0.1 and +/- 0.2 around the starting value. To quickly change bending fine, without affecting the stored clinical beam, a 100MU beam should be started and quickly interrupted during the initial ~1 second warm-up period prior to any delivery of radiation. Then the bending fine parameter can be changed on the steering page, and the beam will be delivered with the new bending fine parameter. After delivery, the beam will revert to its original stored value for bending fine. After acquiring 5 HBB measurements at collimator 0 degrees for each photon energy, the collimator was rotated 180 degrees and the measurements were repeated. Finally, the HBB percent differences between 0 and 180 degrees was calculated for each energy and bending fine setting for a total of twenty-five results for the five photon energies.

Next, the HBB setup was completely removed, and a BB was placed close to collimator-axis using the light-field crosshairs as a guide. A square field was used to acquire portal images of the BB on the Versa HDs on-board MV imaging system (iView) at gantry and collimator angles of 0 degrees. Twenty-five portal images with the various energies and bending fine parameters to match the HBB measurements. After each portal image, the beams revert to their original stored value for bending fine as described in the previous paragraph. The portal images were exported to Sun Nuclear's SNC machine v1.3 (Sun Nuclear Corporation, Melbourne, FL) software as DICOM files, which processed the portal images to determine the BB-beam center deviation for each image.

The deviations in the gun-target direction were plotted against the results of the HBB test for the five energies and modelled with a linear regression (Figure 9). From the definition of the HBB test, if the difference between the two HBB measurements (for collimator 0 and 180 degrees) is zero percent, the beam is perfectly aligned with the collimator axis. Therefore, the linear regression can be solved to

determine the desired BB-beam center deviation needed to achieve perfect alignment between the beam centers and collimator rotation axis. It is important to note, that if the BB was perfectly placed at the collimator rotation axis, the desired BB-beam center deviation would be a distance of 0.0mm. However, since the BB was placed close to the collimator rotation axis using the light field, the desired BB-beam center deviation to achieve perfect radiation-collimator alignment will likely be non-zero. As the BB will likely not be placed perfectly at the collimator rotation axis, no adjustment should be made to the collimating jaws to match the BB position. In this instance, the average desired BB-beam center deviation over all energies, corresponding to a HBB measurement of zero percent, was 0.87mm (Figure 9).

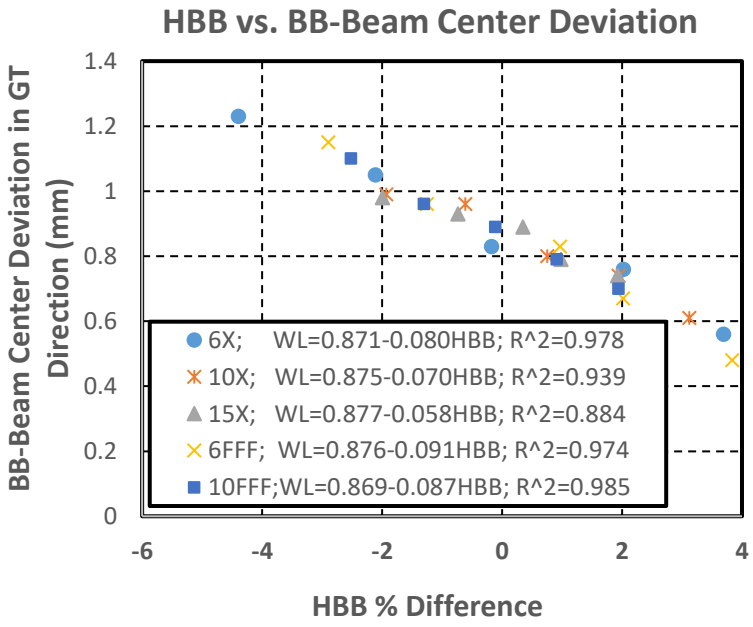

Figure 9: Correlating Half Beam Block (HBB) measurements with BB-beam center deviation results in the gun-target (GT) direction for Versa HD photon energies (6X, 10X, 15X, 6FFF, and 10FFF). The 0.0% HBB result corresponding to 0.87mm is the desired BB-beam center GT deviation.

To adjust the beam centers to match the collimator rotation axis, the bending magnets were adjusted by the service engineer using the “bending fine” setting on the linac, and another portal image was acquired and processed using SNC Machine. This procedure was repeated until the SNC Machine reported BB-beam center deviation in the gun-target (GT) direction was sufficiently close to the ideal value

determined from the linear regression (0.87mm for this calibration). After bending fine adjustments, the BB was removed, and the symmetry of the beam was checked using Sun Nuclear's IC Profiler (Sun Nuclear Corporation, Melbourne, FL). If large adjustments in bending fine are made for a given energy, a corresponding symmetry adjustment may be necessary.

Calibrating Imaging Isocenter to Match Linac Isocenter

Following the profile symmetry checks, the BB was placed back near isocenter using the light field and a 3-dimensional WL test was performed for all energies to determine their respective linac isocenters. This test utilized the Elekta provided Flexmap Wizard beam sequence, which included portal images at the four cardinal gantry angles with two collimator angles, 180 degrees apart, for a total of 8 portal images. The different gantry angles were needed to account for gantry sag, while the collimator angles were needed to nullify the effects of collimator misalignment. All portal images were acquired using iView and processed through SNC Machine, which computed the offset between the BB and linac isocenter for each energy.

With the linac isocenter position for each photon energy determined, it was decided to calibrate the lasers and kV imaging system to the average of all the energies. Some other possible options include calibrating to the average of the energies used for SRS/SBRT, or the most used energies. In this work, the average position was selected to determine the overall radiation-imaging isocentricity achievable across all energies simultaneously.

Once the selection was made, micrometers on the Elekta provided BB jig were used to move the BB to the average linac isocenter position using the shifts derived from SNC Machine. Additional 8-field WL portal images were acquired and processed through SNC Machine to ensure the BB was moved correctly relative to its original location. After verifying the BB was in the correct location, the Elekta

Flexmap Wizard was run to calibrate the imaging isocenter to the BB location, which corresponds to the average linac isocenter location for all photon energies.

After imaging calibration, the lasers were adjusted to match the external lines on the BB jig. It should be noted that the lines on the BB jig may not be perfectly aligned to the BB. When the BB jig is initially delivered to the facility, it is recommended to place small copper wires on the external lines and acquire kV images using either the kV imager on the Versa HD or topograms from a department CT. The wires and BBs will both be visible on the planar images and the wire overlap at the centroid of the BB can be evaluated.

Adjusting Couch Rotation Axis to Match Linac Isocenter

The last step in the procedure was to adjust the couch rotation axis to match the linac isocenter. The location of the current couch rotation axis relative to the radiation-gantry isocenter was determined by performing a specialized Hancock WL test that is included in SNC Machine. The Hancock WL test involved acquiring twelve WL images with a specific combination of gantry, collimator, and couch rotations (5 couch angles were used: 270, 315, 0, 45, 90 degrees). SNC Machine was used to analyze these portal images and it returned a report that states the offset between the couch rotation axis and linac isocenter. The reader is referred to the Sun Nuclear manuals for full details on how the software uses the portal images to calculate couch offset.

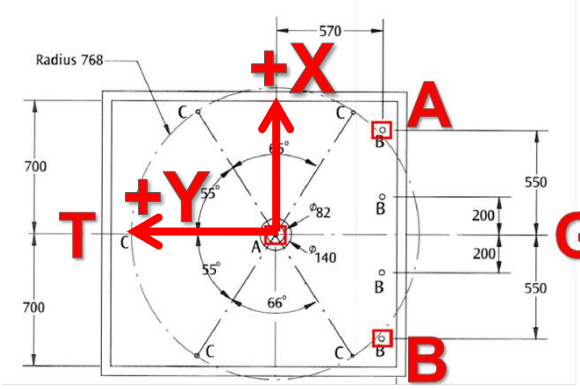

Figure 10: Versa HD couch schematic showing the location of adjustment bolts A & B. The gun (G) and target (T) directions are also labeled, while the up (U) and down (D) directions are not shown.

Alternatively, a couch runout test could have been performed by projecting the lasers (now calibrated to linac isocenter) onto a piece of paper on the couch and marking the laser position at various couch angles. If there is a deviation between the couch rotation axis and linac isocenter, the laser will trace a semicircle about the couch rotation axis.

The couch rotation axis was matched to the linac isocenter position by adjusting the couch support system. The couch sits on top of a tripod support system shown in Figure 10. The couch rotation axis was adjusted by turning the two bolts closest to the gantry according to Equations (1a) and (2b). Similar equations for other couch types can be derived through theoretical calculations or empirical testing. After the couch was adjusted, the BB was repositioned at the linac isocenter using an 8-field WL test, and the Hancock WL test was re-run until the coincidence between the couch rotation axis and linac isocenter was satisfactory.

$$\text{A Bolt turns} = (10.88\ \text{Table X} - 10.48\ \text{Table Y})\ \text{flats/cm} \tag{1a}$$

$$\text{B Bolt turns} = -(10.88\ \text{Table X} - 10.48\ \text{Table Y})\ \text{flats/cm} \tag{2b}$$

Measuring Radiation-Imaging Isocentricity

Finally, the radiation-imaging isocentricity of the system was characterized by analyzing WL portal images acquired at a subset of combinations of gantry, couch, collimator, and photon energies that were to be used for SRS/SBRT treatments with the BB located at imaging isocenter. In total, 18 combinations of gantry, collimator, and table (GCT) positions were performed: G180C270T0, G180C0T0, G180C90T0, G270C270T0, G270C0T0, G270C90T0, G0C270T0, G0C0T0, G0C45T0, G0C90T0, G0C315T0, G90C270T0, G90C0T0, G90C90T0, G0C0T45, G0C0T90C0, G0C0T315, G0C0T270. Additionally, the isocentricity was calculated for the following combinations of gantry, collimator, and table (GCT) positions: G180C0T45, G180C0T90, G180C0T315, G180C0T270. Since the number of permutations that need to be tested can become large, a smaller subset can be chosen for analysis according to clinical requirements. All WL portal images were acquired using iView and processed through SNC Machine to determine the deviation between the center of the BB and the center of the radiation field. The deviations in both directions of the image were combined to determine the Euclidian distance between the BB and the radiation field. The overall radiation-imaging isocentricity was specified as the largest Euclidian distance in any image for a given energy.

Results

The results of the bending fine adjustment along with corresponding changes to the beam center position are shown in Figure 11. The ideal location for the BB, obtained from Figure 9, was 0.87mm. All beams were calibrated within 0.10mm of the collimator rotation axis.

For future measurements, the slopes of the correlations in Figure 11 can be used to estimate the necessary change in bending fine (BF) needed to adjust the beam center for each photon energy: 6X: 0.55BF/mm, 6FFF: 0.50BF/mm, 10FFF: 0.58BF/mm, 15X: 0.75BF/mm. Bending fine adjustment was not performed for 10X during this initial testing, however it was performed at a later date and found to be

0.67BF/mm. The radiation-collimator isocentricity in the GT direction of all energies were calibrated within 0.10mm.

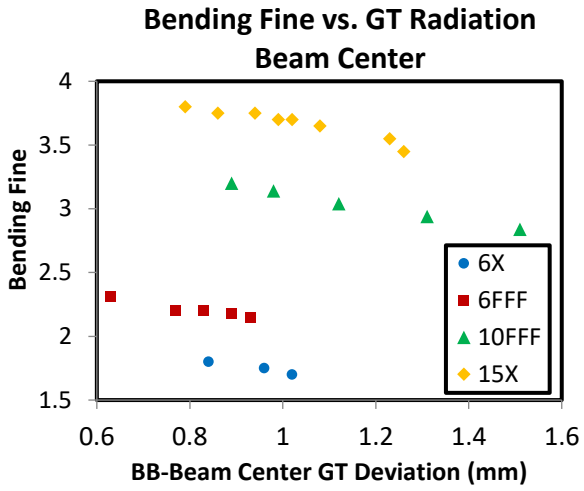

Figure 11: Iterative adjustment of bending fine to achieve the ideal BB-beam center GT deviation (0.87mm). The 10X energy did not require adjustment.

The post beam-adjustment 3-dimensional linac isocenter locations, as determined by the 8-field WL tests, are shown in Table 1. The maximum Euclidian distance between any two isocenters was 0.20mm (6FFF and 15X). The largest spread in the GT direction was 0.10mm, which matches the 0.10mm deviation that was measured during the aforementioned calibration.

Versa HD Multi-Energy Isocentricity

	Linac			Couch		
	AB (mm)	**GT (mm)**	**UD (mm)**	**Table X (mm)**	**Table Y (mm)**	**Overall Radius (mm)**
6X	0.04	0.00	0.08	0.15	-0.08	0.8
10X	0.02	-0.06	-0.01	0.1	0.12	0.88
15X	0.02	-0.01	-0.11	0.04	0.20	0.91
6FFF	-0.06	0.04	0.07	-0.15	-0.08	0.98
10FFF	-0.03	0.01	-0.01	-0.18	-0.06	0.87
Average	0.00	0.00	0.00	-0.01	0.02	0.89

Table 1: WL results showing the linac isocenter coincidence across all energies, coincidence between the couch rotation axis and linac isocenter, and overall radiation-imaging coincidence for all gantry, collimator, and couch angles.

The post table-adjustment coincidence between the couch rotation axis and the linac isocenter position for each photon energy is shown in Table 1. The overall radiation-imaging isocentricity for all gantry, collimator, and couch angles of all energies was less than 1.0mm.

Discussion

Following this procedure, the beam centers were matched to within 0.10mm in the GT direction. A similar procedure can be repeated to match the energy isocenters in the AB (left-right) direction. However, there is no easily adjustable parameter, like bending magnet current, which can steer the beam in the AB direction. Rather, if a discrepancy is found, the symmetry should be checked, followed by an examination of the beam startup.

Many of these measurements can be performed using the stored beam option in the Versa HD service mode. However, caution should be used when switching between energies in stored beams as there can be a hysteresis effect where the previously selected energy effects the current measurement. In the context of this procedure, this is particularly problematic when switching from a higher energy to a lower energy. Instead of starting from a low bending magnet current (bending magnet coarse parameter in service mode) and increasing the current to the appropriate value for the beam energy, as is done in clinical mode, the linac will drop the bending magnet current when switching from a higher energy to a lower energy in stored beams. Approaching the desired bending magnet current from a different direction can cause the beam center to shift. To prevent this issue, it is recommended to first load a field of the desired energy using the quick beam service page, prior to switching energies in the stored beams service page, particularly when switching from high to low energies. Loading a field of the desired energy in the quick beams service page, will mimic the bending magnet behavior of clinical mode and prevent the hysteresis behavior when switching back to stored beams.

The ideal location for the cross-energy isocenter calibrations was determined by correlating the results of the HBB test with the BB-beam center deviations for all energies. However, the main reason for performing the HBB measurements is to correlate the results with the BB-beam center deviations to find the GT deviation in the images that corresponds to the collimator rotation axis. The collimator rotation axis is a mechanical property of the machine that should not change between energies. From Figure 9, the maximum difference in ideal BB deviation, corresponding to the collimator rotation axis, between energies was 0.008mm. Therefore, to reduce calibration time, the HBB and BB-beam center deviation measurements can be performed for a subset of energies.

Various vendors manufacture BB jigs that attach to the couch and allow micrometer adjustments of the BB position in a specified direction. In practice, shifting the BB along one direction often leads to unwanted small changes in orthogonal directions. For example, moving the BB in the GT direction may inadvertently cause a shift in the AB direction. Alternatively, the 6 degree of freedom Hexapod couch can be used to move the BB. It was found that the Hexapod couch can reproducibly move a BB within 0.10mm of isocenter in all directions. Regardless of the movement method, care should be taken to level the couch and align it as close to angle 0 degrees as possible to ensure translational couch movements correlate with the gantry coordinate system.

For the Versa HD tested in this study, it was possible to achieve <1mm radiation-imaging coincidence for all energies. In practice, SRS/SBRT tolerances may only be maintained for selected energies on the treatment machine. Table 2 shows two tolerance levels for the individual steps of the described procedure. It is recommended that Tolerance A values be met for all energies that will be used for SRS/SBRT. Tolerance B values, which were achieved during commissioning, are the limits at which it is expected that any additional work may result in diminishing returns.

Versa HD Isocentricity Tolerances

	Tolerance A	Tolerance B
Beam center vs. collimator rotation axis coincidence	0.20mm	0.10mm
Cross-energy linac isocenter coincidence	0.50mm	0.20mm
Linac isocenter vs. couch rotation axis coincidence	0.50mm	0.25mm

Table 2: Tolerance A: Easily achievable on all Versa HDs. Tolerance B: lower expected limit of what is achievable.

Furthermore, the shape and magnitude of inherent couch-wobble will vary between Hexapod couches. This may affect the achievable imaging-couch isocenter coincidence for a given linac. If an inherent couch wobble is large enough to prevent the calibration of all energies within the 1.0mm SBRT/SRS tolerances, it is recommended that a subset of the energies be calibrated for SRS/SBRT or the couch be replaced.

Conclusion

A procedure was developed to calibrate the cross-energy radiation isocenter locations for all photon energies on multi-energy linac. It was implemented during commissioning of a Versa HD, where it was able to achieve the radiation-imaging coincidence tolerance of <1.0mm for all energies. This work provides a framework to help physicists achieve SRS/SBRT tolerances in a simple and precise manner, eliminating much of the tediousness usually encountered when optimizing machine isocentricity.

CHAPTER 3 AN ANALYSIS OF CONFIDENCE LIMITS USED IN AAPM TASK GROUP NO. 119

Using a set of standardized phantoms and measurement protocols, AAPM Task Group #119 established quantitative confidence limits as baseline values for the purpose of evaluating IMRT commissioning[96]. For all criteria presented in the report, confidence limits (CL) are determined under the assumption of a random distribution of measured values, thereby establishing these limits as a function of the standard deviation of a normal distribution. As noted in the report, assuming the measured data to fall along a normal distribution may not be valid for IMRT gamma index pass rate data.

During IMRT quality assurance, planar dose distributions are measured using detector arrays, film or electronic portal imaging devices (EPIDs) [130-132]. The measurements are compared to planar dose distributions using a gamma evaluation introduced by Low *et al.*[133]. The goal of the evaluation is to determine if the treatment machine can accurately deliver the calculated dose from the planning software. The gamma index analysis is performed for multiple points in the plane and the percentage of points which pass the analysis are reported as the gamma index pass rate. The gamma index pass rate has lower and upper bounds of 0% and 100% respectively. These bounds — the 100% upper bound in particular — prevent the measured data from following a true normal distribution. Quantitative CLs established in the report for gamma pass rate based on unbounded normally distributed data are, therefore, approximations of the CLs defined on the true bounded distribution of the data, and may not accurately reflect the statistical confidence sought through their use.

In order to evaluate CLs more representative of the TG #119 gamma pass rate data, an accurate fit of the data must first be found. Since the gamma pass rate data is bounded at 100%, an asymmetric distribution should be employed. In this study we chose two asymmetric distributions to attempt to better represent the data: a *truncated* normal distribution and a Weibull distribution. Using these distributions we can fit the data by employing Maximum Likelihood Estimators (MLE), and from there

determine confidence intervals on IMRT data sets. In addition to comparing the CLs of different distributed fits on IMRT data, we also attempt to make more general statements about the differences between the CLs established in this situation by a standard normal distribution and the asymmetric distributions described above.

If the CLs determined by fitting the measured data to more accurate distributions significantly differ from those in determined in TG #119, then, at the very least, the interpretation of the approximated CLs needs to be amended. Furthermore, if the difference between the TG #119 CLs and those calculated using stricter fits of the data changes significantly as the measured data changes, not only must the TG #119 CLs be interpreted differently, but the utility of the approximation presented in the TG report could be compromised.

In this work we investigate methods for calculating CLs with truncated normal and Weibull distributions, and compare those limits with CLs calculated using the TG #119 formalism. We then discuss the potential impact of this truncated modeling on the IMRT commissioning criteria presented in TG #119.

Material and Methods

In order to test the differences between CLs determined in the method of TG #119 and those determined by tighter fits of the data, we analyzed clinical gamma pass rate data using TG #119's normal distribution and two truncated asymmetric distributions: truncated normal and Weibull. Our data consisted of gamma pass rate values for 111 Head and Neck patients from the Karmanos Cancer Center (Detroit, MI). The data was collected using Mapcheck (Sun Nuclear Corporation) and analyzed with a 3%/3mm gamma index using a cutoff criteria of 10% of the maximum dose.

In Figure *12*, we present a frequency plot of the 111 gamma index pass rates using a bin size of 0.5%. The figure also displays fits to this data using the TG #119 method (normal distribution), a truncated normal distribution, and a Weibull distribution. To determine how well the fits describe the data, we used

the Kolmogorov-Smirnov (K-S) goodness-of-fit test. CLs were determined for each of these cases as described below.

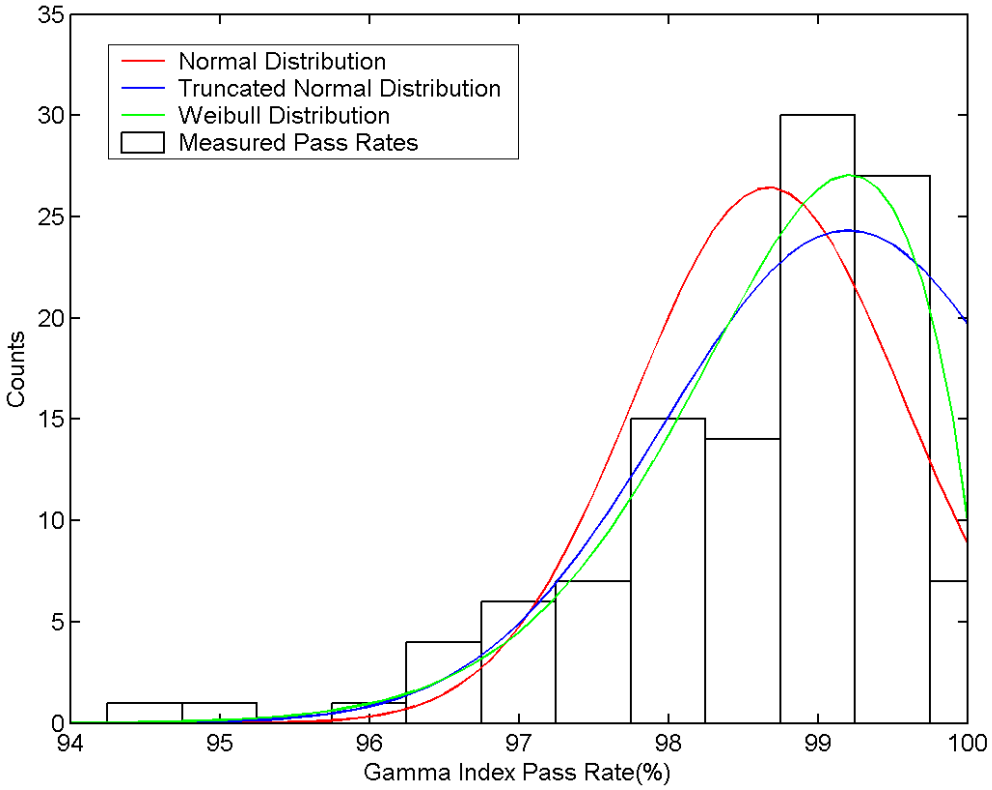

Figure 12: Gamma Index pass rates for 111 Head and Neck IMRT QAs. Three distributions were fitted to the data (normal, truncated normal, and Weibull). Maximum Likelihood Estimators were used to obtain the optimal fitting parameters of the distributions.

Truncated Asymmetric Distributions

To describe the first asymmetric distribution we choose to employ, it is helpful to begin with a description of the standard normal distribution used in TG #119 to approximate gamma index pass rate data. The normal distribution is characterized by two constants, the mean, μ, and standard deviation, σ, where μ represents the most probable outcome and σ is a measure of the spread of the measurements from the mean (Equation 3).

$$P_{Norm}(x) = \frac{1}{\sqrt{2\pi\sigma^2}} e^{\frac{-(x-\mu)^2}{2\sigma^2}}, \quad -\infty < x < \infty \qquad (3)$$

For a *truncated* normal distribution, only the range within which the distribution is defined as non-zero changes. As opposed to the standard normal distribution defined over all space, the truncated normal distribution is defined only within a specified range, which, for our purposes, is 0 <x<100. The parameters μ and σ no longer represent the mean and the standard deviation of the distribution, but instead are simply parameters describing the distributions' shape[134]. The actual mean and standard deviation of the distribution must be calculated on the non-zero interval defined above. The parameters μ and σ can still be thought of as the mean and standard deviation of the *un-truncated* normal distribution from which the truncated distribution was established. This remains helpful for visualization, as the parameter μ represents the peak of the distribution when it falls within the non-zero range.

The other distribution fitted to the TG #119 data is the Weibull distribution given by:

$$P_{Weibull}(x) = \frac{k}{\lambda}\left(\frac{x-\theta}{\lambda}\right)^{k-1} e^{-\left(\frac{x-\theta}{\lambda}\right)^k}, \quad x \geq 0 \quad (4)$$

where k, λ and ϑ are the shape, scale and shift parameters respectively[135]. Depending on the parameters, the Weibull distribution can resemble a normal, Poisson or exponential distribution. The shape parameter, $k > 0$, is the primary variable which affects the distribution that the Weibull will most closely resemble, while the scale parameter, $\lambda > 0$, primarily controls the structure of the chosen distribution. The final parameter ϑ, allows the distribution to shift along the x-axis much like the normal distribution parameter μ shifts the mean of the normal distribution. The Weibull distribution is defined only for $x \geq 0$, and thus is naturally truncated. To employ this natural truncation of the Weibull, we reflect our data and reinterpret it as a set of gamma index failure rates. The resulting failure rate data is truncated at zero and has a mean very near the truncation point — an ideal data-set to model with a Weibull distribution.

Maximum Likelihood Estimators

Modeling gamma index pass rate data using the asymmetric distributions described above involves fitting the data using an MLE method. The MLE method involves calculating a maximum likelihood function, *H*, with a wide range of model parameters. The optimal model parameters, and therefore the optimal distribution fit, are then chosen as those that maximize *H*. For the example of a truncated normal distribution, the maximum likelihood function derived by Cohen[134, 136] is:

$$H(x_0, x_1, \cdots x_n; \mu, \sigma) = [1 - F(\xi)]^{-n} (\sigma\sqrt{2\pi})^{-n} \exp\left[-\sum_{1}^{n} (x_i - \mu)^2 / 2\sigma^2 \right] \quad (5)$$

where x_n is the measured data, σ affects the shape of the distribution and μ still represents the most probable measurement of the distribution.

For a sample that is truncated on the right, such as the gamma index, $F(\xi)$ is the probability that a measured value will be truncated by the upper limit (L).

$$F(\xi) = \frac{1}{\sqrt{2\pi\sigma^2}} \int_{L}^{\infty} \exp(-(\xi - \mu)^2 / 2\sigma^2) d\xi \quad (6)$$

The computer MLE calculation is performed by varying μ and σ to find the values which maximize $H(x;\mu,\sigma)$. Example MLE calculations that are written in Matlab and Mathematica have been described by Myung[137] and Currie[138] respectively.

For distributions other than a truncated normal distribution, such as the Weibull distribution, the same type of analysis is possible[139]. The functions *H* and *F* are defined for the given distribution, and *H* is maximized to determine the set of parameters that give the best fit to the measured data.

Confidence Limit Calculations

TG #119 approximated their gamma index pass rate data with the normal probability distribution (Eq. 3). The CL of the normal distribution is traditionally described as a range around the mean of the data(±*w*) and determines the probability that a single measurement will fall within that range. It is usually calculated such that 95% of the measured points are expected to fall within that range (Figure *13*). Integrating the normal distribution gives this confidence interval to be CL = mean ± 1.96σ (Eq. 7).

$$0.95 \leq \int_{\mu-w}^{\mu+w} P(x)dx \text{ , where CL} \in (\mu\text{-w},\mu\text{+w}) \qquad (7)$$

Following the methods of Venselaar[140] and Palta[141], TG 119 used this equation to calculate the CL.

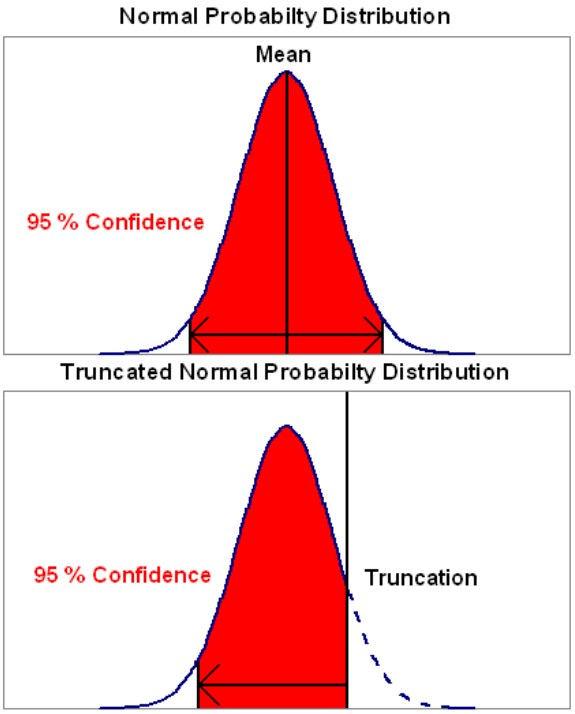

Figure 13: Comparing the 95% confidence limits (CLs) for a normal and a truncated normal probability distribution. The normal CL is defined around the mean of the distribution. The truncated normal CL is defined by the truncation point and a lower bound.

When using a truncated asymmetric probability distribution (*T(x)*), a portion of the domain on which the original, un-truncated probability function is defined is not included. Therefore, the probability function is re-normalize to exclude these values. This re-normalization is shown in Equation 8 for the gamma index pass rate, with limits of 0 and 100%.

$$T_{normalized}(x) = \frac{T(x)}{\int_0^{100} T(x)dx} \qquad (8)$$

When analyzing IMRT gamma index pass rates, we want to determine the CL such that 95% of our measurements are *larger* than a specified gamma index (L_o), as opposed to a range around a mean value. The two different CLs are shown in Figure *13*. Equation 9 was used to calculate the CLs for the gamma index pass rates.

$$0.95 \leq \int_{L_o}^{100} T_{normalized}(x)dx \text{ , where CL} \in (L_o, 100) \qquad (9)$$

As a general method to establish confidence limits in a truncated dataset such as IMRT gamma pass-rate data, we employ a three-step process: we first model the data with a truncated asymmetric distribution using the MLE method (Equation 5), we then renormalize the data on the truncated interval (Equation 8), and finally, we calculate a CL by integrating the renormalized probability distribution (Equation 9).

Modeling Expected Differences in CL

To provide a more generalized understanding of possible differences in CLs calculated using the different methods, we tested the accuracy of the TG #119 CL calculations in a multitude of idealized situations. For a range of parameters (e.g., μ and σ for a truncated normal distribution) an asymmetric, truncated probability distribution was calculated, and the resulting distribution was assumed to represent

an *ideal* set of IMRT gamma index pass rate data. CLs for the simulated gamma pass-rate data were then found using both the truncated CL definition (Equation 9) and the TG #119 definition (CL = mean ± 1.96σ). We then calculated the difference between the TG #119 and truncated CLs. The analysis was performed for both the truncated normal distribution, and the Weibull distribution. Due to the fact that the Weibull distribution has three parameters to vary (λ, k, ϑ), we performed the above analysis for only a few values of the shift parameter, ϑ.

Results

The results of the analysis of our H&N pass rates are presented in Table 3 and Figure 14 and Figure 15. The differences between the CLs calculated with TG #119 and our asymmetric distributions were 0.09% and -0.03% for truncated normal and Weibull distributions respectively. The K-S statistics were calculated using the K-S test and the P-values were estimated from published tables[142, 143].

	Untruncated Normal		Truncated Normal		Weibull	
MLE Fitted Parameters	**μ**	98.67	**μ**	99.2	**k**	1.63
	σ	0.90	**σ**	1.23	**λ**	1.59
					θ	-0.10
95% Confidence Limits		96.91%		97.00%		96.99%
K-S Statistic		0.1417		0.1065		0.0856
K-S P-value		<0.01		~0.01		~0.05

Table 3: Three distributions were fitted to gamma index pass rate data for 111 Head and Neck IMRT QAs. Confidence limits were calculated for each distribution and Kolmogorov-Smirnov goodness-of-fit tests were performed.

Figure 14 and Figure 15 are the expected differences for the CLs that were calculated using the procedure described previously where a series of ideal pass-rate data was simulated with both truncated distribution types. Figure *14* shows the differences in CLs when the data was simulated with a truncated normal. In Figure 14 the largest differences between the calculated CLs is approximately 1.2%. As the mean of the distribution gets further away from the upper bound (100%), the difference in the CLs will

continue to slightly increase. However, Palta *et al.*[141] and TG #119 suggest a clinical action level of 90%, therefore lower mean pass rates have been omitted from the analysis.

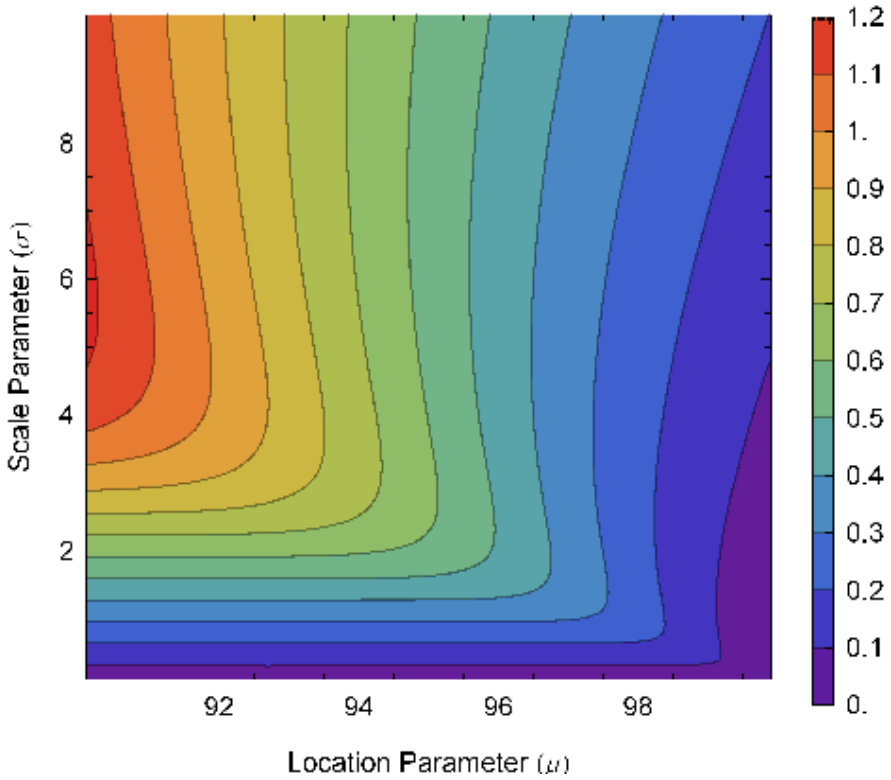

Figure 14: The difference in confidence limits that were calculated using the Task Group # 119 method and the truncated normal method. The axis values are the μ and σ parameters, which describe the truncated normal distribution.

Figure 15 shows the differences in CLs when the data was simulated with a Weibull distribution. The largest difference between the calculated CLs was approximately 1.0%. The data in Figure 15 was calculated with a constant shift parameter equal to zero. Changing the shift parameter of the Weibull distribution does affect the calculated difference for each (λ,k) pair, however the maximum difference, as shown in Figure 15, was independent of the value of the shift parameter.

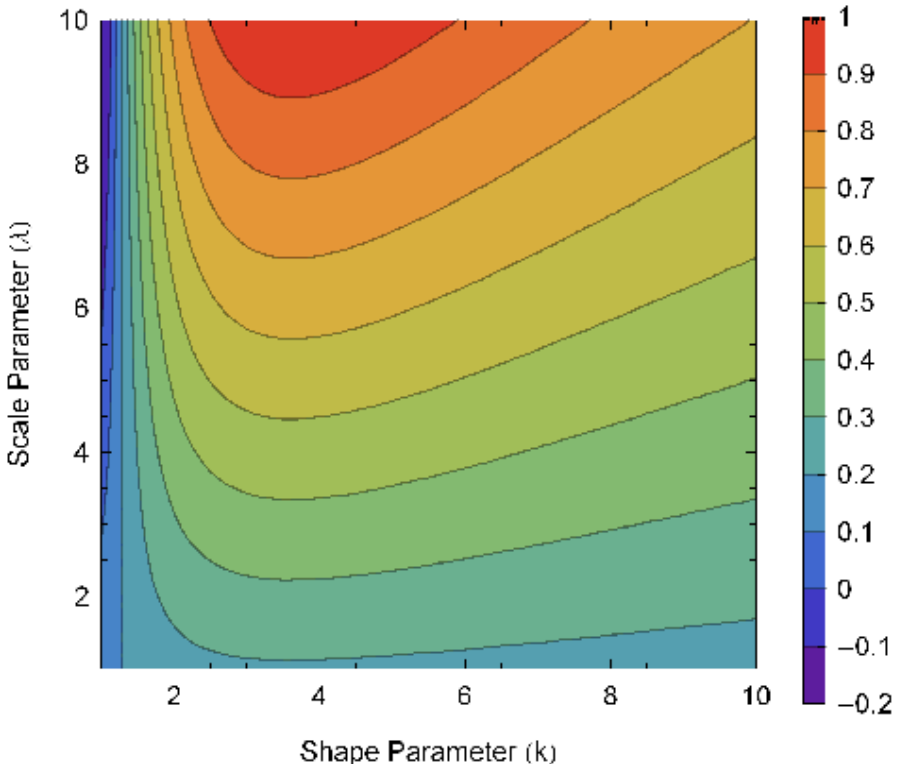

Figure 15: The difference in confidence limits that were calculated using the Task Group # 119 method and the Weibull method. The axis values are λ and k parameters, which describe the Weibull distribution. The shift parameter (θ) is set to zero.

Discussion

Somewhat surprisingly, the CLs determined for each distribution type on both measured data, and on simulated idealized data differ very little. Despite the poor fit that a normal distribution gives to a truncated data-set, *specifically designed* to not be normally distributed, the resulting CL found using the TG #119 definition differs at most by approximately 1.2%. Moreover, the maximum CL differences are found only at parameter values where the idealized data are near the clinically acceptable limits[96, 141]. The apparent unimportance of accurate distribution fit likely arises from two competing factors: the differing definitions of CL between the fitting methods, and the better fit to the data itself. The way in which CLs are calculated here for the asymmetric distributions immediately shifts the CL closer to 100%, as we have taken the definition to be representative of the point *above* which 95% of the data most probably lies, as

opposed to TG #119 which takes the definition of CL to be lower point defining the range *inside of* which 95% most probably lies. In competition to that shift, however, is a shift away from 100% due to the overall ability of the distribution to more accurately fit the data, which tends to flatten out the asymmetric distribution in comparison to a standard normal fit.

The K-S goodness-of-fit test showed a higher probability that our limited data set originated from Weibull distributed data than for either the normal distribution or the truncated normal. Despite the better fit of the Weibull relative to the other distributions, the low p-value of the MLE determined Weibull shows that it is far from a certainty that the distribution of IMRT gamma index pass rates can always be described in this way. Nevertheless, the 5% probability associated with the Weibull fit significantly improves upon the very low probability for a normally distributed data set, and in fact, as data were added to the statistics during the completion of this study, the trend of the data set was consistently towards a higher probability of Weibull fit.

The better fits shown in Figure *12* may advocate the use of the MLE method in all fitting scenarios, but there are drawbacks to the MLEs. The MLE method is a cumbersome process that involves writing programming code to determine the optimal solution. A possible solution, if indeed even necessary, would be to create a distributable MLE program that could accompany TG #119. Even with a compact MLE program, there is a biasing effect when using MLEs to fit small data sets to Weibull distributions[144, 145]. The biasing effect can lead to differences in the calculated CLs. The effect can be calculated, however this would further increase the complexity of the MLE method.

The confidence limit calculations used to generate Figure *14* and Figure *15* were performed with an ideal data set. This was done as a theoretical example to show the differences in CL calculations that we would expect when using the two different methods. In real IMRT measurements, the fitted distribution will not perfectly describe the data. Rather, the fitted distribution is a best guess of the true

probability distribution, based off of a limited data set. Therefore the difference in the CL calculations may be different from our simulated situation. Furthermore, the simulation was performed by assuming that gamma index pass rate data follows either a truncated Gaussian or a Weibull distribution. In reality, the statistical distribution of the pass rate data is probably more complex. However, as the goodness-of-fit tests show, the three-parameter Weibull distribution has the ability to approximate clinical gamma index pass rate data.

Conclusion

A straight normal fit to measured gamma pass rate data is almost always going to be a very poor approximation of the distribution due to the upper bound of 100% on the gamma pass rates. However, due to the small range of distributed data points, a confidence limit determined by assuming a straight Gaussian fit will likely be within 1.2% of those determined by other, more accurate fits of the data. Given the scarcity of data points in the IMRT commissioning process, the approximation introduced in TG #119 allows for a significant simplification of data analysis while being accurate to within the limitations of the data set itself.

CHAPTER 4 IMRT QA MEASUREMENTS – PTW's 1000 SRS

Introduction

IMRT quality assurance (QA) consists of delivering patient plans to dosimetric measuring devices and comparing the dose to that predicted by the treatment planning system (TPS). The devices must accurately measure dose with high enough resolution to sufficiently characterize the field. When small field sizes are used this requires the close placement of small detectors[146, 147]. This can cause issues when using air filled ionization chambers, typically used in non-IMRT radiation dose measurements[110, 148]. The low-density air results in less scatter and a low signal to noise ratio, which limits the proximity and size of the detectors.

One potential solution is to use liquid-filled ionization chambers (LICs), which use higher-density liquid to increase response and scatter[149, 150]. However, there is a tradeoff – the liquid reduces ion mobility, leading to ion collection times that are approximately 100 times larger than air-filled chambers, which increases ion recombination effects[151-157]. Ion recombination effects have been studied in LICs and found to be proportional to the frequency and dose of the pulses delivered to the detector, among other things. The dose and frequency of the pulses at each detector will vary during an IMRT delivery due to the changing MLC aperture and changing machine MU/min, respectively. This could potentially introduce ion recombination effects into QA measurements, resulting in a distortion of the dose map and overall IMRT QA results.

The PTW 1000 SRS array (PTW, Freiburg, Germany) implements the above described LICs, for small field IMRT measurements[158]. The goal of this research is to determine the effect of ion recombination on clinical 1000 SRS IMRT QA measurements and investigate two potential ion recombination correction methods.

Materials and Methods

The device used in this study is the 1000 SRS detector. The 1000 SRS detector consists of 977 isooctane-filled liquid ionization chambers (LICs). The chambers have dimensions 2.3mm x 2.3mm x 0.5mm (depth). The chambers are arranged in a planar array with a spacing of 2.5mm in the center of the array and 5.0mm at the periphery (Figure 16). During measurements the array was placed in a rotating Octavius 4D phantom, which uses an inclinometer to keep the array aligned perpendicular to the axis of the beam[159]. All measurements were performed on a TrueBeam linear accelerator (Varian Medical Systems, Pal Alto, CA) equipped with a high definition multi-leaf collimator (HD-MLC).

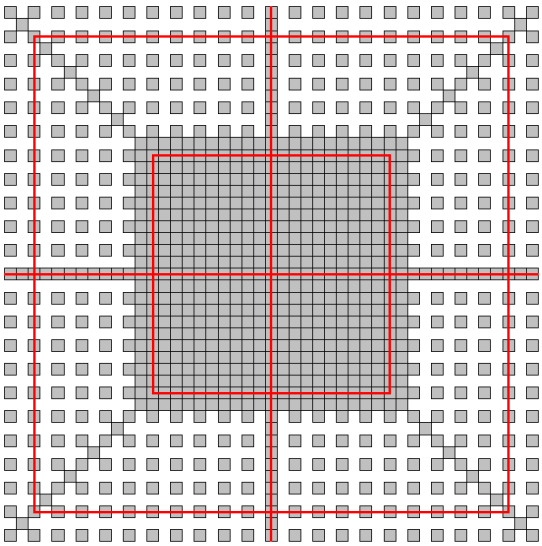

Figure 16: 1000 SRS detector locations. Detectors are 2.3mm wide squares. Centroid spacing is 2.5mm in the center and 5.0mm in the peripheral.

<u>LIC ion recombination</u>

The evaluation of the 1000 SRS detector began by determining the correlation between collection efficiency and pulse dose for the 1000 SRS LICs in 6MV and 10FFF beams. This investigation consisted of exposing the 1000 SRS detector to different pulse dose rates, measuring the dose, and comparing the

results to true dose measured with a 0.125cm^2 model 31010 air-filled ionization chamber (PTW, Freiburg, Germany) to determine the LIC collection efficiencies.

To create a consistent setup where the 1000 SRS detector measured the same pulse dose as the ion chamber, the detectors were alternately placed at the same location in a virtual water stack. Prior to measurements, both devices were by pre-irradiated, per manufacturer recommendations. After pre-irradiation, 9.1cm of solid water was placed on top of the 1000 SRS – combined with the 0.9cm buildup in the device this resulted in an equivalent depth of 10cm. The distance to the surface of the solid water, or source-to-phantom distance (SPD), was set to 100cm. 100Mus were delivered to the 1000 SRS using a 10cm x 10cm field with the maximum dose rate of 600MU/min and 2400MU/min for 6MV and 10FFF, respectively. For subsequent measurements, the SPD and buildup on top of the 1000 SRS was varied to produce different pulse doses at the detectors. For each SPD and depth combination, the 1000 SRS measurements were divided by the ion chamber reading, which was corrected for P_{tp}, P_{pol}, and P_{ion} using TG51 formalisms[108]. These ratios were subsequently normalized to the dose/charge ratio at 100cm SPD and 10cm depth. The change in the dose/charge ratio at each SPD/depth combination was attributed to the different collection efficiencies of the LICs caused by the different pulse doses.

To correlate the LIC collection efficiencies with pulse dose, the pulse dose at the 1000 SRS central chamber was calculated for each SPD. The dose and number of pulses were determined separately and then used to calculated pulse dose. First, dose was obtained for 100cm SPD by simulating the delivery in the Eclipse TPS (Varian Medical Systems, Pal Alto, CA), and calculating dose to the center detector. To eliminate any potential dosimetric effects caused by calculating dose in the treatment planning system at different SPDs, the ratio of the corrected ionization chamber readings were used to convert dose at 100cm to dose at other SPDs.

The number of pulses was determined from the pulse repetition frequency of the linac and the delivery time. The deliveries were performed at the maximum MU/min (600MU/min and 2400MU/min for 6X and 10FFF, respectively), which corresponds to a linac pulse frequency of 360Hz. Pulse frequency and calculated dose to the 1000 SRS detector were used to calculate pulse dose at each SPD.

The collection efficiencies were plotted against the pulse dose for different SPDs to obtain the pulse dose dependency of the 1000 SRS detector central chamber. The plotted data was modeled using a linear least-square fitting method. Based on the fitting results, a constant was subtracted from all of the collection efficiency data so that the modelled collection efficiency was 1.0 for a 0.0mGy/pulse rate.

To study the effect of pulse frequency on collection efficiency, the above procedure was repeated with different MU/min. The set MU/min were used to calculate pulse frequency using the linear correlation between the two parameters and the fact that the max MU/min corresponded to a 360Hz pulse frequency.

IMRT ion recombination corrections

The following is a brief description of how the 1000 SRS is used in the Octavius 4D system for clinical IMRT QA measurements. 1000 SRS measurements are performed in the Octavius 4D system, which consists of a rotating phantom that keeps the array perpendicular to the beam using an inclinometer attached to the gantry. Prior to a QA measurement, the central chamber of the 1000 SRS is calibrated to a known dose using a reference beam from the linac. A default Co-60 array calibration file, included with the device, has chamber-specific calibration factors, which are scaled using the daily central chamber calibration, thereby calibrating the whole array. Once calibrated, treatment fields are delivered to the 1000 SRS, which measures dose in user defined collection intervals (0.2s for this study) as a function of gantry angle. For each collection interval, a vendor-supplied analysis software (VeriSoft) takes the

measured dose and uses PDDs to back-project a 3D dose throughout the phantom. The total dose, from all collection intervals, is combined and compared to the TPS using a 3D gamma analysis[56, 160].

The daily 1000 SRS calibration is performed at a standard pulse frequency and pulse dose. During a 1000 SRS measurement, the changing MU/min and MLC aperture will cause the pulse frequency and dose to vary across the detector, which will cause changes in the collection efficiency. The changing collection efficiency could potentially cause errors in the IMRT QA measurement. To determine the magnitude of this effect the collection efficiency determined in the previous sections were used to correct clinical 1000 SRS measurements. The details of the IMRT measurements, the corrections, and the IMRT analysis are presented in the subsequent sections.

IMRT Measurements

The effects of ion recombination were studied in seven clinical SBRT plans: four lung, two spine, and one liver plan. The number of available clinical lung SBRT cases far outweighed spine and liver cases, however a variety of plans were chosen to provide a broad case-set for studying ion recombination effects. All plans used RapidArc deliveries. All of the plans were re-planned on the same machine (TrueBeam) for both 6MV and 10FFF energies, using the original clinical dose objectives specified by the physician and a 1.5mm calculation voxel size, per department protocol. Each plan consisted of 4 or 6 arcs. In total, 34 arcs were measured for each energy. Each arc was delivered individually to the Octavius 4D. The measured dose was compared to the dose calculated in the TPS using a 3D gamma analysis. In this work the 3D gamma analysis was performed with a 3%/3mm, 2%/2mm, and 1%/1mm global criteria using a threshold that excluded measurements below 10% of the maximum calculated TPS dose. Finally, the measurements were corrected for ion recombination effects using the procedures in the following sections, and then re-analyzed.

Measurement Corrections

Ion recombination effects in 1000 SRS measurements are caused by the difference in collection efficiencies between the daily array calibration and the IMRT delivery. To correct this effect in the 1000 SRS measurements, the pulse frequencies and pulse dose for both calibration and the IMRT measurement were calculated. The pulse information was used to find collection efficiencies using the measured relationships from the previous section. Finally, the ratio of calibration/measured collection efficiencies were used as correction factors for the 1000 SRS measurements.

First, the pulse dose during 1000 SRS calibration was calculated. The dose to the central chamber was calculated from the TPS. The number of pulses was calculated from the MU/min of the machine and the delivery time (360Hz when using the maximum MU/min).

Pulse frequency and dose during a measurement were calculated using the 1000 SRS measurement file and data from the TPS. The formula for determining the pulse dose during a measurement is shown in Equation 10. This formula assumes a constant pulse dose throughout the individual collection intervals of the Octavius 4D, which was set to 0.2 second for all of the measurements. This limitation in temporal resolution, makes it difficult if not impossible to distinguish separate pulses - only the average pulse frequency during the collection interval is obtainable. As such, Equation 10 does not calculate the actual pulse dose, rather it will calculate the average pulse dose during the 0.2 second collection interval.

Furthermore, the dose rate servo of the TrueBeam may modulate the pulse structures (height and width) to modulate dose rate. This correction technique assumes a change in collection efficiency due to increasing pulse frequency with increasing dose rate; however, the decrease in collection efficiency due to frequency increase may not match the decrease in collection efficiency due to a change in pulse

structure. This is an inherent limitation in this correction technique, which warrants the additional investigation of a simpler correction method.

$Dose_{measured}$ is the amount of dose measured by each chamber during a single sampling time. $MU/min_{measured}$ is the MU/min of the machine during the sampling interval. MU/min_{max} is the maximum MU/min of the machine for each energy: 600MU/min for 6MV and 2400MU/min for 10FFF.

$$\frac{Dose}{Pulse} = \frac{Dose_{measured}}{MU/\min_{measured}} * \frac{MU/\min_{\max}}{360\,pulses/\sec} * \frac{1}{collection\ time} \tag{10}$$

The $Dose_{measured}$ was taken directly from the Octavius 4D measurement files.

The $MU/min_{measured}$ was found using information from the measurement file and the TPS. The TPS stores a table containing MU/min as a function of gantry angle. For each plan, the MU/min vs. gantry angle table was exported from the TPS into the Matlab software. The Octavius 4D system records the gantry angle for each measurement point, which was used to lookup the $MU/min_{measured}$ from the TPS table. Planned MU/min was used instead of the delivered MU/min due to the uncertainty in the Octavius 4D inclinometer reading that resulted in unrealistic pulse doses when measurements were matched with the delivered MU/min from the beam trajectory files. Using the planned MU/min resulted in more realistic pulse doses, especially when there were large changes in MU/min as a function of gantry angle.

Using the data from the previous paragraphs and Equation 10, the pulse frequency and dose at every detector was found for each measurement point. The pulse information was used to calculate collection efficiencies via the measured relationships from the previous sections. Due to the low resolution of the collection efficiency vs. frequency data (Figure *18*), linear interpolation was used to calculate collection efficiencies for frequencies that were not multiples of 60Hz (MU/min not multiples of 100MU/min and 400MU/min for 6X and 10FFF, respectively). The collection efficiencies were used to determine correction factors for each measurement point. Correction factors, shown in Equation 11, were

the ratios of the collection efficiency at the time of daily calibration (CCE), divided by the collection efficiency during the measurement (MCE).

$$Correction Factor = \frac{CCE}{MCE} \tag{11}$$

Each measurement point was subsequently multiplied by its corresponding correction factor.

This correction method provides corrections for changes in both pulse frequency in dose. However, the correction method is cumbersome and may not easily implemented in standard QA practices. Therefore a second correction was tested that involved simply matching the 1000 SRS daily calibration MU/min to the expected average MU/min of the plan. For simplicity the daily calibration correction will be referred to as the "simple" correction, while the Matlab correction will be referred to as the "complex" correction.

The simple correction only accounts for changes in pulse frequency and as such was expected to be less accurate than the complex correction for changes in pulse frequency and dose. To determine the accuracy of the simple corrections, the resulting QA pass rates were compared for both correction techniques.

One issue with the simple correction method is that the TrueBeam linear accelerator only allows the selection of discrete MU/min values during 1000 SRS calibration, making it impossible to exactly match the calibration MU/min to that of the plan. Therefore, a clinical user may have to choose a calibration MU/min that is higher or lower than the plan. To determine whether this choice has a major effect on QA results, the effect of both high and low MU/min corrections were tested and the resulting QA pass rates were compared.

IMRT analysis

After applying the correction factors to the measurements, the Octavius 4D measurements were analyzed in the VeriSoft software package. VeriSoft uses PDDs to project the measured dose from the 1000 SRS throughout the phantom. Dose from each projection is summed, and compared to the dose predicted by the TPS using a 3D gamma analysis. In this work a 3%/3mm, 2%/2mm, and 1%/1mm global criteria were used with a 10% threshold. In total 7 patients were analyzed, with two plans per patient (6X and 10FFF), for a total of 34 arcs per energy. For each arc, an analysis was performed with and without pulse dose corrections and the differences in gamma pass rates were calculated.

To correlate the change in gamma pass rates with plan parameters, the average MU/min and average MLC aperture size were calculated for each arc. DICOM RT plan files were imported into Matlab, where the MLC positions and meterset weights were used to calculate the average aperture size for each arc. Planned MU/min and meterset weights taken from the DICOM files were used to calculate average MU/min. The per-arc parameters were compared to the average change in 1%/1mm gamma pass rate for each plan using a linear regression analysis, and Pearson correlation coefficients were calculated.

Results

Figure 17 shows the collection efficiency of the 1000 SRS LICs for 6MV and 10FFF, averaged over four days. The results are presented without error bars for clarity, however the uncertainty of the measurements are included in the slope uncertainties shown in Figure *18*. The collection efficiencies were linearly correlated with pulse dose. As expected, collection efficiencies increased as both pulse dose and pulse frequency decreased. The change in collection efficiencies as a function of pulse dose were slightly larger for 10FFF, changing by 5.01%/(mGy/pulse) at 360Hz (2400MU/min), compared to 4.44%/(mGy/pulse) for 6X, when a 360Hz (600MU/min) pulse frequency was used.

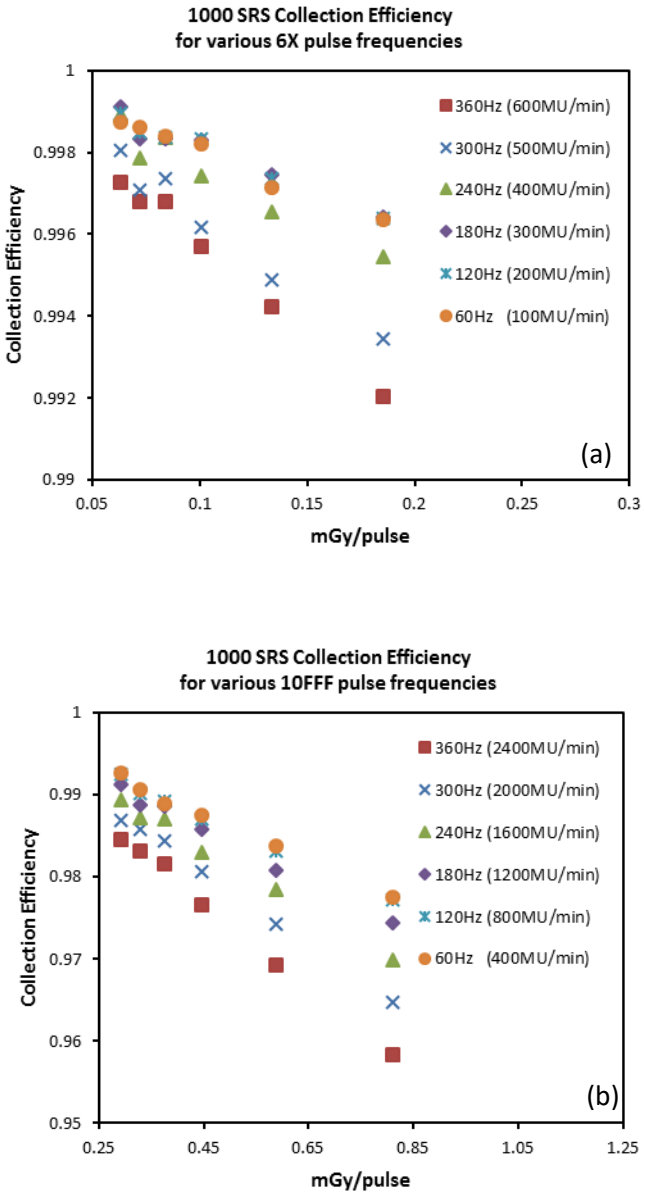

Figure 17: 1000 SRS liquid filled ionization chamber collection efficiencies as a function of pulse dose and pulse frequencies delivered to the detector for (a) 6MV and (b) 10FFF.

The magnitude of the slopes from the collection efficiency versus pulse dose regression analysis are plotted against pulse frequency in Figure *18*. Error bars in Figure *18* are the calculated standard deviations of slope measurements that were repeated over multiple days. This data was used in the ion

recombination corrections to find the change in collection efficiencies for measurements with different combinations of pulse dose and pulse frequency.

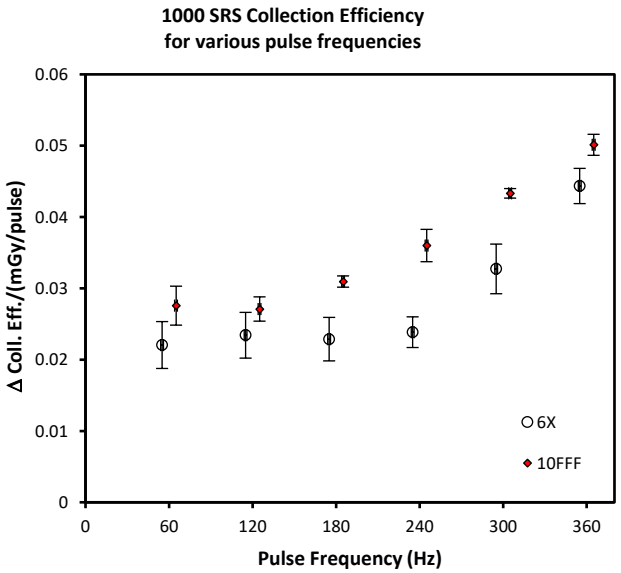

Figure 18: Magnitude of ion recombination effects as a function of pulse frequency. All measurements are for multiples of 60Hz (100MU/min for 6X and 400MU/min for 10FFF) – they have been offset for improved visualization. The vertical axis is the percent change in ion collection efficiency for a given change in pulse dose.

IMRT analysis

The change in 3D gamma pass rates from the ion recombination corrections are shown in Table I for 6MV and 10FFF. For all fields, pass rates improved after corrections. For each plan, the changes in pass rates were averaged over all arcs. The per-plan change in pass rates, found by averaging the pass rate changes for all arcs in a single plan, were used to calculate average (Avg.), maximum (Max.), and standard deviation (σ).

	3D Gamma Pass Rate Changes								
	3%/3mm			2%/2mm			1%/1mm		
Energy	**Avg.**	**σ**	**Max.**	**Avg.**	**σ**	**Max.**	**Avg.**	**σ**	**Max.**
6X	0.07	0.16	0.43	0.40	0.66	1.63	1.17	1.14	3.05
10FFF	0.29	0.40	1.00	1.40	2.09	4.80	4.57	3.71	11.20

Table 4: Changes in gamma pass rates from complex ion recombination corrections. The average (Avg.), standard deviation (σ), and maximum (Max.) changes were calculated from the per-plan changes in pass rates.

Simple corrections produced pass rates both larger and smaller than complex corrections. To quantity the difference in pass rates between the two correction methods, the absolute difference in per-arc pass rates were calculated and the results are shown in Table 5. During simple corrections the nearest possible calibration MU/min was selected to match the plan. Both the results for rounding up (High) and rounding down (Low) to the nearest MU/min are displayed. On average the direction of rounding had less than a 0.5% effect on pass rates. However, selection of the lower calibration MU/min produced pass rates closer to the complex corrections.

		Pass Rate Difference Between Correction Methods								
		3%/3mm			2%/2mm			1%/1mm		
Energy	**MU/min**	**Avg.**	**σ**	**Max.**	**Avg.**	**σ**	**Max.**	**Avg.**	**σ**	**Max.**
6X	High	0.03	0.05	0.1	0.21	0.19	0.5	0.78	0.30	1.2
	Low	0.01	0.02	0.0	0.10	0.06	0.2	0.43	0.28	0.7
10FFF	High	0.01	0.02	0.0	0.27	0.16	0.5	0.98	0.58	2.2
	Low	0.00	0.01	0.0	0.18	0.08	0.3	0.80	0.42	1.7

Table 5: Comparison of the 3D gamma pass rate results obtained after simple and complex ion recombination corrections. The average (Avg.), standard deviation (σ), and maximum (Max.) changes were calculated from the absolute values of per-arc changes in pass rates.

Figure *19* shows dose profiles displaying the effects of ion recombination corrections for a single arc. The dose profile is taken along the C/A of the detector. The profiles are truncated below 10% of the maximum dose, to show the measurements that will be included in the gamma analysis. The uncorrected (measured) and corrected dose planes are compared to the dose predicted by the treatment planning system(TPS). The difference between measured and corrected dose has been plotted as an absolute

difference (M-C) and a relative difference ((M-C)/M*100%). The relative distance represents the magnitude of the ion recombination corrections at those detector locations.

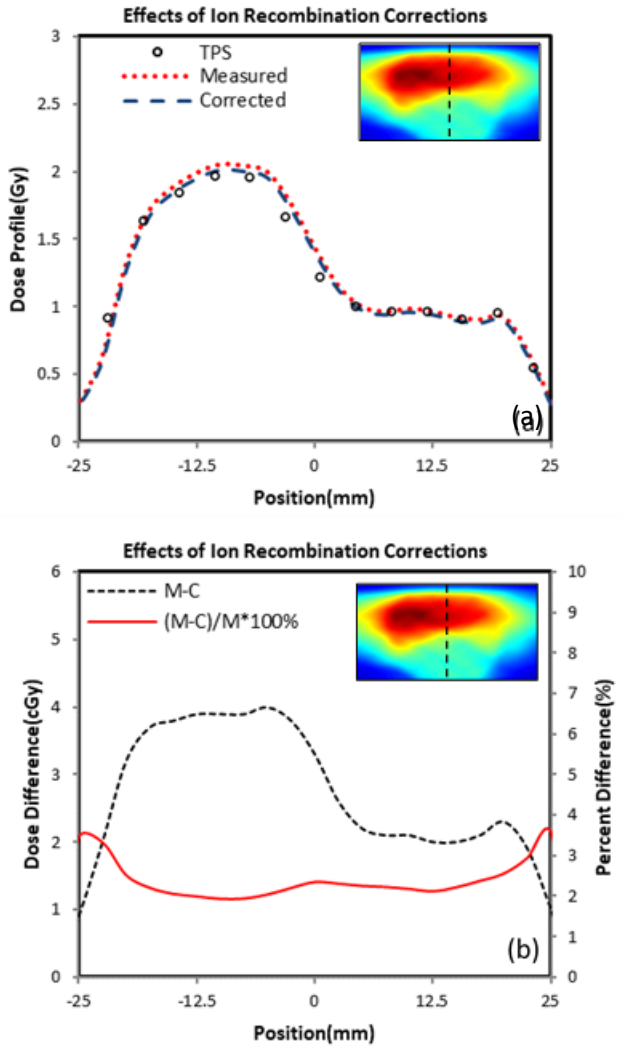

Figure 19: Dosimetric effects of complex ion recombination corrections. (a) Measured and ion recombination corrected dose profiles along the central axis of the 1000 SRS compared to the TPS predicted dose. (b) Difference between measured and corrected profiles. The relative distance is plotted on the right vertical axis.

Figure *20* shows the average per-plan change in pass rates due to recombination corrections plotted against average planned MLC aperture size and average MU/min. The equations from the linear regression are shown on the plots along with the Pearson correlation coefficients. Changes in pass rates were weakly correlated to average MLC aperture size, however they tended to increase as smaller

aperture sizes were used. Changes in pass rates were more strongly correlated to MU/min, increasing as average MU/min decreased.

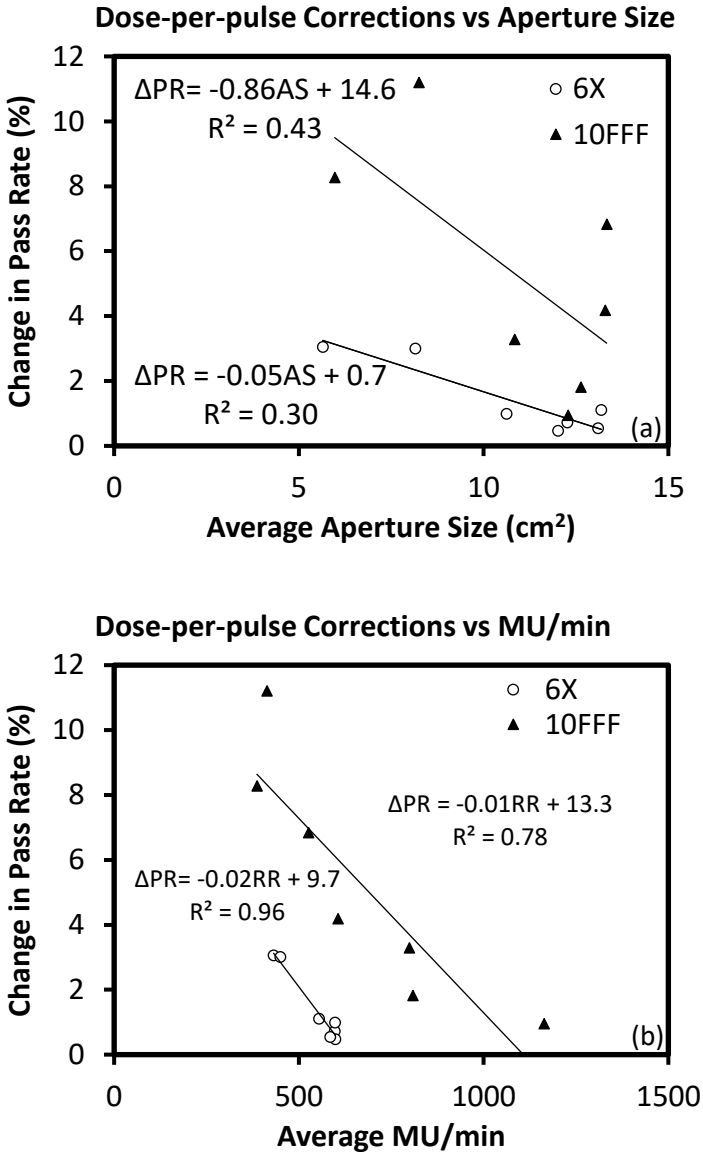

Figure 20: Correlation between changes in 3D gamma analysis pass rates (ΔPR) from pulse dose corrections and (a) average MLC aperture size (AS), (b) average MU/min (RR). 3D gamma analysis was performed using a 1%/1mm criteria with a 10% dose threshold.

Discussion

The linearity between collection efficiency and pulse dose, shown in Figure *17*, matches the relationships found by Chung et al.[152] The magnitude of the slope of the 6MV linear fits was 4.44%/(mGy/pulse) for 360Hz (600MU/min). The slope was close to the manufacturer quoted values of 3.79%/(mGy/pulse) compared to previous publications that found slopes closer to 0.10%/(mGy/pulse) for the 1000SRS[51, 158]. The difference in measured collection efficiencies from previous publications, may be due to the different pulse frequency (400Hz vs 360Hz) and measurement technique (two-dose rate method vs. ion chamber normalization), used in the other studies.

It is important to note that the measured collection efficiencies are specific to the TrueBeam's pulse structure. When operating at the maximum dose rate, the TrueBeam delivers radiation in bundles of 6 equally spaced pulses. When a lower dose rate is used, pulses are dropped. However, the remaining pulses are not uniformly distributed in the bundles. The longer collection time in the Octavius 4D measurements, 0.2 seconds spanning 12 bundles, will provide some averaging against the pulse non-uniformity. However, the collection efficiencies shown in Figure *17* will still be unique to the non-uniform pulse sequence of the TrueBeam, and may not be applicable to other pulse structures.

The pulse structure of the TrueBeam can help explain the change in ion recombination slopes for the different pulse frequencies, shown in Figure *17* and Figure *18*. Chung et al described the difference in the ion recombination slopes between, pulsed and continues beams[8]. The slopes of the continuous beams were steeper than the pulsed slopes. This was due to the buildup of free charge in the chamber, which will increase general recombination, resulting in a higher ion recombination effect.

Figure *18* shows the magnitude of ion recombination magnitude decreasing as pulse frequency decreases. When the TrueBeam is operating at the highest dose rate and frequency, the pulse sequence will be closest to a continuous beam. As the dose rate is lowered, pulses are dropped, reducing the buildup

of free charge, resulting in a more pulsed-like beam and lower slope. Uncertainty in ion recombination magnitudes were primarily due to uncertainties in (1) measuring P_{ion}, (2) 1000 SRS measurements, and (3) the linear regression analysis. Uncertainties in the 6X ion recombination magnitudes were typically larger than 10FFF, due to the increased collection of leakage in longer (lower MU/min) 1000 SRS measurements.

IMRT analysis

The effects of ion recombination corrections on pass rates were larger for 10FFF compared to 6X. The larger changes in pass rates were caused by three differences: 1) the pulse dose at the central axis of the 1000SRS in Octavius 4D was larger for 10FFF(0.760mGy/pulse) compared to 6MV(0.175mGy/pulse), 2) as seen in Figure *18*, a change in pulse dose results in a larger change in collection efficiency for 10FFF, and 3) as seen in Figure *20*, the average MU/min of 10FFF plans deviated further from calibration (max MU/min), compared to 6MV. Changes in pass rates, due to ion recombination corrections, increased with tighter gamma analysis criteria. Tighter gamma criteria has been recommended for SBRT QA (2%/1mm or less), due to the high conformity, small field size, and hypofractionation of SBRT treatments.[161, 162] Therefore, the tighter gamma criteria, where ion recombination corrections are the largest, will likely be used in a clinical analysis.

Ion recombination corrections tend to have a uniform effect on the dose distribution. As seen in Figure *19*, the magnitude of the ion recombination effects ((M-C)/M*100%) are mostly uniform in the high dose region (>10% max dose). There is some non-uniformity in the high dose regions near the high dose gradients of the profiles. During an IMRT delivery, the high dose gradients are created by exposing a MLC edge at that location, which results in a dosimetric penumbra with a spatially varying pulse dose. The change in pulse dose from the calibration conditions are the cause of the increased ion recombination effects at these locations.

Although there is some non-uniformity in ion recombination effects across an IMRT field, the effect tends to be uniform in the high dose region (>10% max dose) – the region that will be included in the IMRT analysis. Across the subset of LICs measuring in the high-dose region of an IMRT distribution, ion recombination corrections tend to be uniform within the subset and dependent upon rep-rate only due to the majority of the dose being delivered to these chambers directly through open MLC apertures at similar doses/pulse. This uniformity of the ion recombination effect is promising, in that it may be possible to apply a single calibration factor, which could account for this effect. The daily calibration of the 1000 SRS presents itself as a natural opportunity for the application of a global calibration factor to account for ion recombination.

The inclusion of an ion recombination correction in the daily calibrations requires an identification of the magnitude of recombination prior to delivery. For this reason, the magnitudes of the ion recombination effects were correlated to average planned MU/min and aperture size – parameters that will change pulse frequency and pulse dose, respectively. Figure *20* shows the results of this investigation, where it was found that the magnitudes of ion recombination effects are more strongly correlated to MU/min.

The stronger correlation suggests that the magnitudes of the ion recombination effects in the 1000 SRS measurements are larger for changes in MU/min, rather than MLC aperture size. The reasoning for the increased effect can be discerned from the measurement and the process used to calibrate the 1000 SRS. The magnitudes of the dosimetric errors due to the ion recombination effect at any point in the measurement is equal to the change in collection efficiency multiplied by the dose per pulse. The 1000 SRS was calibrated at the maximum pulse dose and pulse frequency. Lowering the pulse frequency (MU/min) will change the collection efficiency, while keeping pulse dose large, resulting in a large ion recombination effect.. Lowering the pulse dose (MLC aperture size) will change the collection efficiency, however there will be a smaller ion recombination effect compared with the change in frequency. It is

this characteristic of the ion recombination effects that results in larger dosimetric errors for changing frequency (MU/min).

Fortunately, ion recombination corrections for changing MU/min can easily be included in the daily calibration by matching the calibration MU/min to the average MU/min of the plan. This was implemented in the simple ion recombination corrections. From table 2 it can be seen that the simple corrections greatly reduce the error due to ion recombination effects. There is still some difference in pass rates between the complex and simple corrections. This is due to the residual change in MU/min and aperture size during the IMRT delivery. It may possible to match the average aperture size during calibration to that of delivery. However, the average aperture size of the plan is not readily available from the treatment planning system. The added complexity of calculating aperture size may be an unrealistic burden for clinics looking for a simple fix to ion recombination effects.

Choosing a calibration MU/min higher or lower than the planned MU/min produced pass rates within 0.5%. On average the lower MU/min calibration pass rates were closer to the complex corrections. This is likely due to the increased collection efficiency during calibration from the lower MU/min accounting for the increased collection efficiency from the lower aperture size.

Many clinics use a 6MV flattening filter free mode (6FFF) to treat SBRT patients. The removal of the flattening filter for 6FFF more than doubles the maximum pulse dose of the machine. The pulse dose at the central axis of the 1000SRS in the Octavius 4D during calibration would increase from 0.175mGy/pulse to approximately 0.406mGy/pulse, which is less than the 0.760mGy/pulse of the 10FFF beam. The result is that errors in pass rate due to ion recombination effects would likely fall somewhere between the 6X and 10FFF results. However, the residual error in pass rates after the simple corrections, shown in Table II, were similar for 6X and 10FF. Therefore, the residual error in 6FFF measurements would be expected to follow the same trend.

The discussion of the ion recombination effects relies on the accuracy of the ion recombination corrections, which use measured pulse dose and pulse frequency to calculate collection efficiencies. However, there is an error introduced into the pulse dose corrections when calculating the measurement collection efficiencies. The true pulse dose is needed to determine accurate collection efficiencies. However, only the measured pulse dose, which is effected by the collection efficiency, is available leading to an inherent error in the collection efficiency calculation. The magnitude of this effect can be determined by (1) assuming a true pulse dose, (2) calculating the corresponding measured pulse dose, (3) using Equation 11 to re-calculate true pulse dose from the measured, and (4) finally comparing the result to the original assumed true pulse dose. Using this technique, the error in calculated dose from measured instead of true pulse dose in the ion recombination corrections is less than 0.1% for all energies.

Conclusion

1000 SRS collection efficiencies increased with decreasing pulse dose and pulse frequency. For a given pulse dose and a 360Hz pulse frequency (600MU/min and 2400MU/min for 6X and 10FFF, respectively), the ion recombination was 4.44%/(mGy/pulse) and 5.01%/(mGy/pulse) for 6MV and 10FFF, respectively. On average, applying complex pulse dose and pulse frequency corrections to 1000SRS measurements produced small changes in 6X 3D gamma pass rates (1.17+/-1.14% for 1%/1mm gamma criteria). However, the same corrections resulted in larger changes in pass rates for 10FFF (4.57+/-3.71% for 1%/1mm gamma criteria), which increased when the plan contained small aperture sizes and a strict gamma criterion was used. The magnitudes of the change in pass rates were strongly correlated to pulse frequency (r^2=0.96 for 6X and r^2=0.78 for 10FFF); therefore, a simple correction method was tested where the MU/min of the 1000 SRS calibration was selected to match the average planned IMRT MU/min. On average the pass rates of the simple corrections were within 1% of the complex correction pass rates for all energies and gamma criteria.

CHAPTER 5 IMRT QA ANALYSIS – INCLUDING STRUCTURES IN GAMMA INDEX CALCULATIONS

Introduction

A typical IMRT QA measurement involves delivering a treatment plan to detectors and comparing the dose to that predicted by the treatment planning system (TPS). In practice, if the measured dose deviates too far from the TPS, the plan fails QA and the treatment does not proceed until the failure mode is investigated. This QA paradigm operates under the assumption that the fidelity of measured and predicted dose is correlated to the fidelity of the dose delivered to the patient by the treatment machine and the TPS predicted dose to the patient. In other words, the better the QA result, the closer the delivered plan to the TPS. However, research has shown that this assumption is not valid for common IMRT measurement and analysis techniques. One such publication by Nelms et al. even showed an inverse correlation, with larger deviations in dose delivery having better QA results[163].

In an effort to strengthen the correlation between IMRT QA results and clinically relevant plan metrics, the inclusion of patient anatomical structures in IMRT QA analysis was investigated. Due to the wide range of delivery, measurement, and analysis techniques that are used clinically for IMRT QA, a small subset was chosen for initial investigation. Static gantry head and neck plans were selected to mimic Nelm's investigation. Planar measurements in a rectangular solid water phantom were selected to match TG-119 QA geometry. The gamma analysis was selected as the method of analyzing QA measurements to match TG-119 and Nelms. In the following sections, the technique for including structures in gamma index calculations will be discussed and their effect on the correlation between QA results and clinically relevant plan metrics will be investigated.

Materials and Methods

Prior to including structures in the gamma index calculations, it was necessary to create a test environment where IMRT QA could be simulated in a controlled manner. The test environment was

modelled after the work by Nelms et al. and involved creating multiple treatment machines in the TPS that were slightly modified from one original clinical treatment machine. These modifications would simulate real-world differences between the dose delivered on a treatment machine and that predicted by the TPS. Creating these modified real-world machines in the TPS allowed for the simulation of IMRT QA calculations along with the simultaneous calculation of the delivered and planned dose to the patient. This allowed for the comparison of IMRT QA results to the deviation between planned and delivered patient dose. Specifically, this allowed a Pearson correlation analysis to be performed to determine whether a lower IMRT QA pass rate is correlated with a larger deviation in relevant planning structures (targets and organs at risk).

Four modified machines were created to simulate real-world deliveries. The modifications included: 1) doubling the transmission of radiation through the multi-leaf collimators (MLCs), 2) halving the radiation transmission through the MLCs, 3) smoothing the penumbras that are used to model the cross-beam profiles of the radiation beam, 4) a double-smoothing of the penumbras. The modifications were chosen to match Nelms et al., however they also simulate plausible real-world inaccuracies in beam models. MLC transmission is a commonly adjusted beam model parameter that could easily be set too high or too low. Excessive beam penumbra smoothing is a mistake that can easily be made if the detector used to measure beam profiles is too large, particularly for small fields that are often used in IMRT deliveries.

The original and four modified treatment machines were created in Varian Medical Systems' (Palo Alto, CA) Eclipse treatment planning system. The original machine was created using Varian's golden beam data. The golden beam data is a collection of machine commissioning data that is distributed by Varian that represents an average of multiple clinically commissioned machines. The golden beam data used in this study was for a Varian 21EX machine equipped with a Millennium 120 leaf MLC. The MLC transmissions were adjusted by changing an editable parameter in the machine configuration. The

penumbras were adjusted by running the profiles through a moving-average smoothing algorithm in Matlab. The very smooth penumbras were run through the algorithm a second time. A summary of the changes made to the four modified machines are shown in Table 6.

Machine	MLC Transmission	80% Width at 10cm depth	20% Width at 10cm depth
1(original)	0.016	9.38	10.78
2	0.008	9.38	10.78
3	0.032	9.38	10.78
4	0.016	9.15	11.02
5	0.016	9.02	11.23

Table 6: Changes made to MLC and beam penumbras to create the modified treatment machines.

To simulate IMRT QA on patients, 9 previously treated head and neck cases were selected and the dose to the patients were re-calculated using the 5 machine models. Each plan was originally optimized for a clinical case. The plans were not re-optimized on the new machines, rather the MUs were held constant to match their clinical plans and new dose calculations were performed. Dose was calculated with Eclipse's Pencil Beam Calculation Algorithm(version 8.6.15) using the modified Batho heterogeneity correction method and a 2.5mm grid size. After the dose calculations were performed, the dose to 95% of the PTV (PTV-95%) and the maximum dose to the cord (max_spine) were calculated for each plan. The dose differences between the modified and original plans were normalized to the original planned dose and recorded as a percentage. These metrics were selected because they were heavily prioritized during the head and neck plan optimization. A dose deviation in either of these two values could have significant impact on the tumor control probability or the normal tissue complication probability for an individual patient.

To simulate IMRT QA measurements, the individual fields for each plan were re-calculated on a solid water phantom. Dose planes at isocenter, tangential to the beam direction, were exported as DICOM RT Dose files. The modified dose planes were compared to the original dose planes using a gamma analysis. The gamma analysis is well described in the literature; however, a brief explanation will be

provided due to the importance within this work. During a gamma calculation, each measured point is compared to all planned points. A gamma value is calculated for each comparison. The minimum gamma value at each measured point determines whether it passes or fails. The gamma value calculation is shown in Equation 12.

$$\Gamma(r_m, r_c) = \sqrt{\frac{r^2(r_m, r_c)}{\Delta d_m^2} + \frac{\delta^2(r_m, r_c)}{\Delta D_m^2}}$$
$$\gamma(r_m) = min\{\Gamma(r_m, r_c)\}\forall\{r_c\} \quad (12)$$

In Equation 12, $r^2(r_m, r_c)$ is the squared distance between the measured (r_m) and planned or calculated points, $\delta^2(r_m, r_c)$ is the squared dose deviation between those two points, Δd_m^2 is the squared distance tolerance, and ΔD_m^2 is the squared dose deviation tolerance. The tolerances are user-selected for each analysis. 3mm distance and 3% dose tolerances are often used and is commonly written as 3%/3mm. In addition, it is common to only include points above a certain percentage of the maximum predicted dose in the analysis. 10 percent is often used and when combined with the analysis criteria it is written as 3%/3mm/10% threshold. The results of the gamma analysis are reported as the percentage of points, above the inclusion threshold, that passed the gamma calculation (had a gamma less than or equal to 1.0).

A gamma analysis was used to compare all the simulated IMRT QA measurements by using the dose planes from the original machine as the planned or calculated doses, and the dose planes from the modified machines as the delivered or measured doses. The gamma analysis was performed using a custom designed Matlab code using various percent, distance, and threshold values. The range of values along with the magnitude of steps between the different iterations are shown in Table 7.

A gamma pass rate for each individual field in the plan was calculated and averaged within each plan to get a per-plan pass rate. Finally, a Pearson r-correlation analysis was performed between the per-

plan IMRT QA pass rates and the normalized dose differences in the PTV-D95% and max_spine metrics between the original and modified plans.

Parameter	Minimum	Maximum	Step
Threshold	5%	90%	5%
DTA	1.0mm	3.0mm	0.5mm
Dose Deviation	0.50%	5%	0.50%

Table 7: Various parameters used in the gamma index calculations.

After performing a traditional gamma analysis, a second gamma analysis was performed that included PTV and spine structures from the TPS. For each patient, the DICOM structure and plan files were exported from the TPS. The IMRT QA DICOM dose, structure, and plan files were imported into author-developed Matlab software. Details of these files along with the Matlab code used to manipulate them are presented in Appendix A. The structures were used to vary the importance of each point in the field, the strictness of the analysis criteria, and also to determine which points should be included in the calculations. A schematic showing the different workflows for the traditional versus structure-dependent gamma analysis is shown in Figure 21.

Four different methods for including structures in the gamma index calculations were investigated:

1) Binary – Measurement points would only be included in the final pass rate calculation if they fell within the beams eye view projection of the structures. Standard gamma index criteria was used.
2) Structure Falloff – All the points within the structure have equal weighting when calculating the per-field gamma pass rate. Points outside the structure have weighting relative to their distance from the structure.
3) Structure thickness weighting - Weighting each location's contribution to the per-field pass rate based on the BEV thickness of the structure at that location.

4) Structure dependent Gamma Index criteria – Adjusting the Gamma Index distance-to-agreement and dose deviation criteria at each location based on the BEV thickness of the structure at that location.

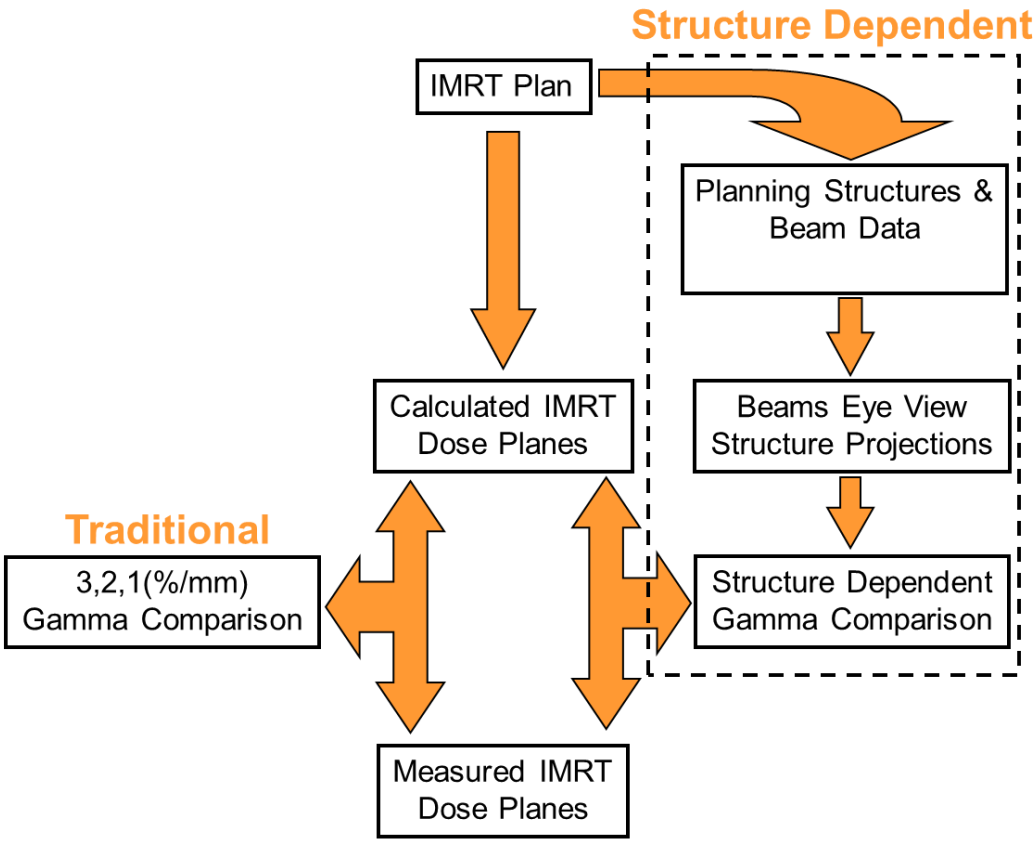

Figure 21: Schematic showing the workflow for a traditional versus structure-dependent gamma analysis

The simplest way that structures can be included in the gamma analysis is to use them to determine which measurement points should be included in the final analysis. From a programming standpoint, this was accomplished by creating a binary mask for each structure where the value was "1" if the point fell within the structure and "0" if the point was outside the structure. For this study, the spinal cord and PTV structures were considered. The spinal cord was chosen for normal tissue as it is typically

the most critical dose limiting structure. An overdose to the spinal cord can cause catastrophic complications to the patient and in most cases is deemed clinically unacceptable.

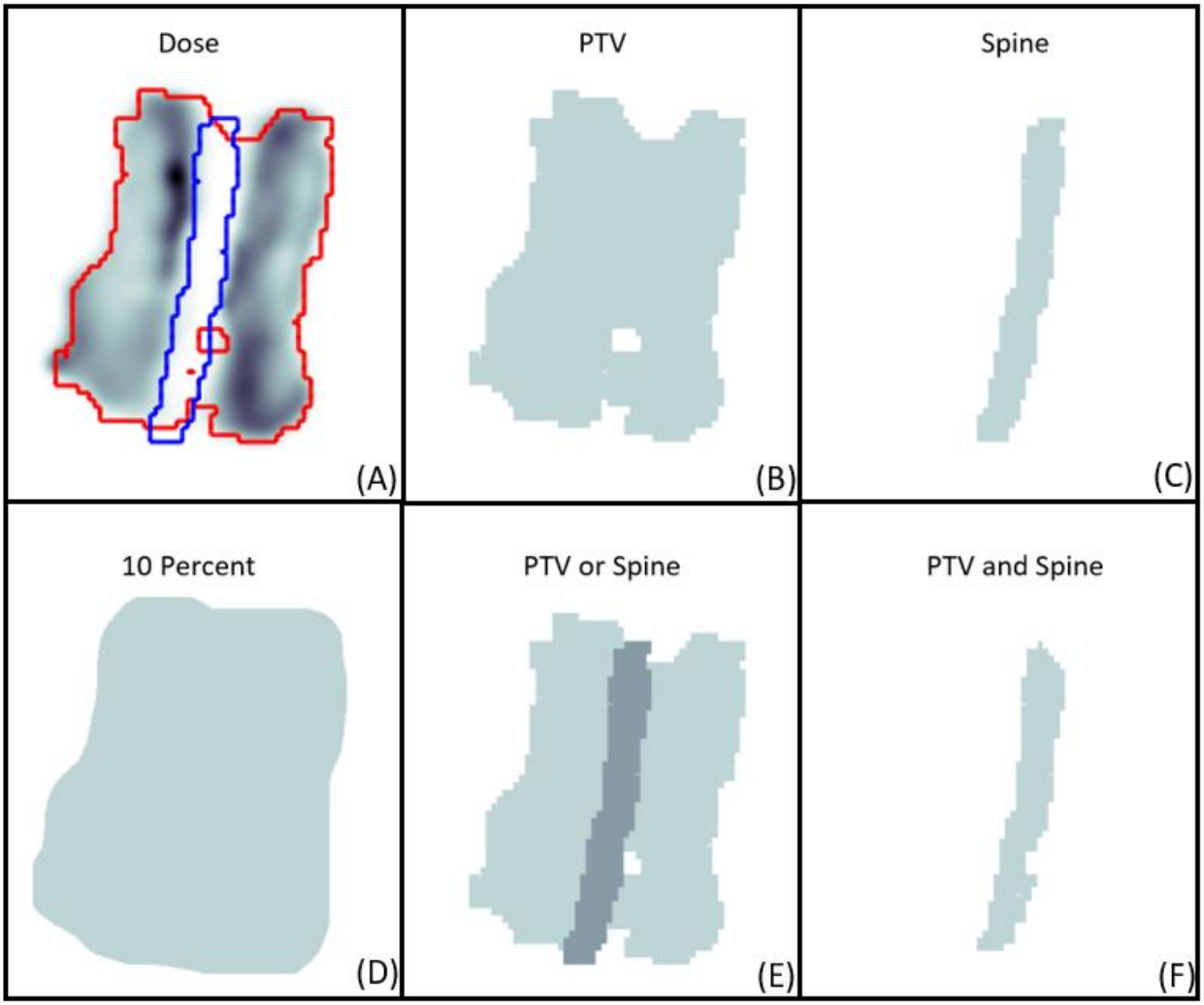

Figure 22: Binary structure masks used to delineate region included in the gamma calculation. (A) Overlay of the structures on a planar dose distribution, (B) PTV only structure, (C) Spine only structure, (D) traditional 10 percent mask, (E) PTV or Spine structure, (F) PTV and Spine Structure.

The PTV and spinal cord structure maps were combined using logical operators to designate four different regions that could be included in the gamma calculation: 1) spine only, 2) PTV only, 3) Spine and PTV, 4) Spine or PTV. An example of the four masks are shown in the Figure 22. The masks were used to recalculate pass rates, which were subsequentially used to recalculate r-values.

One fundamental drawback to restricting the analysis using a structure mask is that the radiation field adjacent to a structure, that will contribute dose to the structure due to scatter, will not be included in the analysis . The dosimetric accuracy in this region, just outside the target, can often be the most important due to the task of delivering dose to the target, while sparing the adjacent normal tissue. The balance between coverage and sparing is accomplished with high dose gradients, which are both difficult to approximate in the planning system and deliver by the machine.

Partially due to the inherent uncertainties in this region it is typically included in the analysis by using a 10 percent threshold. As mentioned previously, the 10 percent threshold includes points outside the structures with equal weighting. However, the radiation spatial dose deposition is not a square function, rather it typically approximated by a Gaussian type distribution[164]. Therefore, the closer the point is to the structure, the larger fraction of its dose will scatter into the structure. These concepts motivated the inclusion of points outside the structure in the gamma analysis and the weighting of their contributions based on their proximity to the structure.

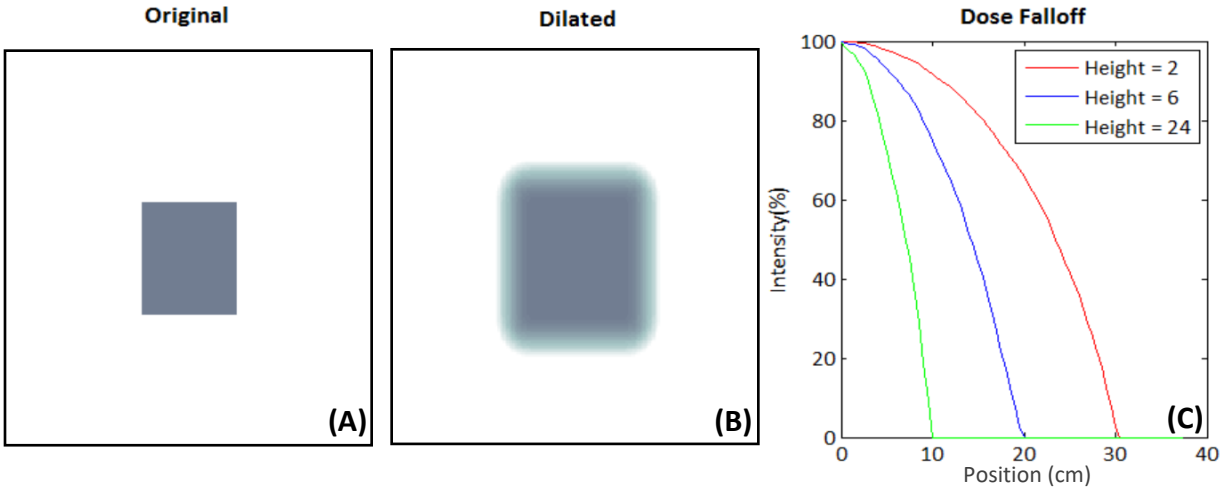

Figure 23: Effect of image dilation using the ball morphological structure element. (A) Original image, (B) dilated image, (C) dilated intensity falloff outside the original image for different ball height parameters.

To include the additional measurement points, the previously generated structure masks required expansion with a Gaussian-like falloff. This was accomplished using a Matlab dilation tools, specifically the

imdilate function. The function dilates an image using a morphological structure element. In this instance, the structure element was a two-dimensional matrix applied to each pixel in the original image. Based on the intensity of the pixel, the neighboring pixels may be increased causing the image to expand.

A “ball” structure element was selected for this research. The structure had two parameters: radius and height. The radius described how far away the dilation occurs from each pixel. The height described the falloff of the dilation relative to original pixel. The effect of the ball dilation is shown in Figure 23. The radius and height parameters were adjusted to provide falloff extending to 1.0, 2.0, and 3.0cm (Figure 23.c). Mathematically the dilation was applied to the structure masks to create a normalized weighting mask, with any point inside the structure having a weighting of one. The weighting value of each passing point was totaled and divided by the total weighting to obtain a pass rate. Subsequently, r-values were calculated to compare the weighted pass rates to plan deviations.

Thus far the structure contours have only been used as binary masks to denote the outside border of the contour. Although this can help to isolate what portion of a field may contribute dose the structure, the weighting is uniform within the structure in the case of binary masks, and dictated by distance for the falloff masks. However, the structures can also be used in a non-binary fashion to weight the field within the structure proportionally to the structure thicknesses (like the falloff). In addition, the structure thicknesses can be used to adjust the gamma criteria for a point to be considered passing within the field. For example, the portion of the field near the spinal cord could have a strict passing criterion of 1%/1mm, while the outer edge of the field could have a laxer 3%/3mm criterion. These two weighting methods, using structures to weight how much individual points accounts for the overall pass rate and weighting the strictness of the gamma criteria at individual points, were both were investigated.

The work started with weighting the contributions of each point for the overall pass rate. To begin, the normalized thickness of the structures was calculated for each field. The results were a

structure map of the fields with a value of 1 at the thickest part of the structure, 0 outside the structure, and some scaling in between the extremes. Three different structure maps were considered: PTV, SPINE, and OR. The AND mask was removed from further analysis as it did not show any major advantage in previous sections. In the case of the OR structure, the PTV and spine contours were added together, and the combined thickness was normalized to one.

The importance at each location inside the structures were calculated using the normalized thickness and Equation 13.

$$Importance = 1 + Slope * (Normalized\ Thickness)^{Power} \quad (13)$$

The importance points outside the structure were set to zero. Pass rates were calculated in a similar fashion to falloff masks, where the importance of each passing point was added together and divided by the total importance of all points summed across the entire field. The pass rate calculations were performed for different slope and power constants ranging from 0 to 5. Finally, r-values were calculated that compared the per-plan pass rates for each combination of constants to the plan deviations.

Next, the structures were used to vary the Gamma Index analysis criteria (distance to agreement and dose deviation). Like the previous work on importance, the thickness of the structures the beam passed through was calculated at each location in the field and then projected onto the exported dose planes. Each structure was normalized so that the thickest part of the structure had a value of 1. Also, if multiple structures added to a number greater than 1 at a single location in the plan, the structure thickness was set to the maximum value of 1. Figure 24 illustrates an example of structure dependent passing criteria for two fields. In both fields, the outline of the PTV and the Spinal Cord are shown. The most significant part of the fields is where the structures overlap. The combined thickness of the structures is largest at the overlap and therefore a strict passing criteria of 1%/1mm is used. The less

significant outer areas of the fields that do not include planning structures have a more relaxed 3%/3mm passing criteria. A 10 percent threshold was used for an inclusion criterion.

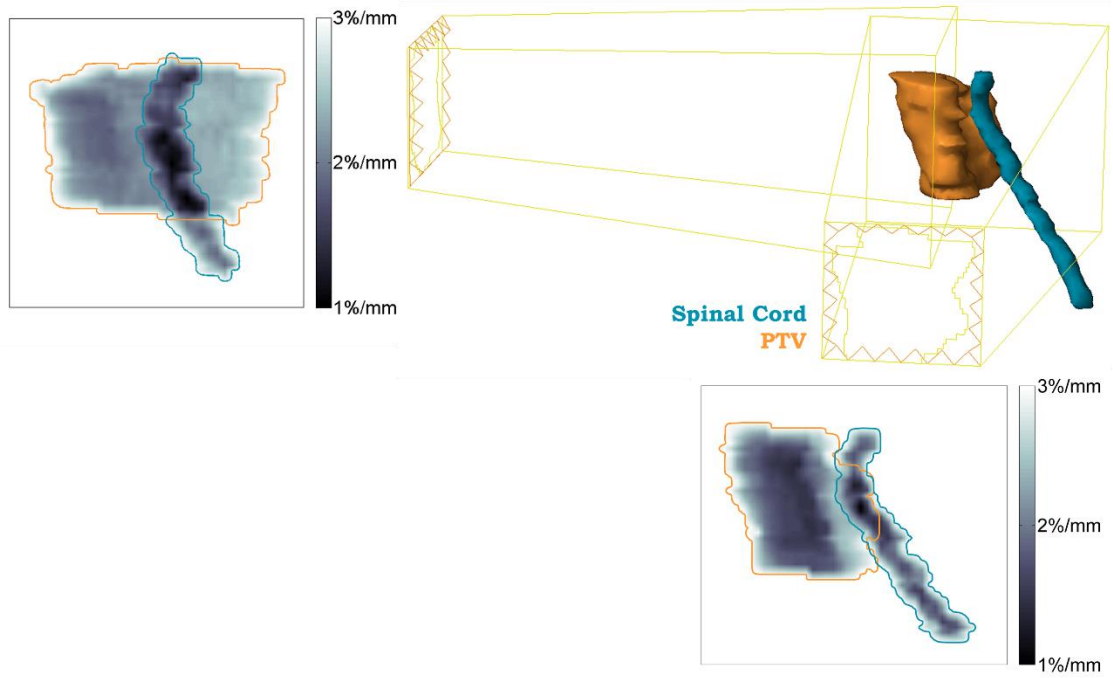

Figure 24: Varying the gamma analysis dose and distance tolerances proportionally to the path length through planning structures. Target (PTV) in orange and spinal cord in blue.

The first structure dependent passing criteria were scaled linearly with the path length through the structures. Additional calculations were also performed with a structure dependent passing criterial that scaled as a power function of the normalized path length. By scaling the passing criteria with progressively higher power functions, this served to further emphasize the regions of the field that passed through the critical structures. An example of the structure dependent passing criteria scaled as a power function of 1 (linear) and 3 (cubic) is shown in Figure 25.

For each structure dependent passing criterion, the pass rates of all the modified IMRT QA plans were re-calculated followed by Pearson r-correlation analysis with the PTV-D95 and max_spine metrics. Finally, the pass rates of the different calculations were compared to discover overall trends in the data

and the Pearson r-correlation values were compared to quantify the level of correlations with clinically relevant plan metrics.

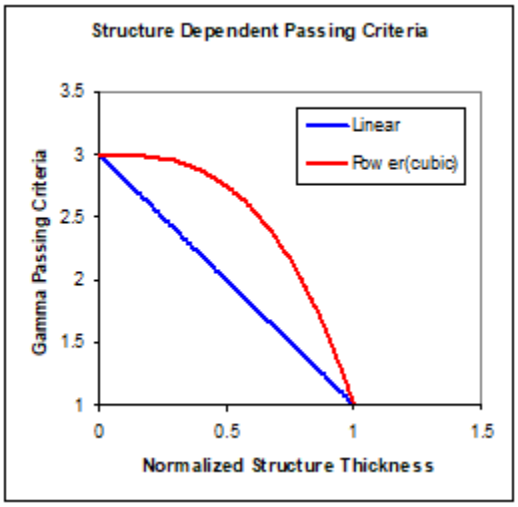

Figure 25: Scaling the structure dependent passing criteria as a function of normalized structure thickness in the beams-eye-view projection of a treatment field.

Results

The gamma index criterion that produced the best Pearson r-correlation coefficients for the traditional gamma analysis was 3mm/1.5%/5% threshold. For this criterion, the r-values for the max_spine was r = -0.847 and PTV-95% was r = -0.849. For comparison, the r-values for the commonly used 3%/3mm/10% threshold criterion were r = -0.717 for max_spine and r = -0.729 for PTV-95%.

To examine the relationship between r-values and the different gamma parameters (threshold/DTA/percent), one parameter was held constant while the other two were varied. To start, the distance criteria was set to 3mm, while the threshold and dose difference criteria were varied. The resulting r-values are shown in Figure *26*.

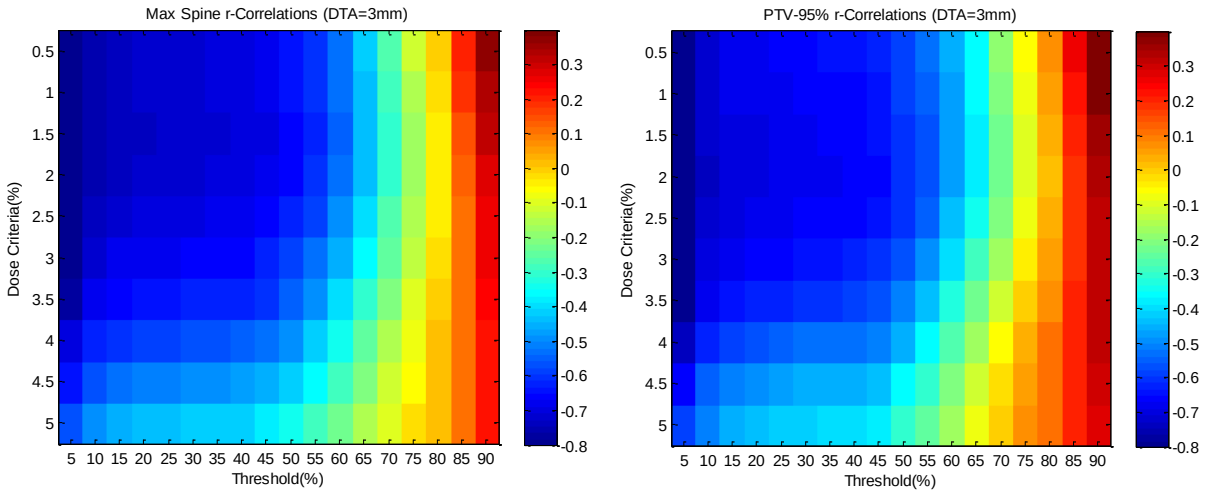

Figure 26: Pearson r-correlation coefficients between per-plan IMRT QA Gamma Index pass rates and dose received by 95% of the PTV (PTV-D95%) and the maximum dose to the spinal cord. The distance criterion in the Gamma Index was set to 3mm, while the dose criteria and threshold criteria were varied.

After examining the effect of varying threshold and dose criterion on the r-values, the same process was repeated for the distance criterion. The threshold was set to 5%, and the distance-to-agreement and dose criterion were varied. The results are shown in Figure *27*.

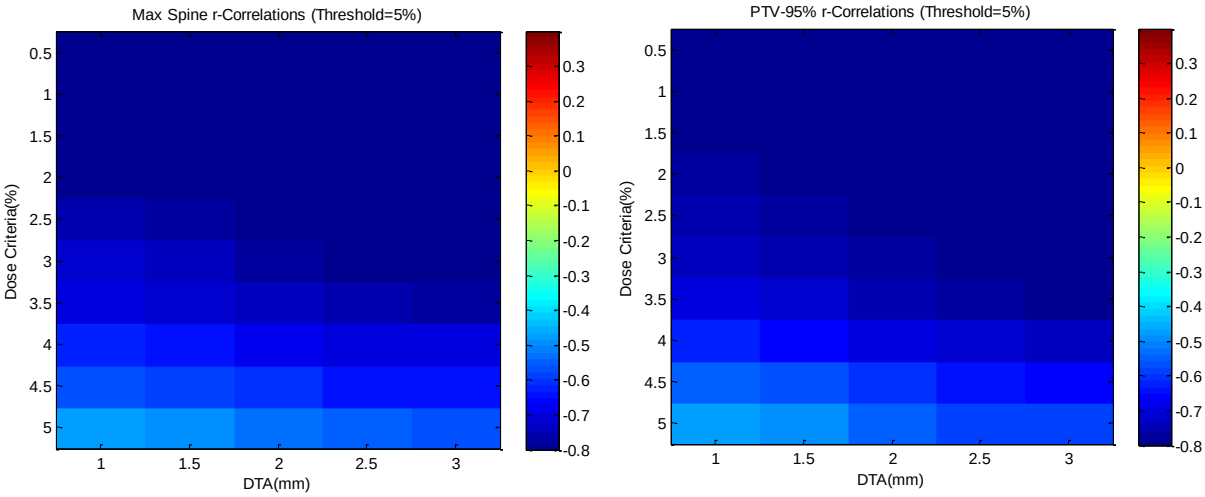

Figure 27: Pearson r-correlation coefficients between per-plan IMRT QA Gamma Index pass rates and dose received by 95% of the PTV (PTV-D95%) and the maximum dose to the spinal cord. The threshold was set to 5%, while the dose and distance-to-agreement criteria were varied.

The resulting r^2-values from using various structure dependent masks are show in Figure 28 and Table 8. The only mask that showed consistent improvement was the spine mask for the maximum spine value. Unfortunately, the spine mask resulted in a drop in r-value for the PTV-95%. The AND mask also showed an improvement in the maximum spine r-values. However, the improvement was less than the spine mask and the detriment to the PTV-95% r-value was greater.

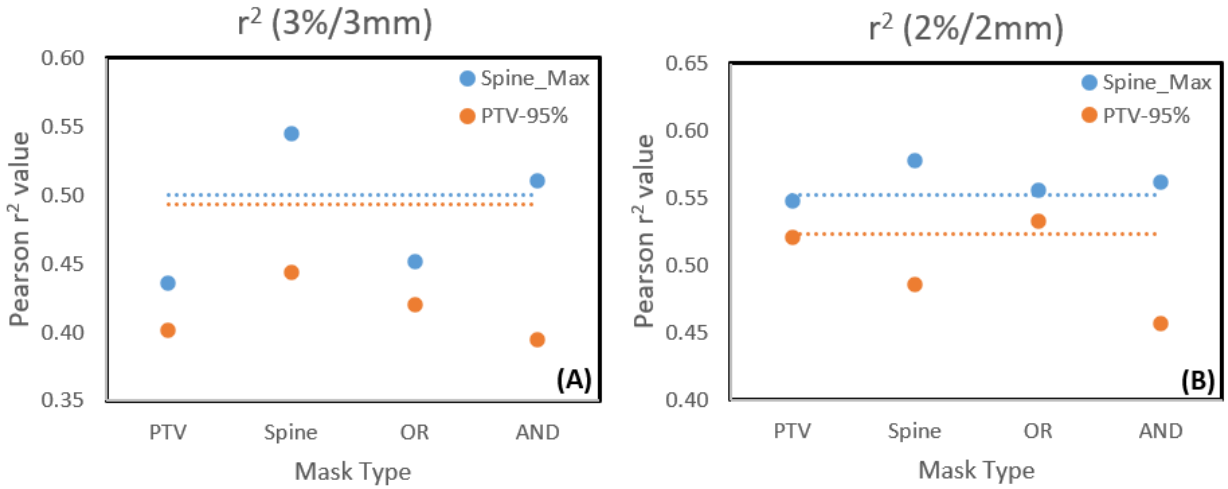

Figure 28: r^2-values comparing pass rates with plan deviations for different binary masks. (A) r^2-values with 3%/3mm, (B) r^2-values with 2%/2mm.

	Pearson (r^2) correlation values			
	2%/2mm		3%/3mm	
Binary Mask	**Max_Spine**	**PTV-95%**	**Max_Spine**	**PTV-95%**
PTV	0.547	0.521	0.436	0.401
Spine	0.577	0.486	0.545	0.443
Either	0.555	0.532	0.451	0.420
Both	0.562	0.456	0.510	0.395
10% Threshold	0.552	0.523	0.500	0.493

Table 8: r^2 values correlating pass rate with plan deviations. Pass rates were calculated using different masks to determine which points were included in the analysis.

The results of the r^2-value calculations for falloff masks are shown in Figure 29 and Table 9. The largest r-values for the spine are achieved when using the SPINE and mask with a 2%/2mm analysis criteria. For this combination of criteria and masks, the r-values showed little sensitivity to the falloff distance. However, the 1-2cm falloff masks produced better r-values than the structure masks for most

cases, while the 3cm falloff masks were better for all cases. This suggests that the optimal advantage for including falloff points, when analyzing the maximum dose the spine occurs, within 2-3cm outside the structure. A portion of this region, between the PTV and spinal cord, is typically characterized by high dose gradients that are used to lower the maximum dose to the spinal cord, while maintaining PTV coverage. It is not surprising that errors in the region could lead to changes in spinal cord dose, and therefore this area should be included in the analysis.

The PTV metric showed similar trends to the spinal cord; increasing r-value as the falloff increased. For 3%/3mm, the falloff masks resulted in larger r-values than all structure masks. At 2%/2mm, the advantage was diminished with some 1cm and 2cm falloff masks underperforming. However, all 3cm falloff masks produced larger PTV r-values than the 2%/2mm structure masks. Similar to the threshold analysis, the r-values increased with falloff when more points were included in the calculation. The PTV and OR masks had larger r-values for 3%/3mm, however all masks tended to perform equally well for 2%/2mm. The 2%/2mm r-values were larger than their 3%/3mm counterparts.

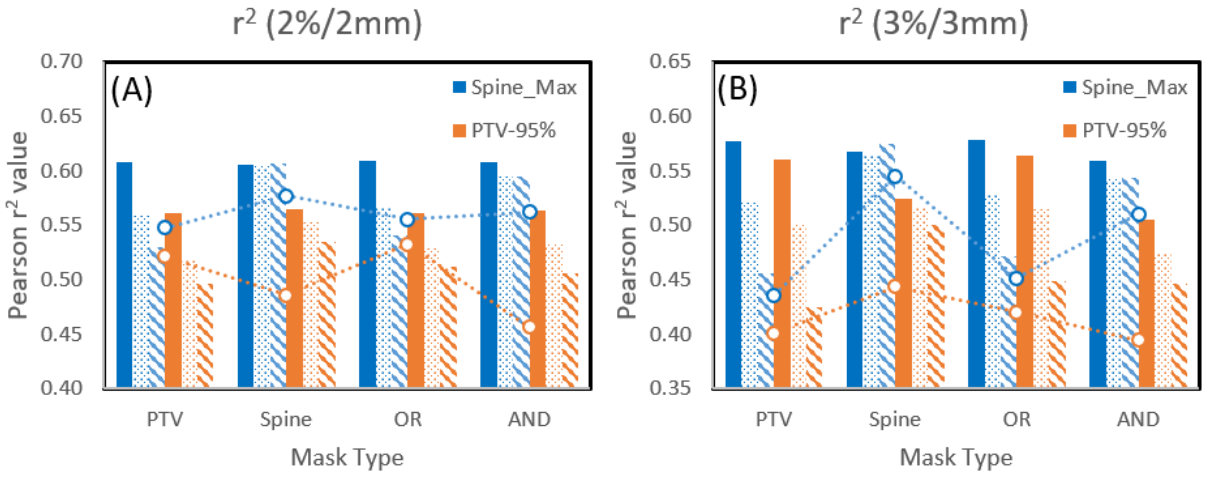

Figure 29: R^2-values for structure mask thresholds with falloff point inclusion. Dashed lines are structure masks with no falloff. Solid bars are 3cm falloff. Dotted bars are 2cm falloff. Striped bars are 1cm falloff. (a) 2%/2mm, (b) 3%/3mm.

		Pearson (r^2) correlation values			
		2%/2mm		3%/3mm	
Binary Mask	Falloff(cm)	Max_Spine	PTV-95%	Max_Spine	PTV-95%
PTV	3	0.608	0.561	0.578	0.561
	2	0.559	0.518	0.521	0.500
	1	0.530	0.496	0.455	0.425
	None	0.547	0.521	0.436	0.401
Spine	3	0.606	0.564	0.568	0.525
	2	0.605	0.552	0.565	0.516
	1	0.606	0.534	0.574	0.501
	None	0.577	0.486	0.545	0.443
OR	3	0.609	0.561	0.578	0.564
	2	0.566	0.528	0.529	0.514
	1	0.541	0.512	0.472	0.449
	None	0.555	0.532	0.451	0.420
AND	3	0.608	0.563	0.559	0.505
	2	0.595	0.533	0.542	0.475
	1	0.595	0.506	0.544	0.446
	None	0.562	0.456	0.510	0.395

Table 9: Correlation coefficients between DVH deviations and gamma pass rates calculated using a structure mask threshold with the inclusion of some points outside the structure. The falloff term represents how far outside the structure mask that points are included in the calculation

The results of the r^2-values for the structure-weighted importance calculations are shown in Figure 30 and Figure 31. The first column of all the plots have a slope of zero. Per Equation 13, this results in an importance of 1 across the entire mask, which creates a binary mask. Therefore, the first columns match the data shown in Table 8.

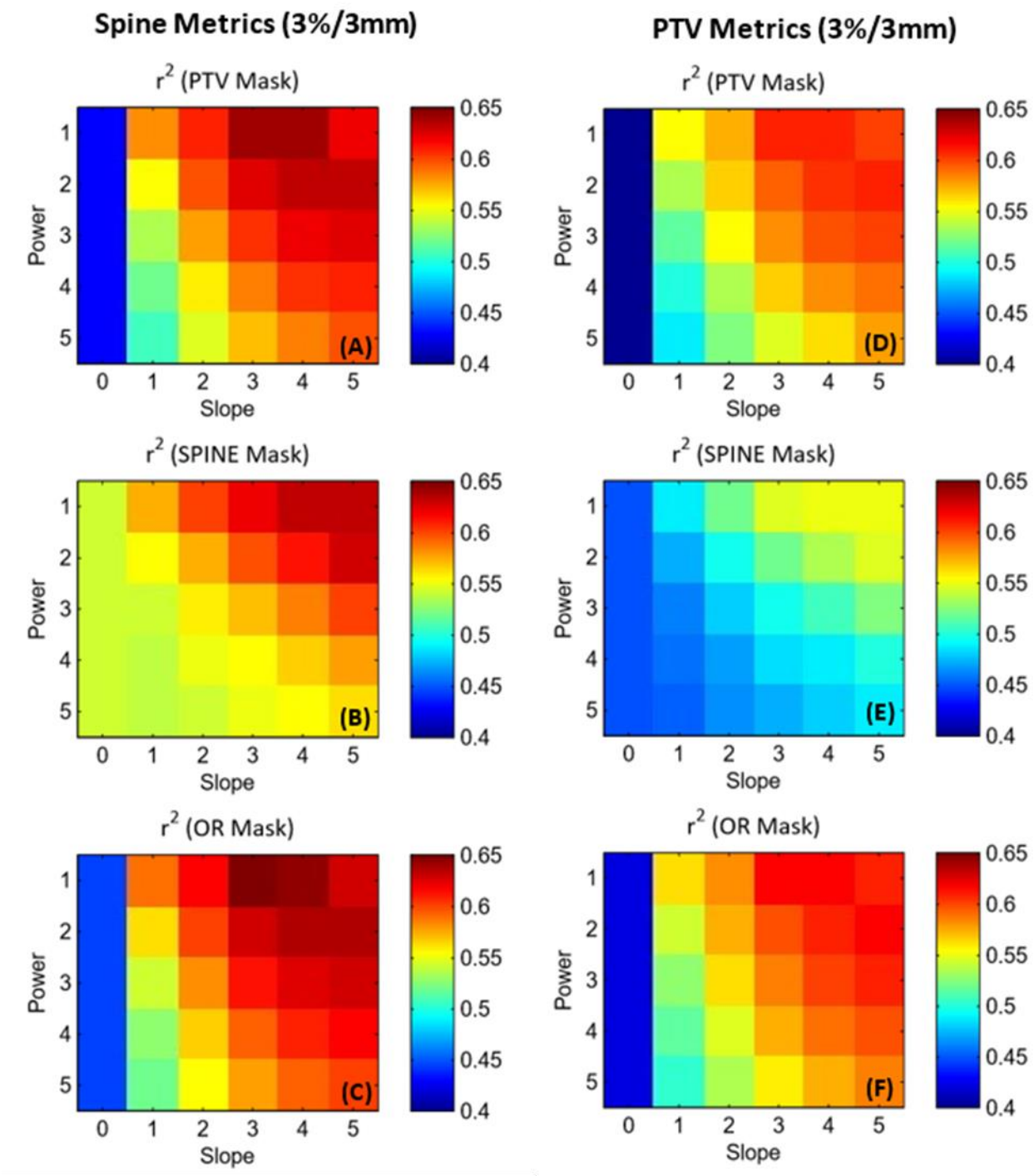

Figure 30: Spine (A-C) and PTV (D-F) r^2-values for structure dependent importance weighting of each point in a 3%/3mm gamma calculation.

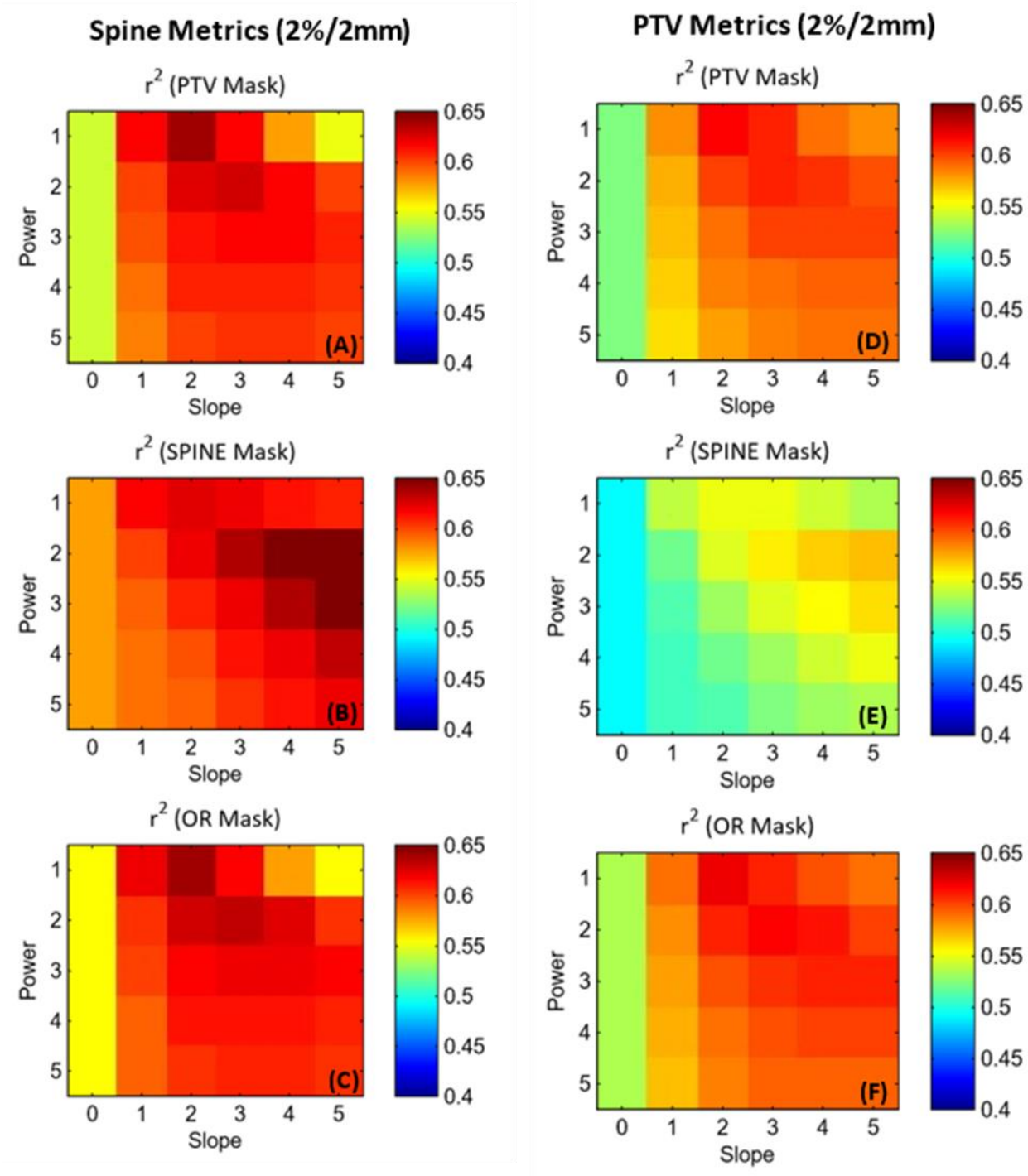

Figure 31: Spine (A-C) and PTV (D-F) r2-values for structure dependent importance weighting of each point in a 2%/2mm gamma calculation.

The comparison between deviations in the maximum dose to the spinal cord and the per-plan pass rates using three common clinical gamma analysis and the linearly scaled structure dependent

gamma criteria are shown in Figure 32 and Figure 33, respectively. The corresponding Pearson r-correlation coefficients are shown in Table *10*. The comparison between deviations in dose to 95% of the PTV and the per-plan pass rates using various gamma analysis criteria are show in Figure 34 and Figure 35. The corresponding Pearson r-correlation coefficients are shown in Table *11*.

Utilizing a higher power scaling technique increased the correlation between passing criteria and dose objectives. Correlation coefficients increased an average of 0.008 between linear and cubic scaling techniques. However, using a power scaling technique larger than cubic did not improve the correlation coefficients.

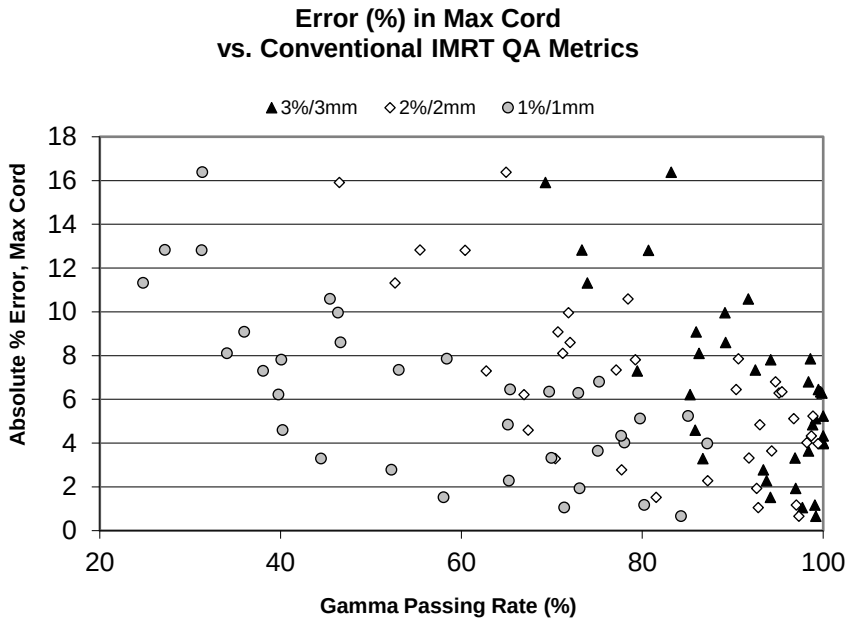

Figure 32: Per-plan IMRT QA pass rates versus deviations in maximum dose to the spinal cord for different gamma analysis passing criteria.

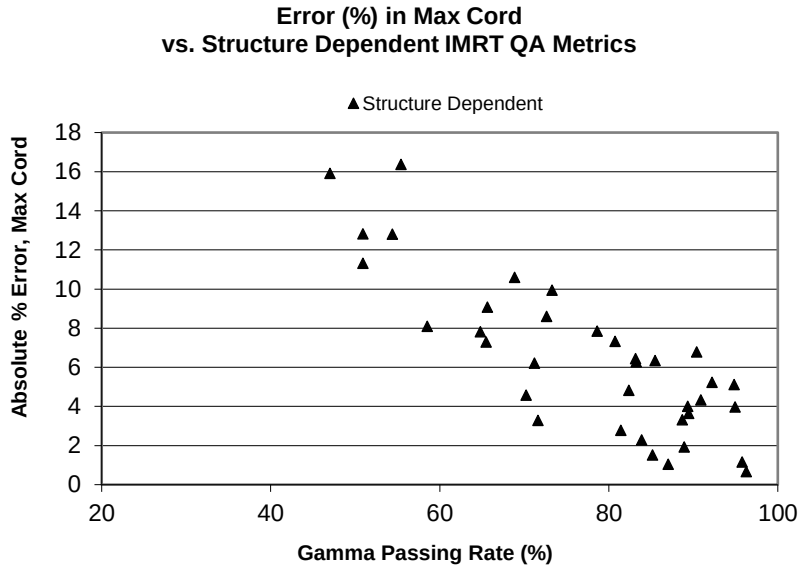

Figure 33: Per-plan IMRT QA pass rates versus deviations in maximum dose to the spinal cord for structure dependent gamma analysis passing criteria.

	Pearson r-correlations between IMRT QA Pass Rates & Max Cord Error			
Analysis Criteria	**3% / 3mm**	**2% / 2mm**	**1% / 1mm**	**Structure Dependent**
Pearson r - values	-0.717	-0.720	-0.750	-0.831

Table 10: Pearson r-correlation coefficients (r-values) between per-plan IMRT QA pass rates and deviations in maximum dose to the spinal cord for various gamma analysis passing criteria.

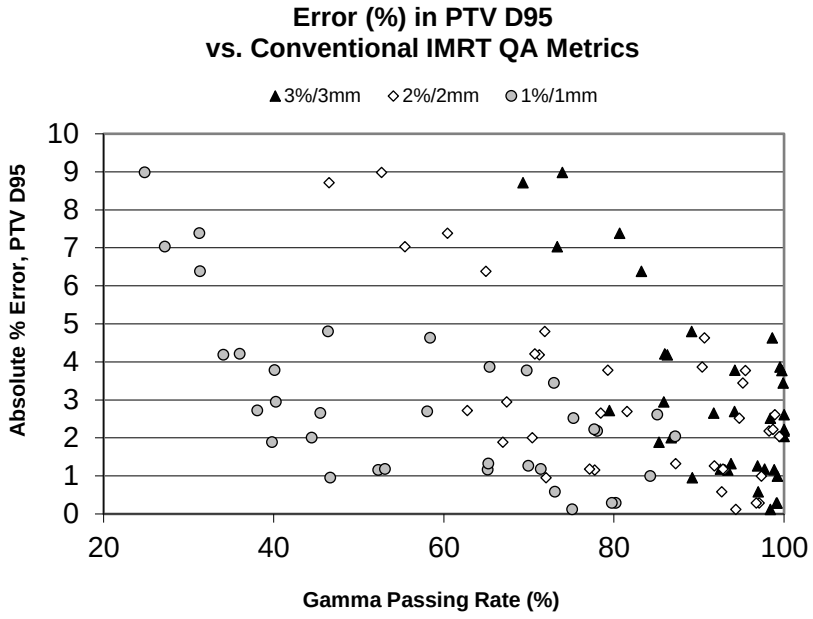

Figure 34:Per-plan IMRT QA pass rates versus deviations in the dose to 95% of the PTV for different gamma analysis passing criteria.

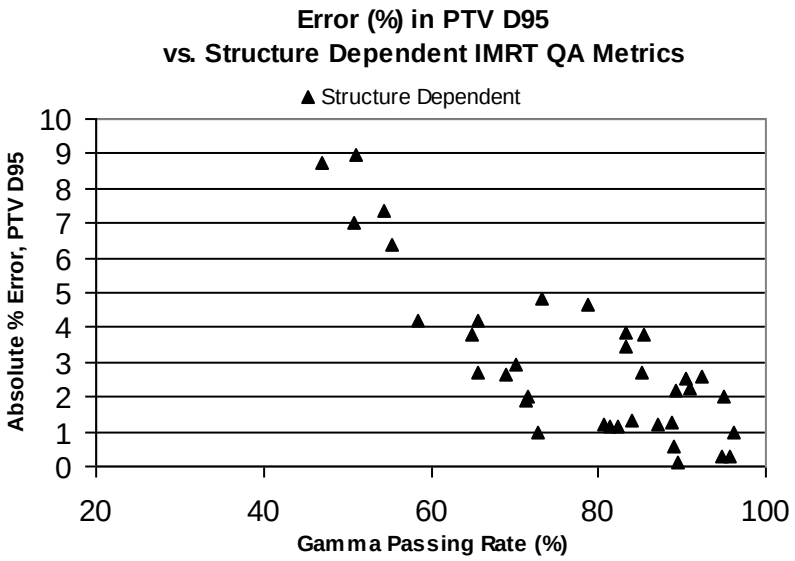

Figure 35: Per-plan IMRT QA pass rates versus deviations in the dose to 95% of the PTV for structure dependent gamma analysis passing criteria.

	Pearson r-correlations between IMRT QA Pass Rates & PTV D95 Error			
Analysis Criteria	**3% / 3mm**	**2% / 2mm**	**1% / 1mm**	**Structure Dependent**
Pearson r - values	-0.729	-0.703	-0.711	-0.812

Table 11: Pearson r-correlation coefficients (r-values) between per-plan IMRT QA pass rates and deviations in dose to 95% of the PTV for various gamma analysis passing criteria.

Discussion

Figure 26 shows that lower thresholds produced the best correlations. Above a 75-80% threshold, the correlation breaks down entirely. For those thresholds, a large portion of the treatment field that passes through the spine and PTV has been ignored, causing the correlation to break down.

For the thresholds below 40%, the correlation may more strongly depend on the portions of the field that fall near a target-critical structure junction. Some example locations for H&N cases would be between PTV-cord, PTV-parotid, and PTV-normal tissue. At these locations, dose gradients are usually high, resulting in low doses to the OAR and just enough coverage on the PTV to obtain a good DVH. These voxels play an important role in determining the max dose to the spine and the coverage of the PTV. As

the threshold increases, fewer of these points are included in the analysis, causing the correlation to break down.

For a given threshold, a stricter dose criterion tended to produce stronger correlations. To visualize the reason why this happens, it is useful to look at the 0.5%/3mm/10% threshold and the 3%/3mm/10% threshold data on the same plot (Figure 36). The 3%/3mm data has a considerable amount of points above 95% and a few that are 100%. The truncated nature of gamma analysis (with a maximum 100% pass rate), may lead to poor correlations with plan metrics due to too many QA results hitting this upper limit.

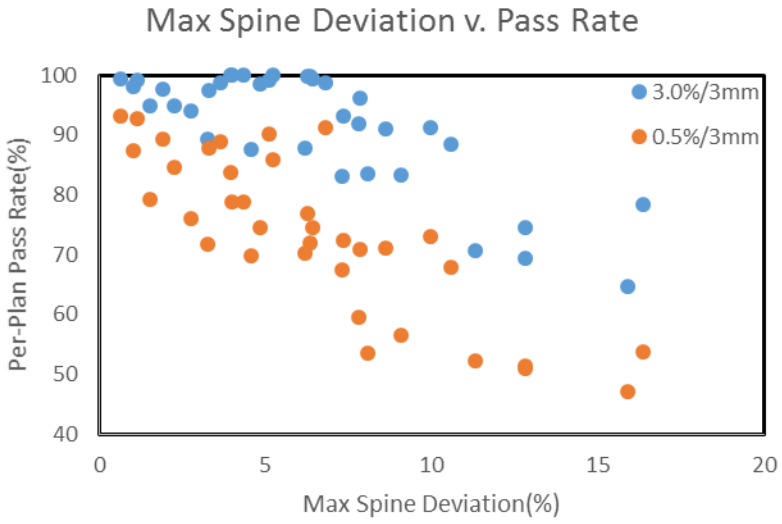

Figure 36: Comparison between per-plan Gamma Analysis pass rates for 0.5%/3mm/10% threshold and 3%/3mm/10% threshold analysis criteria.

For the head and neck cases in this study, the DTA criteria did not have a strong effect on the r-correlations and AUCs. However, in general the smaller the DTA the worse the correlation. This may have been due to the types of modifications that were introduced into our machines. The modifications were spatially "smooth"; they had a gradual effect on the overall dose distribution. If the modifications had a

higher spatial gradient (moving an entire leaf bank), then modulating the DTA criteria may have a greater effect on the pass rate correlations to dosimetric plan metrics.

There are a few features of the masks, shown in Figure 22, which can be used to understand their behavior. The PTV and 10 Percent masks look very similar with a few notable differences in that the 10 percent mask is slightly larger and filled in the middle. The size comes from the dosimetric objectives of the radiation treatment. If the goal is to treat the PTV with full dose, the 10 percent line must trace outside the PTV, thus the 10 percent mask is larger.

The middle filling of the 10 percent mask is a product of the technique used in its creation. The technique starts by determining the area in which dose is greater than 10% of the maximum. Instead of only using this area as the mask, it also includes any points in between two areas that are greater than 10% of the maximum dose. The idea is that when analyzing an IMRT field it is equally important to look at where the radiation is and is not being delivered. If a low dose region exists in between two high dose regions, it is likely that there is a critical structure which is being avoided. Figure 22.a demonstrates this phenomenon where the dose surrounds the spinal cord. If only the greater than 10% areas were considered, the dose to the spinal cord would be ignored, which is not ideal.

The PTV and OR masks follow the same trend as the previous threshold analysis: as more points are included in the analysis, the r-values improve. Furthermore, when a spine mask was used, the r-values improved for the spine, while decreasing for the PTV, showing the importance of adequate analysis of the entire structure. When the AND metric was used to further reduce the size of the analysis area, the spinal cord r-values decreased.

Based on this data, it appears that binary masks may have some utility for analyzing individual structures, especially if those structures occupy a small portion of the field. However, care should be taken to ensure that enough measurement points are included in the analysis to cover the entire structure.

Overall, falloff weighting was able to produce better r-values compared to binary mask weighting. For the PTV-95% metric, a 3%/3mm and 3cm falloff from the OR mask was optimal. For the Spine_Max metric, a 2%/2mm and 3cm falloff from the OR mask was optimal. This supports the use of a lower dose threshold to include data outside of the PTV in the gamma analysis.

For almost all masks and gamma criteria, the r-values improved when the structure dependent importance weighting was included in the gamma analysis. As slope increased, the structure metrics tended get better at first, however most reached a critical point after which an increase in slope led to a decrease in the r-values. The effect of increasing the power was less beneficial, in that r-values were optimized for a power of 1. Some did show improvement for a power of 2, but most r-values became smaller for powers of 3 and above.

For the spine, the PTV and OR masks performed similarly to the SPINE mask. The magnitudes of the r-values were similar across the masks, and the optimal power and slope constants were also similar. For the 2%/2mm criteria, the optimal slope and power values were 2 and 1, respectively. For the 3%/3mm criteria, the optimal slope and power values were 3 and 1, respectively.

For the PTV structure, the PTV and OR masks produced better metrics compared to the SPINE mask. The optimal slopes and powers were 2 and 1 for 2%/2mm; 3 and 1 for 3%/3mm. This matched the optimal values for the spine, suggesting that a single set of importance weighting should be used in conjunction with a large mask (ex. 10 percent threshold) to produce optimal r-values for various structures.

When the structures were used to modify the gamma analysis criteria, similar trends were observed to the structure dependent importance weighting. Like the importance weighting, utilizing a power scaling technique was beneficial up to a cubic-power, however higher powers did not show the same benefits. The structure dependent gamma criteria produced r-values that were stronger than any

traditional gamma analysis criteria (1%/1mm, 2%/2mm, 3%/3mm). As the structure dependent criteria ranged between 1%/1mm to 3%/3mm throughout the treatment field, strictness of the passing criteria was equal to or less than the 1%/1mm traditional global criteria. This suggests the improvement in r-values were not just from increasing the strictness of the gamma analysis criteria. Rather, preferentially weighting the gamma analysis using patient structures, either through importance weighting or gamma criteria weighting, can have a positive effect on the correlation between pass rates and dosimetric plan metrics.

Conclusion

Choosing appropriate gamma criteria and including structures in the gamma analysis were both able to improve the correlations between per-plan IMRT QA pass rates and deviations in dosimetric plans rates. However, the commonly used 3%/3mm/10% threshold performed favorably as well. Analysis techniques that produced many pass rates near to 100%, tended to have poorer correlations than those that were more evenly distributed. This may be a fundamental flaw in the current clinically practice, where IMRT QA tests are designed with high pass rates tolerances (ex. 95%). This study was limited given the scope of the types of IMRT plans studied (static-gantry angle head and neck) and the types of errors (MLC transmission and penumbra), however the various techniques that were used are applicable to other errors and static-gantry angle treatment types.

CHAPTER 6 SINGLE-ISOCENTER MULTI-TARGET IMRT CRANIAL SRS COMMISSIONING

Introduction

Elements Multiple Brain Mets SRS (MBMS) is a site-specific planning system for treating multiple cranial targets that was developed by Brainlab (Brainlab, Munich, Germany). Unlike conventional planning systems that are designed to treat a wide range of anatomical sites, MBMS creates single-isocenter multi-target (SIMT) linac based cranial stereotactic radiosurgery (SRS) plans, using non-coplanar dynamic conformal arcs. SIMT has the potential to create plans with similar organ at risk (OAR) sparing and target coverage, while reducing treatment times compared with multiple single-target plans.[165-168] The specificity of the MBMS allows for an optimization algorithm that can focus on important cranial SRS metrics. The optimizer can also overcome typical linac based cranial SRS planning shortfalls, like the bridging of dose between two targets.

One drawback of the specificity of the TPS being able to only produce one type of plans for a specific anatomical site, is that the commissioning physicist is unable to perform an AAPM Task Group 119 type test of the system to compare their commissioning results for various anatomical sites to other institutions.[96] Furthermore, MBMS may be commissioned at the start of an institution's linac-based cranial SRS implementation so there may not be any internal data for comparison. In this work, the MBMS commissioning experience on an Elekta Versa HD (Elekta AB, Stockholm, Sweden) will be presented which can be used for guidance as well as a baseline for comparison.

Materials and Methods

Generating Beam Model

Beam model measurements included: PDDs, profiles, scatter factors, collimator transmission, and dynamic leaf shift. Data collection followed Task Group 106 methodology.[169] All measurements were

made in Sun Nuclear's (Sun Nuclear Corporation, Melbourne, FL) 3D water tank with Sun Nuclear's 0.125cc chamber, EDGE detector, or PTW's (PTW-Freiburg, Freiburg, Germany) microDiamond detector. A SNC 0.125cc chamber was used as a reference chamber to normalize the data for fluctuations in linac output when scanning profiles and PDDs.

The water tank was set up to the central axis of the beam using a ray tracing procedure. For profile measurements, the tank was shifted 0.25cm (1/2 leaf width) in the jaw direction, so the detectors intersected a multi-leaf collimator (MLC) leaf tip instead of junction between two MLC leaves. For output measurements, a Daisy-Chain method was used to calibrate the microDiamond for small field measurements[170]. The SNC 0.125cc was used to measure output factors down to a 3.0cm field size, after which it was cross calibrated to the microDiamond chamber to measure output factors down to 1.0cm. microDiamond measurements were performed without corrections, which is examined in the discussion.

Beam data was collected for energies 6X, 6FFF, and 10FFF. The measured data was processed by Brainlab to calculate leaf shifts, tongue and groove sizes, source functions, and radial factors.

After beam model parameters were measured and calculated, machine models were created for each energy. Machine models require department specific parameters (machine name, coordinate convention, etc.) along with machine specific information such as dose rate and maximum gantry speed. The machine type parameters were collated from 3 sources: 1) Versa HD manuals, 2) Monaco manuals (provided by Elekta), and 3) settings in existing hospital planning systems (Pinnacle). Following the creation of the machine model, the energy specific beam models were created for the three energies. Prior to final saving of the model, the system performed a secondary check for the data to help protect against non-realistic values.

Validation

AAPM Task Group 53 was used to guide the treatment planning system (TPS) validation.[109] The data transfer from Elements to the record and verify system (Mosaiq) was tested using various test plans. Subsequent data transfer to the linac and on-board imagers was tested. Data fidelity was checked at each step of the transfer.

Initial validation of the MBMS version 1.5 beam model was done using the Beam Model Verification module, included in the Elements software, which allows the calculation of single fields on phantoms. Dose was calculated with a Pencil Beam Algorithm utilizing a 1mm grid size. A virtual water phantom with density 1.0g/cm^3, simulating a water tank, was generated in Matlab and imported into Elements. The point dose, output factors, depth dose, and profiles were calculated using the same geometry as the commissioning measurements and verified against measured data.

Following beam model verification, the validation of typical clinical deliveries was performed. Since Elements is a template-based software, various prescription and beam arrangement template protocols were generated to cover the range of expected clinical cases. Prescription protocols of 19Gy x 1fx, 8Gy x 3fx, and 6Gy x 5fx were created with various minimum target coverages of 95%, 97%, and 99% for a total of nine protocols. Beam templates for 2, 3, and 5 different couch angles were created. Two versions of each protocol were created: 1) all the couch angles on one side of the gantry, 2) couch angles on both sides with symmetrical arrangement. MBMS automatically mirrors one-sided protocols if the target is on the other side of the brain, therefore the generation of both left and right sided protocols was not needed.

To test the protocols, previously treated cranial SRS patients treated within the hospital system, were re-planned in MBMS. All initial plans were 1 fraction treatments with the same prescriptions ranging from 15Gy to 20Gy covering 95% of the target. Fourteen clinical targets were studied ranging from 0.27cc

to 7.32cc. Plans had between 2-5 couch angles and 1-5 targets. Each plan was recalculated for three energies: 6X, 6FFF, and 10FFF. While it was known that 10FFF would not be used for cranial treatments, the energy was commissioned in anticipation of different anatomical sites for use with Elements (ex. Spine). Regardless, it is recommended that at least two energies be commissioned simultaneously to allow cross-comparison between results, which can be helpful with troubleshooting any inconsistencies that arise during validation.

$$ICI = (TV \times PIV)/(TV_{PIV}{}^2) \quad (14)$$

$$GI = PIV_{half}/PIV \quad (15)$$

where, *ICI* = Paddick Inverse Conformity Index

GI = Gradient Index

TV = Target Volume

PIV = Prescription Isodose Volume

TV_{PIV} = Target Volume covered by Prescription Isodose Volume

PIV_{half} = 50% Prescription Isodose Volume

Plan quality was evaluated using Paddick inverse conformity index (ICI – Equation (14*)*), gradient index (GI – Equation (15)), and Brain V_{12Gy} (volume of normal brain getting dose of 12Gy or more) to get an understanding of the limits of the system.[171, 172] A subset of plans (volumes ranging from 0.89cc to 7.32cc) were exported to Mosaiq for dosimetric validation on the Versa HD. Dose validation was performed using a combination of Gafchromic film, microDiamond point dose measurements, and SRSMapcheck. All measurements were done using StereoPHAN with proper inserts. To set up the StereoPHAN in MBMS, multiple CTs were acquired will the different measurement inserts using a Philips Brilliance Big Bore CT scanner (Andover, MA) with 1mm slice thickness. The StereoPHAN was indexed to the CT couch while scanning with different inserts to prevent movement. This allowed for easy comparison of cross-modality measurements (ex. Gafchromic Film and SRSMapcheck) using the same DICOM

coordinates. The phantom was imported into MBMS and assigned a uniform density of 1.20g/cm^3 as specified by the StereoPHAN manual.

Initial dose validation of the phantom was performed by measuring simple square fields on the Versa HD at various gantry/couch angles. This confirmed the model within the TPS was correct and also verified the angular and field size dependencies of the various detectors matched manufacture's specifications.

Subsequent dose validation was performed for MBMS plans. When measuring single target plans, the StereoPHAN central axis was aligned to the in-room lasers, so that the dose cloud was positioned on the central axis of the detector. However, for multi-target plans, where target dose clouds are often located away from isocenter, the phantom was shifted for QA measurements to align the target dose clouds with the detector central axis. This corresponding shift was done in the Elements software by moving the beams isocenter position on the phantom. Equation 16 was used to determine the new measurement isocenter position (I_m), from the detector central axis (I_d), target position (I_t), and treatment isocenter (I_p). All positions were 3 x 1 matrices (x,y,z). The measurement and detector positions were DICOM coordinates on the phantom CT. The target and plan isocenter were DICOM coordinates on the patient planning CT.

$$I_m = I_d - R_y(\theta')\,(I_t - I_p) \quad \text{, where } \theta' = \theta_p - \theta_m \tag{16}$$

The rotation matrix was included for measurements that were performed at a different couch angle than planned. For example, some measurements were done at couch angle zero to minimize angular dependencies of the detectors. The 3 x 3 matrix is an elemental rotation matrix about the y-direction (anterior-posterior) where θ' is the difference between the planned ($\theta_{p)}$ and measurement (θ_m) couch angles.

To apply shifts during measurements, the phantom was first set up to the lasers and calculated shifts ($R_y(\theta')\ (I_t - I_p)$) were manually typed into the Elekta iGuide software. The iGuide software used the translational movements on the 6 Degree of Freedom Hexapod couch to apply the shifts. For shifts outside of the Hexapod range of motion, the iGuide software prompts the user to manually shift the 3-dimensional Elekta Precise table to get close to the intended position, before automatically performing final adjustments with Hexapod couch.

In addition to validating dose on MBMS patient plans, an End-to-End (E2E) test was performed using the StereoPHAN phantom. The E2E test incorporated all clinical steps from initial imaging, fusion, contouring, planning, data export to record and verify system, quality assurance of the treatment plan, positioning using image guidance, and treatment delivery. The MR target insert, consisting of three spherical cavities (two 10mm diameter and one 20mm diameter) filled with mineral oil, was imaged using MRI and CT scanners. The images were co-registered in MBMS and targets were contoured on the MR image set and compared with the CT data set to validate geometric accuracy. A 5-table angle 6FFF MBMS plan was created that delivered 18Gy in one fraction to each target. The plan was exported to Mosaiq for delivery and pre-treatment plan QA was performed. The in-room imaging system was used to align the StereoPHAN with the Gafchromic film insert. The treatment plan was delivered to a Gafchromic film plane that intersects all the targets. Point dose measurements were taken with microDiamond at the center of each target. Gafchromic film and microDiamond measurements were compared to dose calculated by MBMS plan.

Following the commissioning of MBMS version 1.5, an updated version of the software 2.0 was released. A new optimizer was tested for clinical use with the following major changes: 1) MLC margins can vary between -3mm to 3mm and change between arcs (previously a universal 1mm margin was used), 2) jaws can partially cover an MLC leaf (previously fixed to the leaf edge), 3) optimizer cost function focused on dose falloff as well as conformity (previously only conformity). The commissioning plans were

re-optimized with the new software and a student t-test was used to compare plan quality metrics for the two optimizations. In addition, a subset of the plans were delivered to an SRSMapcheck and microDiamond in a StereoPHAN on a Versa HD to verify dose.

Results

Beam Model – Scatter Factors

Comparisons between measured and calculated scatter factors measured at 100cm source-to-phantom distance and 10cm depth were performed (Figure *37*). Square fields were within 1% of Elements calculated values. The absolute measured scatter factors are shown in Table 12 for comparison.

Field Size (cm)	6X	6FFF	10FFF
1.0	0.677 (3)	0.696 (3)	0.680 (4)
2.0	0.806 (2)	0.830 (3)	0.843 (4)
3.0	0.847 (3)	0.872 (2)	0.894 (3)
4.0	0.879 (1)	0.901 (4)	0.923 (1)
6.0	0.928 (2)	0.945 (2)	0.958 (2)
8.0	0.970 (2)	0.977 (2)	0.982 (4)
10.0	1.000 (0)	1.000 (0)	1.000 (0)

*Table 12: Measured scatter factors at 100cm SSD and 10cm depth. Field size is nominal setting on the VersaHD. Bracketed numbers show the 2*sigma uncertainty in the last digit.*

The uncertainty in the measurements were calculated as two times the standard deviation of repeated measurements on separate days. It is important to note that scatter factors measurements were required without any leaves open behind the jaws. However, 1cm field size calculations could only be performed with an additional two leaves open behind each jaw that matched the width of the open leaves defining the field. Colloquially known as guard leaves, these will increase the dose for a 1cm field by approximately 4%. This discrepancy likely contributed to the small (<10mm) single-target modeling error that is discussed in the dose validation section.

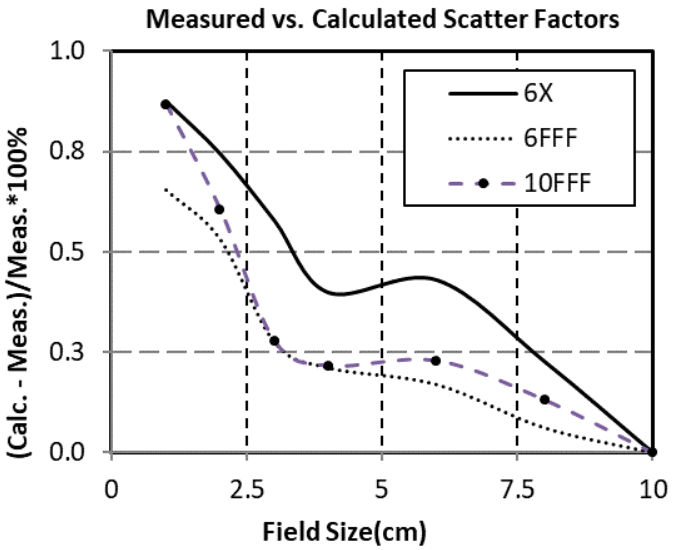

Figure 37: Comparison between commissioning and calculated scatter factors at 100cm source-to-phantom distance and 10cm depth. All scatter factors were normalized to unity for a 10cm x 10cm field.

Beam Model – PDDs & Profiles

The difference between the measured and calculated PDDs and profiles for select 6FFF square fields and depths were compared (Figure *38* and Figure *39*). The PDDs and Profiles were normalized to dmax and the central axis, respectively. A PTW-60019 microDiamond chamber was used for PDD scanning. Large field profiles, used in beam model generation, were scanned with the Sun Nuclear 0.125cc chamber. Subsequent profiles down to 1cm field size were scanned with both the microDiamond and EDGE detector for beam model validation. Measured PDDs were within 0.5% of calculated past dmax for all energies. Measured Profiles for all energies were within 0.5% of calculated for typical cranial off-axis treatment distances (<10cm).

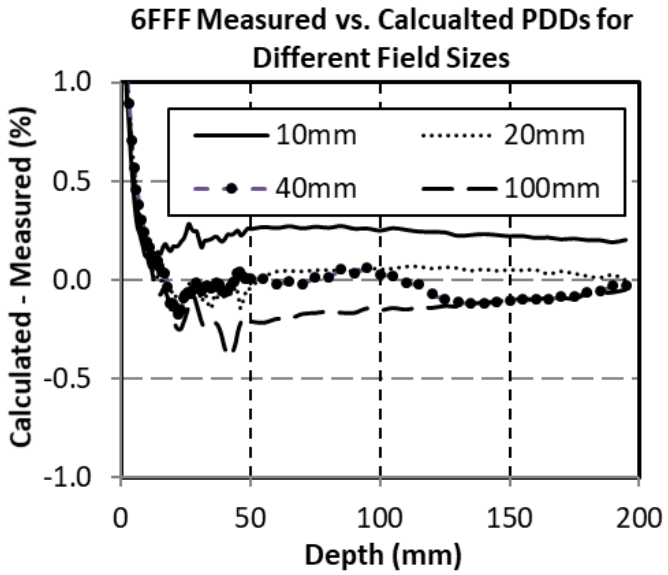

Figure 38: Comparison between commissioning and calculated 6FFF percent depth doses (PDDs) at 100cm source-to-phantom distance for selected field sizes.

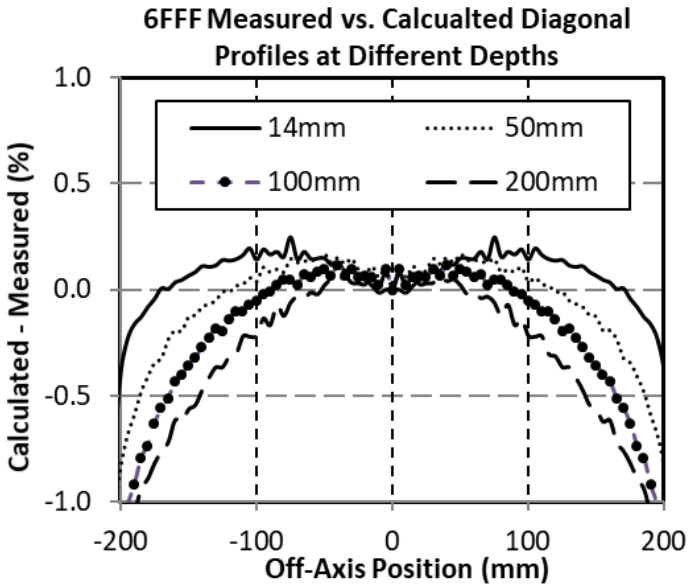

Figure 39: Comparison between commissioning and calculated 6FFF diagonal profiles at 100cm source-to-phantom distance for select depths.

Beam Model – Collimator Penumbra

The measured in-plane (jaw) penumbra was larger than the cross-plane (MLC) penumbra, which is similar to previous publications.[129] The difference between the measured and calculated penumbras is

shown in Figure *40*. All profiles were normalized to the central axis for comparison. The differences in the jaw direction were typically <2.0%, while the differences in the MLC direction were <10.0%. The penumbra differences were similar for different field sizes and depths. A single penumbra model is used for both the MLC and Jaws, which resulted in a larger difference in the MLC direction.

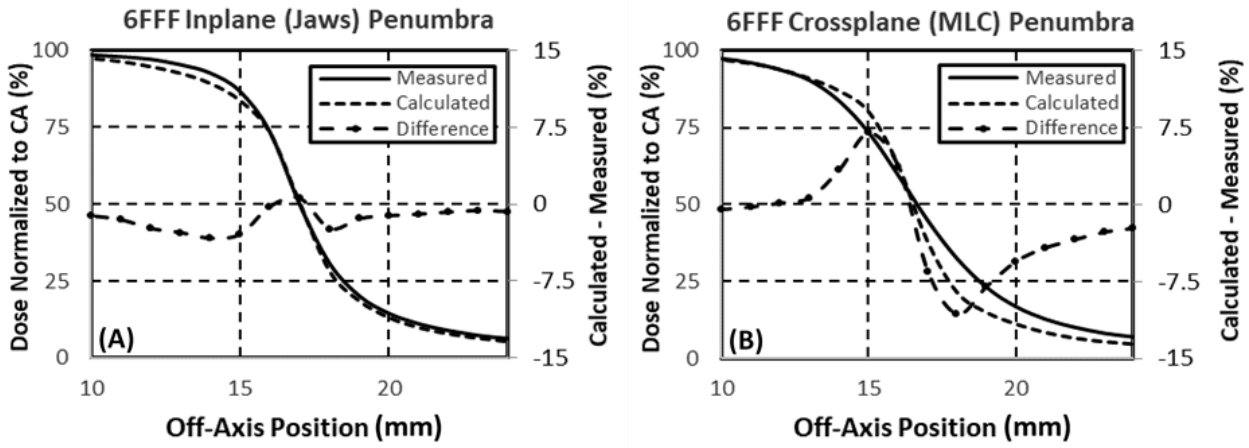

Figure 40: Difference between the measured and calculated 6FFF collimator penumbras at 100cm source-to-phantom distance, 10cm depth for a 3cm x 3cm field size. The discrepancy is smaller in the jaw direction (A) compared with the MLC direction (B).

Beam Model – MLC DLS and Transmission

The measured MLC transmissions and dynamic leaf shifts are shown in Table 13. The 10FFF transmission was slightly lower than 6X and 6FFF, however this is offset by the larger dynamic leaf shift causing increased transmission near the field edges. The transmission with the jaws closed (jaws and MLC combined) was zero percent for all energies.

	6X	6FFF	10FFF
Transmission	0.4%	0.4%	0.3%
Dynamic Leaf Shift	0.15	0.22	0.26

Table 13: Measured multi-leaf collimator (MLC) transmission and dynamic leaf shifts.

MBMS plan quality

The MBMS plans had GIs smaller than 5.0 and ICIs smaller than 1.5 for target diameters larger than 10mm. For targets smaller than 10mm, the GI increased above 5.0 for SIMT plans as shown in Figure *41*. This increase occurs at approximately two times the multi-leaf collimator (MLC) width of the Versa HD (5mm at isocenter) and may be different for other MLCs. Chea et al. found a similar increase in GIs above 5.0 for target smaller than 0.1cc, which corresponds to a diameter of approximately 0.6mm[173]. The lower cutoff may have been due to their use of Varian's HD-MLC, which has a width of 0.25mm at isocenter at the central axis. However, Liu et al. found this GI increase to occur at approximately 0.3cc (0.8mm diameter) for single-target VMAT plans that were generated for Varian's HD-MLC, which is close to what was observed in this study[174].

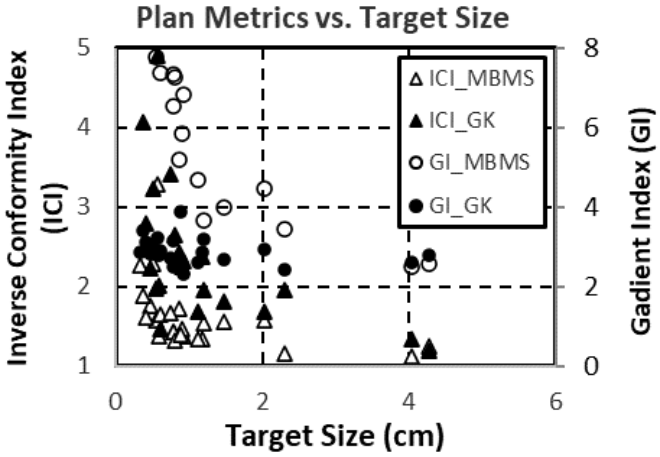

Figure 41: Dose metrics for single-isocenter multi-target plans of different target sizes created with MBMS compared with Gamma Knife (GK).

Due to the small size of the targets, an increase in GI corresponding to a larger 50% prescription isodose volume, has a smaller effect on V_{12Gy} compared with a larger targets. Therefore, a higher GI is often deemed clinically acceptable, when treating small targets which may add a small volume of V_{12Gy} with additional larger targets. Also when treated in isolation small relative amounts of V_{12Gy} may be clinically irrelevant depending in terms of risk of radionecrosis and focal neurological deficit.[175, 176] ICIs

tended to be worse for irregularly shaped targets, which matches previous work showing SIMT deliveries having better normal tissue sparing for spherically shaped targets.[177]

Compared to the Gamma Knife plans, the MBMS plans tended to have better ICIs and worse GIs. On average the MBMS V_{12Gy} was 0.998cc +/- 4.179cc lower than the Gamma Knife. However, the Gamma Knife plans often had lower V_{12Gy} values than the MBMS plans, which is reflected in the large standard deviation about the average.

MBMS Dose Validation

Measured MBMS microDiamond doses had a mean difference of 0.31% compared to MBMS calculated dose with a maximum difference of 2.84%. Average per-field pass rates measured with the SRSMapcheck in the StereoPHAN were 98.0% with a minimum of 95.5% using a 2%/1mm/10% threshold. E2E testing showed similar results, with a microDiamond measurements within 1.5% of planned, and Gafchromic film pass rates of 98.6% and 99.6% using a 10% threshold and 3%/1mm and 5%/1mm gamma criteria, respectively. Figure *42* shows the Gafchromic film results in the axial plane for the 3 target E2E plan. Most of the remaining failing points with the 5%/1mm criterion were due to the pin-holes in the Gafchromic film, which were used for registration.

When a plan was generated for only a single target, the microDiamond measured dose began to increase >3% for targets below 10mm, possibly due to larger effect of guard leaves in smaller targets. However, this dose discrepancy was not observed when the smaller target was included in a plan with other targets. Attempts were made to manually adjust beam model scatter factors to better model single target dose, however it was found that improvements in single-target dose modeling would lead to larger errors in multi-target plans. Due to the multi-target purpose of MBMS, the decision was made to prioritize multi-target dose modeling over single-target.

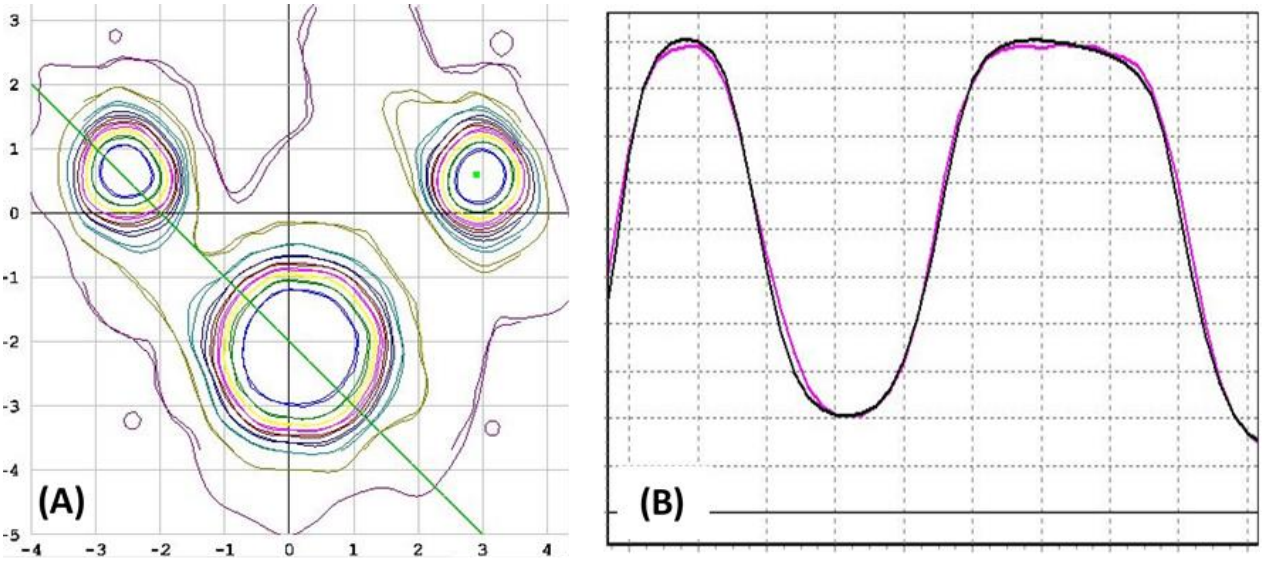

Figure 42: Axial film results of the end-to-end test. (A) Isosdose overlay between Elements-predicted and film-measured dose. (B) Line profile between two targets (green line in (A)).

MBMS Version 2.0

The new optimization algorithm in MBMS Version 2.0 reduced ICIs by 0.05+/-0.10 [$P < 0.01$] and GIs by 0.40+/-0.65 [$P < 0.01$], with no significant changes to the PTVmin [$P > 0.10$]. Whole brain V_{12Gy} was reduced by an average of 2.39cc [$P < 0.01$]. The resulting reduction in whole brain V_{12Gy} is visualized in Figure *43* where the new optimizer eliminates the 12Gy dose-bridging between the two targets. A similar improvement in plan metrics in MBMS v2.0 has been observed in previous publications[178]. Average SRSMapcheck pass rates were 98.7% [97.0% - 99.8%] using relative gamma analysis (2%/1mm/10% threshold). Measured microDiamond dose was within 1.40% of calculated for all targets.

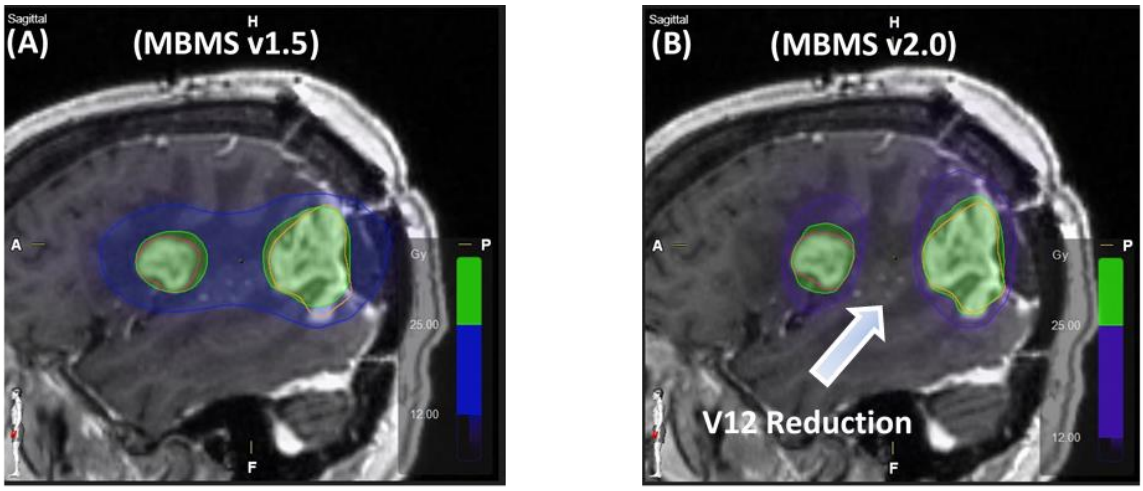

Figure 43: Plan comparisons between: (A) MBMS v1.5 and (B) MBMS v2.0. The updated algorithm removes the 12Gy dose-bridging.

Discussion

Due to the small field sizes used in cranial SIMT deliveries, small misalignments of the water tank may lead to sharper falloff in PDDs and lower scatter factors. For PDD measurements, the tank should be aligned to the beam axis. This will require that the water tank deviates from true level as gantry sag on the VersaHD causes the beam axis to point slightly towards the gun direction. The alignment of the beam-axis can be verified by scanning profiles at multiple depths and ensuring the central axis of the profiles remains unchanged. Furthermore, the beam profiles should be scanned immediately prior to small field scatter factor measurements to position the detector at the local maxima within the field.

IAEA TRS-483 provides an exhaustive list of small field correction factors for various chambers.[179] These can be used to correct small field scatter factor measurements, particularly when comparing results between detectors. If correction factors are used for commissioning measurements, they should also be used for validation measurements. Published correction factors are typically reported for reference conditions on the central axis, while MBMS validation measurements will likely be off-axis. The correction factor for a given field size under reference conditions may differ from validation measurement, due to

changes in small field phenomena (source blocking, volume averaging, angular dependence, etc.). Therefore, it is recommended to validate small field dosimetric accuracy with multiple detectors.

In this work, small field correction factors were not applied to the measurements. Based on TRS-483, the microDiamond will over-respond by approximately 1.5% for a 1.0 cm field size. Additional publications have suggested this over-response may be up to 3.4% for a 6FFF beam on the VersaHD with a 1.0 cm field size[180]. This over-response will lead to an increase in the measured small field scatter factors and thereby a reduction in the delivered dose. This matches the measured E2E film results which were found to be 1.5% lower than the predicted TPS dose for the 1.0cm target (Figure *42*). Given the expected clinical prescriptions for the small targets, this lower dose was deemed to still be ablative to the target, while the clinical organs-at-risk dose would be within tolerance.

TPS validation of water tank measurements was important for discovering fundamental limitations of calculation model. Specifically in Elements, a discrepancy was found in how the Versa HD MLC penumbra is modeled. It was found that error in the MLC model could lead to reduced pass rates for single field measurements at couch zero with a small collimator rotation. In these instances, the modeling error could have coherent summation leading to failing measurements along the edges of the targets. However, when the cumulative target dose from all fields in the MBMS plan was measured with couch rotations applied, the MLC modeling error had little effect on the overall dose distribution.

One of the unique challenges of SIMT commissioning was positioning the detector at the center of an off-axis target. This was accomplished by manually applying shifts with the Hexapod couch, which has been shown to have sub-millimeter accuracy.[181] An initial hurdle to this technique was determining how the Hexapod coordinate system related to real-word and TPS coordinates. It is recommended that coordinate correlations be determined ahead of QA measurements by either: 1) an investigation of documentation and system settings, or 2) guess-and-check method where shifts are applied and the

resulting real-world shifts are recorded. During commissioning the guess-and-check method was used to determine the coordinate relationships between: 1) treatment planning system, 2) six degree of freedom couch, 3) in-room imaging systems, 4) QA analysis software.

The arclength error produced by a rotational error will increase as targets get farther from the central axis. For small angles, the linear error will equal the radius times the angle in radians. AAPM Task Group 142 recommends a 1° collimator tolerance.[120] A 1° collimator error would create a 0.87mm linear error for a target 5cm away from the central axis. To reduce this error, a stricter 0.5° collimator tolerance was adopted, which was found to be consistently achievable on monthly QA. Furthermore, TG-142 requires a 0.5° couch tolerance for SRS/SBRT, however the clinical display only shows integers. This was overcome by enabling the "PSS" page in service mode, which reports angles in 0.1° increments. Studies show that target coverage degrades substantially when rotational errors approach 2°.[182] Therefore, minimization of both mechanical and patient setup errors is critical. This can be partially accomplished by real time image guidance at each couch angle and positioning the patient with a six degree-of-freedom robotic couch[183].

When creating beam and prescription protocols, it was best to create one prescription and beam protocol and fully test the planning and delivery. Once fully tested, the protocols could then be copied and modified as needed. This would help prevent unnecessary time fixing issues that may propagate through all the protocols if they are generated prior to testing.

The two main advantages of SIMT are efficiency in planning and delivery. For a multi-target cranial case without SIMT, each target would have a separate isocenter with its own set of non-coplanar arcs. The person designing the treatment would have to manually optimize the arc, gantry, and couch angles appropriately so that the treatment of one target does not overlap with another target. The issue of dose overlap in multi-isocenter plans is twofold: 1) overlapping dose will increase the dose to other targets,

which may cause overdosing and increase the GI and ICI metrics, 2) dose overlap in the normal brain tissue, particularly in the high dose region, will increase the brain V12 which may lead to normal tissue complications

For a two-target treatment, it is typically easy to prevent cross-target dose overlap by viewing each arc in the beams-eye-view and adjusting the couch and gantry angles to avoid projecting dose through the other target. However, this manual optimization quickly becomes more complicated when the number of targets increases. This increased complication typically results in increased variation amongst different planners, as often more experienced planners are better able to handle this manual optimization. Regardless of the abilities of the planner, this manual optimization is tedious. Furthermore, some overlapping of dose between targets is inevitable due to scatter within the patient. Therefore, optimizing individual target doses then combining them may not produce the optimal plan for each target when the summated dose is considered.

The Elements MBMS optimization solves both problems of angular optimization and dose overlapping by optimization all targets simultaneously. What may have taken multiple hours, or even days, to plan can now be accomplished in less than 10 minutes. Furthermore, the time on the treatment machine can be dramatically reduced due to the need to only setup the patient once for a single isocenter. A typical clinic, treating with a Versa HD, will take 30-45 minutes per isocenter for a non-coplanar cranial SRS case. A 5-target treatment would be 2.5 – 3.75 hours for a multi-isocenter treatment versus 30-45 minutes for a SIMT delivery. This is of particular importance to the patient who is immobilized in a rigid, and often uncomfortable, aquaplast mask to prevent intra-fraction motion.

While SIMT has the potential to reduce delivery and optimization times, it may not be suitable for all target sizes and locations. As shown in Figure *41*, the GI begins to increase as the target size becomes smaller than approximately 10mm. With the improvement in MBMS v2.0, the threshold for GI degradation

was reduced to target sizes below 8mm. For target sizes less than this threshold, the increased dose to the normal tissues, corresponding to an increase in GI, may be deemed clinically unacceptable. In these cases, there is the option to treat with stereotactic cones that are affixed to the linac gantry head. The stereotactic cones can produce beam sizes down to 5mm in size with sharper penumbras compared to MLCs, thereby improving the normal tissue sparing. Furthermore, if a Gamma Knife treatment unit, which is a dedicated cranial SRS treatment machine, is available within the hospital system, then the small lesions can be treated on that machine as well.

For these small lesions, it appears from Figure *41* that the MBMS plans have better ICIs than the Gamma Knife, which may offset the benefits of the smaller GK GIs. However, the larger ICIs may be due to the forward-based planning technique used to generate the Gamma Knife plans. The Gamma Knife plans are typically created by manually designing a treatment such that the prescription isodose line surrounds the contrast enhanced area of the MRI, which denotes the tumor location. The prescription isodose line will cover the enhancement with some margin, typically 0.5-1.0mm. The target contour is often drawn after planning is completed and is typically a contour of the enhanced area of the MRI. Therefore, the prescription isodose is slightly larger than the target contour, which causes the increase in the ICI.

The MBMS plans, however, are planned inversely, with the target contour drawn first, followed by planning to have the prescription isodose volume cover the target contour as closely as possible. This leads to optimal ICIs for the MBMS plans. This effect is amplified at smaller targets sizes, where the 0.5-1.0mm Gamma Knife margin will increase the prescription isodose size by a larger percentage, compared with the larger targets. This difference in planning techniques, may also lead to slightly higher whole brain V_{12Gy} that were observed in the MBMS plans. Due to the difference in planning techniques used in this study, the MBMS plans were not compared directly to the GK plans. Rather, the Gamma Knife plans were

used as a basis for MBMS investigation, and the MBMS dose metrics (GI, ICI, and V12Gy) were used to determine plan acceptability.

In addition to treating small targets with cones, there are instances where larger targets that are next to critical structures, may not be suitable for MBMS optimized SIMT deliveries. The MBMS algorithm creates plans with dynamic conformal arcs, where the MLC aperture conforms to the outside of the target. This typically provides sufficient dose sculpting around most cranial targets. However, if the target is particularly irregular or directly abutting a critical structure, additional MLC modulation for dose sculpting may be required. For these targets, it may be beneficial to create separate VMAT plans, that allow for full MLC modulation to improve the conformality of the dose to the irregular target or increase the dose sparing of the critical structure.

Furthermore, a second VMAT plan may be warranted for single target that is located away from a cluster of other targets. If the distal target was included in the MBMS plan, the isocenter of the plan would move away from the primary cluster of targets to treat the distal target. This would amplify the effect of rotational errors on the treatments. Introducing a second plan will help to keep the SIMT isocenter close to the targets, thereby reducing errors from rotational uncertainties. Alternatively, an additional margin could be added to the target contour to account for the rotational uncertainties. In addition, if multiple targets exist throughout all areas of the brain, they could be separated into different clusters based on location, and multiple SIMT plans could be used for treatment.

Due to the multiple treatment options for a cranial SRS patient, scheduling issues can arise because the length of time required on the treatment machine may not be known until the plans are finalized. This can often occur less than 24 hours prior to treatment. A single cranial SRS patient can take anywhere between 30 minutes and 4 hours to treat, depending on the number and complexity of the

plans. This can be logistically challenging to schedule on a clinical treatment machine that will likely be treating other patients.

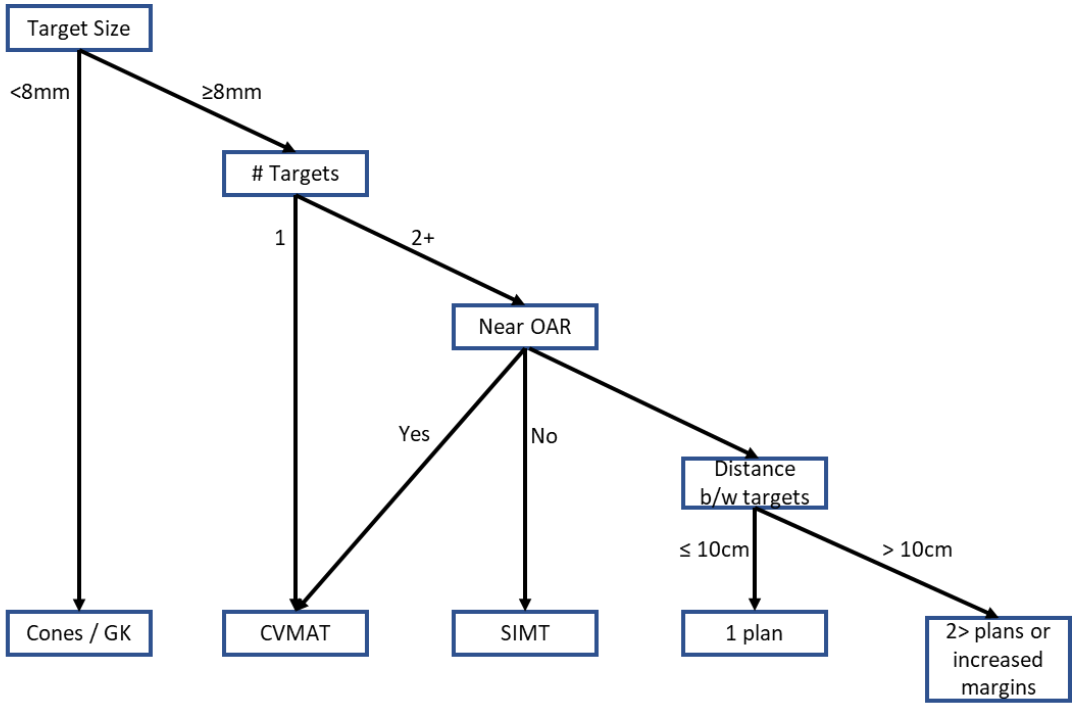

Figure 44: Decision tree for treating cranial SRS targets with a combination of single-isocenter multi-target (SIMT), volumetric arc (VMAT), and stereotactic cones or Gamma Knife (GK) treatments.

Therefore, it is helpful to the clinical workflow to try and predict which modalities will be used for treatment, prior to the patient receiving the therapeutic CT for planning. This can be done from looking at their diagnostic brain MR images to determine the expected number, location, and size of the targets. The target information can then be used to predict their expected course of treatment. A decision tree for this process is shown in Figure *44*. This decision tree does not contain mandatory rules for plan selection, rather it should be used as a guideline.

Conclusion

The commissioning of the MBMS TPS system introduces unique challenges for physicists due in part to the small fields, off-axis non-coplanar beam arrangements, and high-dose hypofractionated

prescriptions. Advanced knowledge of these challenges along with the expected limitations of the MBMS beam models can add familiarity to the commissioning process. Added familiarity will hopefully lead to faster and more consistent MBMS commissioning across institutions.

CHAPTER 7 CONCLUSION

The motivation for this work was to reduce the uncertainties in various subcomponents of the IMRT commissioning-to-treatment paradigm with the overall goal of improving the accuracy of IMRT deliveries. Five sub-components were selected for investigation that included:

1) Radiation-imaging coincidence optimization on a Versa HD.

2) Analyzing confidence limits used in AAPM task group no. 119.

3) Investigating ion-recombination effects in PTW's 1000 SRS.

4) The inclusion of patient structures in IMRT QA calculations.

5) IMRT single-isocenter multi-target cranial SRS commissioning.

Each sub-component affected only a fraction of modern IMRT deliveries, highlighting the complexity and diversity of the treatments themselves. Although, unavoidably limited within the entire scope of IMRT deliveries, the hope is that this research in the various sub-components, will enhance the ability to treat within the therapeutic window by reducing the uncertainties in the delivered dose.

One of the most stressful and important tasks that a medical physicist will perform is that of the initial commissioning of a treatment machine. The rarity of the task (a typical linac has a lifespan of 10+ years), coupled with the long-lasting effects that a mistake during commissioning will have on the lifetime of the machine, makes this a potential major source of error in the clinic. In addition, commissioning of a linac is often performed on a strict timeline that can be further compressed when upstream delays in linac installation compress the commissioning schedule against a hard-set go-live date. Therefore, the work on radiation-imaging coincidence optimization during the commissioning of a Versa HD has major utility for the clinical physicist.

The procedure that was developed provides step-by-step instructions on the optimizing the radiation-imaging coincidence during the commissioning process. It also provides expected achievable tolerances for the various sub-tasks involved in the procedure. This gives physicists clear direction of what to do when calibrating the Versa HD and at what point to stop fine-tuning as additional effort would lead to rapidly diminishing returns. This ensures that the machine will be calibrated with a high degree of accuracy, without requiring an unrealistic amount of time. Time conservation during commissioning is important as it allows the clinical physicist to focus their commissioning efforts in other areas. Ultimately this procedure will not only reduce the uncertainties in the radiation-imaging coincidence calibration, but it will also allow the physicist more time to reduce uncertainties in other areas as well.

The work on analyzing confidence limits used in TG-119 was able to shed light on the accuracy of the simplified statistical assumption used to determine the confidence limits in the report. Due to general application of the report for commissioning a wide range of treatment planning systems, any major uncertainty in the analysis methodology used in the report, could have wide ranging implications for clinical IMRT deliveries throughout Radiation Oncology. To validate the simplified statistical analysis used in the report, a more advanced statistical analysis was used to model the data within the results. Comparing the results between the complex and simple statistical analysis, it was found that the simplified analysis was sufficiently accurate for the expected range of clinical data that would be used in the report. This gave confidence that the simplified analysis of the TG-119 data could be performed, without the added uncertainty of making a mistake while performing a more complex mathematical analysis.

Throughout the different stages of the IMRT commissioning-to-treatment process, physicists rely on various measuring devices to query the radiation produced by the treatment machine. The development of new treatment technologies will always be paralleled with new measuring devices to quantify their accuracy. These devices typically display some results in an easy-to-digest format, however the displayed results do not typically include an uncertainty analysis. Therefore, it is of utmost importance

for physicists to understand the uncertainties of the measuring devices, prior to use, and work to reduce those uncertainties whenever possible.

PTW's 1000 SRS measuring device employed a unique solution to improve the signal-to-noise ratio in their detector arrays by using liquid filled detectors to improve the signal compared with traditional air-filled detector arrays. However, the liquid filled arrays have an inherent uncertainty due to the increased loss of signal due to ion-recombination during the measurement. The effect of ion-recombination is dependent on the strength and frequency of the radiation pulses exposed to the 1000 SRS, both of which may change during an IMRT delivery. Therefore, the uncertainty in the measurement is not static, but will change throughout the delivery, making it difficult to quantify for an individual measurement result.

The investigation of the 1000 SRS found that the uncertainty in the measurement due to ion-recombination could be dramatically reduced by appropriately calibrating the device on a per-plan basis prior to use. The specific reference condition needed for the calibration, average dose rate, could be easily extracted from the treatment plan and used for calibration. This simple calibration method gives the physicist the ability to quickly reduce the uncertainties in their 1000 SRS measurements due to ion-recombination, thereby reducing the uncertainty when using the device in the commissioning and patient-specific IMRT QA process.

Patient-specific IMRT QA has the difficult task of querying the many different uncertainties in an IMRT delivery, using a single measurement to determine whether the delivery is sufficiently accurate for clinical use. Like most QA measurements, they are performed in a simplified geometry and use simplified analysis technique to reduce the uncertainties in the QA itself. These simplified scenarios are typically void of any patient-specific information that may be beneficial in determining whether a given QA result represents a clinically acceptable treatment plan.

The research to include structures in the IMRT QA calculations was an attempt to incorporate patient-specific information into IMRT QA analysis. While the research was interesting, it became clear that large amounts of data would be needed to draw a statistically significant conclusion of whether including these structures would improve the correlation between IMRT QA results and the dosimetric acceptability of the plan. Furthermore, the research focused on static-gantry deliveries that are decreasing in popularity and being replaced by the more efficient moving-gantry volumetric arc therapy. Finally, the way in which IMRT QA measurements are performed and analyzed has changed considerably, making the initial research mostly obsolete. While the work may not have far reaching clinical importance, the investigation itself highlighted many of the potential uncertainties in the IMRT QA and treatment paradigm, particularly with the standard DICOM format used to store digital medical data, including that which is used for IMRT deliveries.

Perhaps the greatest test of IMRT delivery accuracy is that of SRS. A typical fractionated IMRT delivery benefits from the gaussian-smoothing effect, where multiple treatment deliveries occur with some uncertainty around a mean value, and it is expected that they will average to something close to the mean. Conversely, SRS has no such benefit of averaging, and any uncertainty in the single treatment fraction will have direct impact on whether the patient's treatment falls within the therapeutic window. Furthermore, single-isocenter multi-target (SIMT) cranial SRS has its own unique challenges that are not present in typical IMRT treatment. In a typical IMRT treatment, a single unified target contour is treated with the planned isocenter placed close to the centroid of the target. However, the multi-target nature of SIMT deliveries necessitates that the isocenter is placed outside of at least one of the targets.

The inherent lack of gaussian-smoothing and the irregular placement of isocenter outside the target amplified the importance of the research on commissioning Brainlab's SIMT cranial-SRS TPS for the Versa HD. The research presented in this chapter, outlines the work needed to commission, validate, and ultimately treat with this modality. In addition, it highlights some of the unique obstacles and solutions in

SIMT commissioning. The hope is that the work presented can be used by future clinics during commissioning, thereby reducing their commissioning uncertainties.

Although this research covered five different topics in various areas on IMRT, there were re-occurring common themes. Throughout the research, data was transferred between the various systems using the DICOM format. On DICOM import, most systems would convert the data into their own internal format for ease of use, speed, and efficiency. So too did the custom built Matlab code convert the DICOM data into usable DICOM data types. As new or upgraded systems emerge, the system-specific file types are expected to evolve to suit the needs of the systems.

However, given the historical inertia of the DICOM format, one could expect it to remain relatively the same, acting as the common language between the various systems. Although the DICOM format can often be used to transport data between systems, there is no guarantee that when the data is transferred, the information will be well-preserved. Throughout this research it was found that data transfer could lead to missing information, unreal information (ex. negative dose), and potentially worst of all, slightly incorrect information (ex. 1.40Gy rounded to 1.00Gy). Therefore, it is crucial to know how each system handles the import and export of DICOM data to detect potential errors and uncertainties that may exist in the IMRT process due to this data transfer.

This understanding of data transfer should be built into the commissioning process of any new equipment or technology. One could be tempted to assume that a clinically produced technology would perform with an exceptionally high accuracy all the time. In reality, most new technologies will have limitations, approximations, and possibly anomalies that make them behave with inherent uncertainties. Whether it is the ion-recombination effect of the 1000 SRS, the residual radiation-imaging isocentricity drift of the Versa HD, or the modeling error in the Brainlab Elements TPS, any new technology should be well vetted and independently investigated by the medical physics community. It is critical that both

positive and negative experiences are shared, to build confidence in the accuracy of treatment and prevent the propagation of errors.

While highlighting uncertainties in different systems is useful, it is important to remember that is easier to find instances where a system fails compared to showing that it works for a wide variety of cases. As was the case with the gamma index, where previous publications showed that gamma index pass rates did not correlate with patient specific plan metrics for head and neck plans. Their experiment was repeated to replicate, and improve on, their intriguing results, however in contrast to their findings a good correlation between gamma index pass rates and patient specific plan metrics was found for a standard clinical analysis criterion. However, this did not vindicate the pass rate as it only showed a good correlation for a small subset of the clinical IMRT setups for which the gamma index would be applied. To prove a universally strong correlation would have required much more data that covered different types of IMRT deliveries to different body sites.

What these seemingly conflicting results does show is that no single detector or analysis technique is perfect, and they all have their areas in which they perform better. Then the issue arises as to how a clinical physicist can be sure that a measurement is accurate. This is of particular importance during commissioning when uncertainties in measurements will propagate through the lifetime of the machine. The solution follows the technique that was best seen in the SIMT research when multiple detectors were used to measure the same field. Leveraging the utility of multiple redundant technologies, whenever possible, will help prevent the technology-specific uncertainties from effecting clinical IMRT deliveries.

Using multiple technologies for IMRT measurements may reduce uncertainties, however it requires additional physics effort and possibly equipment costs. Therefore, it is useful to know when it would be most prudent to employ additional effort to reduce uncertainties. This leads to the common

theme of standardization. Standardization is typically approached when enough different groups have performed the same task that they can now combine their cumulative experiences to generate best practices for that task. This highlights the importance of publishing commissioning experience like what was done with the radiation-imaging coincidence adjustment and SIMT commissioning work on the Versa HD. Publication of this work to an external audience also allows for global peer review that can often lead to suggestions that improve the publishers practice as well.

The peer review of a department clinical practices is possibly the best tool for reducing uncertainties in IMRT deliveries. It leverages the power of the community of medical physicists to tackle the implementation of the ever-expanding list of software, technologies, and treatment techniques used for IMRT. As IMRT deliveries continue to develop, physicists should continue to research and evaluate the new deliveries and the technologies that support them, to reduce IMRT delivery uncertainties and provide accurate, high quality care for radiotherapy patients.

APPENDIX A COMPUTER CODING IN MEDICAL PHYSICS

Introduction

The use of computer coding was integral throughout much of this work. The primary coding language used was Matlab, however there are many coding applications and languages that are used within Medical Physics. The one common element, which connects these languages together, is the standard format used to store digital medical information known as the Digital Imaging and Communications in Medicine or DICOM format. The DICOM format was created through a joint venture between the American College of Radiology and the Natural Electrical Manufacturers Association in the mid-1980s. The goal was to create a standard template for storing various types of medical information, so that this information could be easily passed between systems. There are multiple types of DICOM files, which outline the storage of image information (computed tomography scans, magnetic resonance images, radiographs, etc.), patient structure information that is drawn in the planning system, dose files, as well as radiotherapy plan information. This appendix will outline the general structure of the DICOM format, then it will focus on the specific DICOM files that were used in this research, and finally it will go over the methodology for some of the computer code that was developed throughout this work.

DICOM files are structured similar to a book, with a title page, chapters, and sub-chapters that contain the relevant information. The title page consists of a preamble and a header, which denotes the type of the DICOM file and contains the relevant patient information for the file. The chapters and sub-chapters within the files contain what is known as the DICOM Data Elements. Each of the DICOM Data Elements are labelled with a specific tag, followed by the length of the element, and finally followed by the data within the Element. Depending on the type of the DICOM file, it may also contain a value representation or VR in between the tag and element length, which denotes the data type of the element. To find data within the DICOM file, software will look for the specific tag, which consists of a pair of 16-bit

unsigned integers for a total length of 32-bits. The tags are commonly written as (HHHH,hhhh) where each H and h is a 4-bit hexadecimal number. For example, the tag for gantry angles is (300A,011E). When trying to find gantry angle for a specific control point, the software will look for the (300A,011E) tag, read the VR if it exists, check the length of the DICOM Data Element which represents the gantry angle, and then read the data. As each plan will contain multiple control points, the (300A,011E) will appear multiple times within the file for each control point that is nested within the radiation beams. To summarize, when writing code to look through a DICOM file, the element lengths should be used to skip through the file until the desired tag is located, the VR should be checked (if it exists), after which the length of the element should be checked and then the data should be extracted.

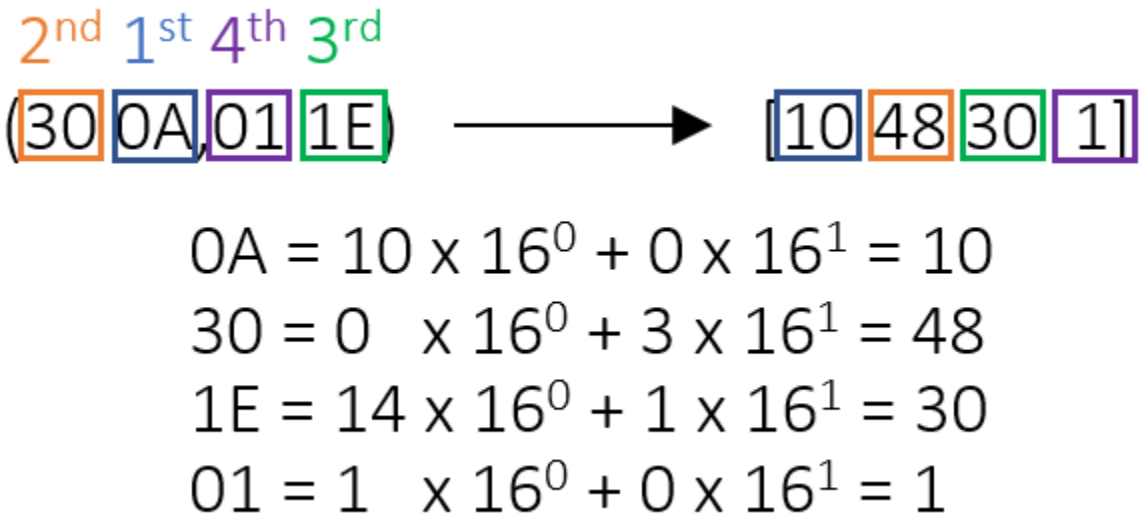

Figure 45: Converting DICOM Data Element tags from hexadecimal to 8-bit.

During the initial stages of the research, the version of Matlab that was used did not have a specific function to automatically look through the DICOM files, so it was necessary to write code to open the files and extract the relevant information. The custom code started by opening the file with a hexadecimal to 8-bit converter. Converting the file to 8-bit from hexadecimal meant the previous tags which were represented by a pair of 16-bit unsigned integers, were now represented by four 8-bit

unsigned integers. The conversion for the hexadecimal gantry angle tag of (300A,011E) to the 8-bit [10 48 30 1] is show in Figure 45.

After opening the DICOM file in 8-bit format, the code would skip the preamble and header and go directly to the DICOM Data Elements. The first tag was checked to see if it contained information that was relevant to the research. If it did not, the code would read the length of Data Element and skip ahead by that many bits. If it contained relevant information, then the data would be captured. Table 14 is a list of relevant DIOCM Data Elements tags that were used in this research. It is important to note that this Matlab code would be greatly simplified if it were done today using the dicomread.m function. The dicomread.m is a built-in Matlab function that opens a DICOM file and sorts all DICOM data in an easy-to-manipulate array. This would drastically reduce the amount of code necessary to perform the work.

Tag (hexadecimal)	Tag (8-bit)	Name	DICOM Filetype
(300A,011E)	[10 48 30 1]	Gantry Angle	Rt Plan
(300A,00C2)	[10 48 194 0]	Beam Name	Rt Plan
(300A,0120)	[10 48 32 1]	Beam Limiting Device Angle	Rt Plan
(300A,0122)	[10 48 34 1]	Patient Support Angle	Rt Plan
(3008,00A0)	[8 48 160 0]	Beam Limiting Device Leaf Pairs Sequence	Rt Plan
(3008,0078)	[8 48 120 0]	Start Meterset	Rt Plan
(3008,007A)	[8 48 122 0]	End Meterset	Rt Plan
(3008,0040)	[8 48 64 0]	Control Point Delivery Sequence	Rt Plan
(300A,00C0)	[10 48 192 0]	Beam Number	Rt Plan
(300A,011C)	[10 48 28 1]	Leaf/Jaw Positions	Rt Plan
(300A,0110)	[10 48 16 1]	Number Of Control Points	Rt Plan
(300A,010E)	[10 48 14 1]	Final Cumulative Meterset Weight Attribute	Rt Plan
(3006,0022)	[6 48 34 0]	ROI Number	RT Structure
(3006,0026)	[6 48 38 0]	ROI Name	RT Structure
(3006,0050)	[6 48 80 0]	Contour Data	RT Structure
(3006,0084)	[6 48 132 0]	Referenced ROI Number	RT Structure
(0020,0032)	[32 0 50 0]	Image Position	Rt Dose
(3004,000E)	[4 48 14 0]	Dose Grid Scaling	Rt Dose
(7FE0,0010)	[224 127 16 0]	Pixel Data	Rt Dose

Table 14: List of relevant DICOM Data Element tags in both hexadecimal and 8-bit formats, along with names and DICOM file types in which they are located.

Although Matlab code was used throughout most of the presented research, the gamma index work required the most amount of code. Furthermore, the code required the most amount of creative solutions, as it dealt will large amounts of data that would often overwhelm the memory of computers that were executing the code. Therefore, the following paragraphs will focus on the structure and obstacles of the Gamma Index code, while an overview of the code used in the other research is provided in their individual chapters.

As described in Chapter 5, the goal of the gamma index research was to include patient-specific anatomical structures in plan-specific gamma index calculations. To approach the coding for this research it was broken into three parts:

1) Structure data extraction from the DICOM files and projecting the structures from a beams-eye-view onto the dose plan used for the gamma index calculation.
2) Performing a gamma index calculation
3) Perform a correlation analysis between the passing rates of the gamma calculations and the patient specific plan deviation metrics.

This appendix will focus on the extraction of the structure data as it was unique to this research. To begin the extraction of the structure data from the DICOM files, the file was opened and converted to 8-bits from hexadecimal. The code searched the file to find the number of contours, the names of the contours, and the contour data itself. The code would then prompt the user to select which contours should be extracted for analysis. In the context of this research, the two contours that were to be included in the gamma index calculation were the PTV and spinal cord. However, due to the lack of standardization in naming conventions, the various plans could have different names for the same structure. For example, spinal cord could be named: spinal cord, cord, spinalcord, or spine. Therefore, it was necessary to have

human input to the otherwise automated code to distinguish the structures from the different contour names.

Once the contour numbers, corresponding to the spinal cord and PTV, were manually selected, the code extracted the contour data for those structures. In the DICOM format, the contour data is represented as a set of 3-Dimensional coordinates that delineate the outside borders of the contours. The coordinates are grouped by axial planes of the image set. Therefore, each set of contour points describe the vertices of a shape on a given axial plane. By combining the 2D-shape across all the axial slices of the image, a 3-dimensional shape is formed.

The 3-Dimensional coordinates in DICOM structure files are given relative to the 3-Dimensional coordinate of the upper left-hand corner of the associated image. While this coordinate convention is practical for DICOM files, for this research it was more beneficial to describe the contours in relation to the central axis of the plan, which corresponds to isocenter in the treatment vault. Ultimately the goal was to create beams-eye-view projections of the contours, which are centered about isocenter. Translating the coordinates system so that the central axis of the plan was the origin of the coordinate system, allowed the easy application of mathematical rotations which describe the beams-eye-view rotations around isocenter. To perform this translation, the DICOM isocenter location for each plan was subtracted from the contour coordinates, thereby centering the coordinate system at the central axis of the plan.

After performing the coordinate shift, the length of the spine contour was reduced to only occupy the same axial slices as the PTV. This was done to increase the speed of the code and reduce the memory burden of calculations, particularly when it came to rotating the structures. By reducing the length of the spine contour to only occupy the same axial slices as the PTV, the matrix size needed for the rotation was reduced. The power of Matlab as a programming software is in its ability to manipulate matrices and as

such, matrices were leveraged throughout the code in this research. When performing rotations with matrices it is necessary to allocate enough space in the rotated matrix to make sure the object that is being rotated does not get “lost” outside of a matrix. The size of the matrix necessary to prevent this loss is equal to the Euclidian distance between the farthest contour point and the center-point of rotation (central axis of the beam at isocenter). For the head and neck plans used in this study, the spine was typically contoured all the way to the inferior border of the CT, well outside the treatment fields that would ultimately be used in the gamma index calculation. Therefore, reducing the length of this contour would have no effect on the calculation, while aiding in memory conservation and calculation time efficiency.

With the structure data extracted from the DICOM Rt Structure file, the next step in the code was to extract the gantry and couch angles for each beam and used them to create rotation matrices to align the contours in the beams-eye-view projections of the fields. The IMRT QA that was being investigated in this study is typically performed at gantry and couch angles of zero degrees. Therefore, rotations were needed to transform the structure coordinates from the beams-eye-view projection to the zero-angle setup for IMRT QA. In terms of cartesian coordinates, this would align the beams-eye-view of the contours along the z-axis as shown in Figure 46.

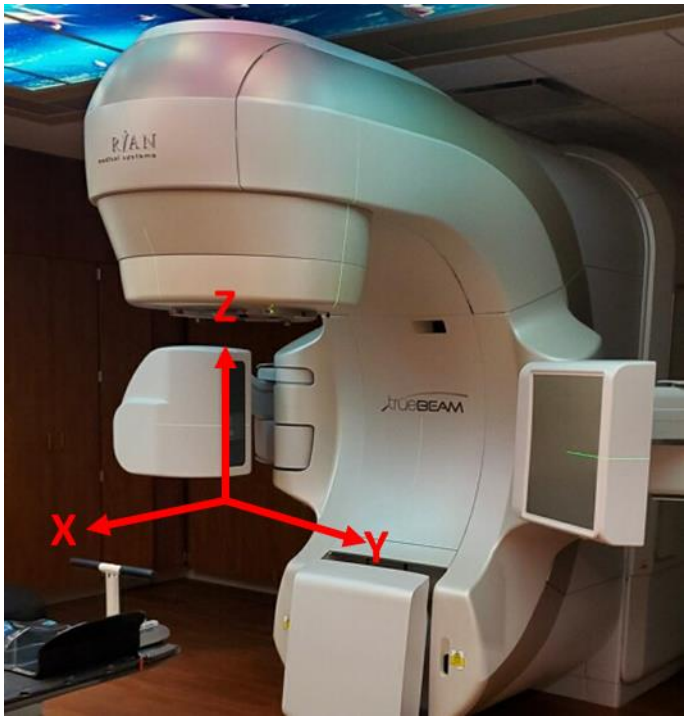

Figure 46: In-room coordinate system used for structure rotations in the Matlab code.

The treatment angles for each beam were found by looking through the DICOM RT Plan file for the appropriate DICOM tag and extracting the values. Rotational matrices were created based on the angles and the in-room coordinate directions. Matrix multiplication is non-commutative, so it was very important to perform the rotations in the correct order. The correct order for the rotations was couch, followed by gantry. Collimator rotations were not performed as the IMRT QA dose planes were calculated at their planned collimator angles. Gantry rotations were performed around the x-axis (Figure 46), and couch rotations were performed around the z-axis (Figure 46). The matrices used to calculated the beams-eye-view structure coordinates ($\vec{P}'$) from the DICOM structure coordinates ($\vec{P}_o$,) using gantry (ϑ), and couch angles (γ) are shown in Equation 17.

With the coordinates transformed into beams-eye-view projections, the poly2mask function was used to create a 3-dimensional high-resolution matrix with ones inside of the contours and zeros outside of the contours. To save memory space, the matrix was created with the data type uint8. Matlab will

automatically create matrices with a double-precision floating-point value type which occupies 64bits of memory per entry, while uint8 only occupies 8 bits, allowing the high-resolution memory allocation to be reduced by a factor of eight.

$$\vec{P}' = \vec{R}_{gantry}\vec{R}_{couch}\vec{P}_o, \text{ where}$$

$$\vec{P}_o = \begin{bmatrix} x_o \\ y_o \\ z_o \end{bmatrix}$$

$$\vec{R}_{gantry}(\vartheta) = \begin{bmatrix} \cos\vartheta & 0 & \sin\vartheta \\ 0 & 1 & 0 \\ -\sin\vartheta & 0 & \cos\vartheta \end{bmatrix} \tag{17}$$

$$\vec{R}_{couch}(\gamma) = \begin{bmatrix} \cos\gamma & -\sin\gamma & 0 \\ \sin\gamma & \cos\gamma & 0 \\ 0 & 0 & 1 \end{bmatrix}$$

Finally, the x-y planes of the 3-Dimensional matrix were combined to effectively "add" the structures in the beams-eye-view. The planes were combined by interpolating each plane to the final resolution of the DICOM dose fields that were to be used in the gamma analysis (0.586mm/pixel). Each interpolation included a scaling factor for the structures that account for the divergence of the beam. The final result of all these calculations, were 2-dimensional matrices that contained the thickness of the spinal cord and PTV structures at each point in the beam, with the matrices centered on the central axis of the field.

The code was created and tested in an object-oriented fashion, however to evaluate the overall end-to-end process, a simple test case was created. This test case consisted of two offset box contours, with dimensions of (2cm x 4cm x 2cm). Three fields were created with different couch and gantry rotations (Figure 47).

For each of the fields, the four structure edges were calculated and compared to the expected values. The average difference between calculated and expected edges was 0.41mm +/- 0.16mm. These

inaccuracies come from the limitations in pixel size and the contour generations from the finite set of axial-shape coordinates in the DICOM structure files.

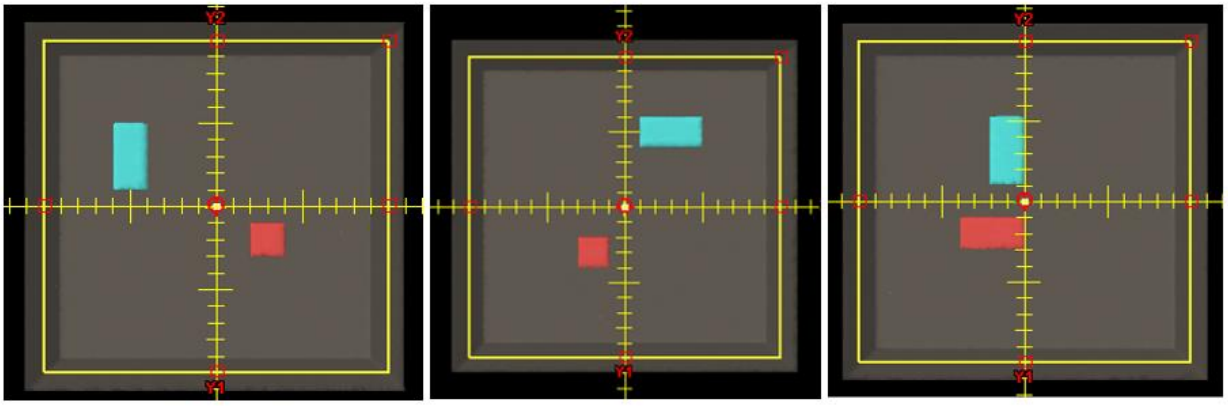

Figure 47: Test fields and structures used to perform end-to-end testing on structure rotation Matlab code.

Pixel sizes were one of the main limitations of this research in that there were constant tradeoffs between accuracy and memory (which sometimes went hand in hand with speed). The manipulation of contours was extremely difficult. The programming solution that was selected was designed to take advantage of the matrix-manipulation functions in Matlab. However, this meant that the matrices had to be large enough to cover the structures while they rotated in three dimensions and large enough to maintain a high resolution. Throughout the coding process, internal functions were built to down sample the matrix size and save memory by using different data types (float, int8, etc.) to lower the bit-per-pixel. Although the Matlab solution produced a workable solution for research, due to the memory issues, it is recommended that any clinical implementation of this research would use a different programming technique that may involve a different language.

REFERENCES

1. M. J. K. Osterman and J. A. Martin, National Vital Statistics Reports **63** (6) (2014).

2. N. Howlader, A. M. Noone, M. Krapcho, D. Miller, K. Bishop, S. F. Altekruse, C. L. Kosary, M. Yu, J. Ruhl and Z. Tatalovich, in *2016-02-16]. http://seer. cancer. gov/csr* (2016).

3. R. Siegel, J. Ma, Z. Zou and A. Jemal, CA Cancer J Clin **64** (1), 9-29 (2014).

4. L. W. Brady and T. E. Yaeger, *Encyclopedia of radiation oncology*. (Springer, Heidelberg, 2013).

5. T. R. Munro and C. W. Gilbert, Br J Radiol **34**, 246-251 (1961).

6. G. A. Ezzell, J. M. Galvin, D. Low, J. R. Palta, I. Rosen, M. B. Sharpe, P. Xia, Y. Xiao, L. Xing, C. X. Yu, I. subcommitte and A. R. T. committee, Med Phys **30** (8), 2089-2115 (2003).

7. N. H. Barth, Int J Radiat Oncol Biol Phys **18** (2), 425-431 (1990).

8. M. Goitein, Int J Radiat Oncol Biol Phys **18** (2), 489-491 (1990).

9. S. Webb, Phys Med Biol **34** (10), 1349-1370 (1989).

10. E. G. Aird, Phys Med Biol **34** (10), 1345-1348 (1989).

11. A. Brahme, J. E. Roos and I. Lax, Phys Med Biol **27** (10), 1221-1229 (1982).

12. J. A. Purdy, E. E. Klein and D. A. Low, Semin Radiat Oncol **5** (2), 156-165 (1995).

13. A. D. Corlan, (WebCite, 2004), Vol. 2014.

14. J. V. Rawson and A. L. Pelletier, American family physician **88** (5), 312-316 (2013).

15. J. F. Barrett and N. Keat, Radiographics **24** (6), 1679-1691 (2004).

16. W. A. Kalender, R. Hebel and J. Ebersberger, Radiology **164** (2), 576-577 (1987).

17. O. Christianson, J. J. Chen, Z. Yang, G. Saiprasad, A. Dima, J. J. Filliben, A. Peskin, C. Trimble, E. L. Siegel and E. Samei, Radiology **275** (3), 725-734 (2015).

18. M. J. Murphy, J. Balter, S. Balter, J. A. BenComo, Jr., I. J. Das, S. B. Jiang, C. M. Ma, G. H. Olivera, R. F. Rodebaugh, K. J. Ruchala, H. Shirato and F. F. Yin, Med Phys **34** (10), 4041-4063 (2007).

19. P. J. Keall, G. S. Mageras, J. M. Balter, R. S. Emery, K. M. Forster, S. B. Jiang, J. M. Kapatoes, D. A. Low, M. J. Murphy, B. R. Murray, C. R. Ramsey, M. B. Van Herk, S. S. Vedam, J. W. Wong and E. Yorke, Med Phys **33** (10), 3874-3900 (2006).

20. S. M. Marcu, Q. J. Wu, K. Pillai and M. S. Weinhous, Medical physics **27** (9), 2146-2149 (2000).

21. N. Rochet, F. Sterzing, A. Jensen, J. Dinkel, K. Herfarth, K. Schubert, M. Eichbaum, A. Schneeweiss, C. Sohn and J. Debus, Strahlentherapie und Onkologie **184** (3), 145-149 (2008).

22. E. E. Wilcox, G. M. Daskalov, H. Lincoln, R. C. Shumway, B. M. Kaplan and J. M. Colasanto, Int J Radiat Oncol Biol Phys **77** (1), 277-284 (2010).

23. Y. Mori, N. Kaneda, M. Hagiwara and T. Ishiguchi, Cureus **8** (11) (2016).

24. M. Oliver, W. Ansbacher and W. A. Beckham, J Appl Clin Med Phys **10** (4), 3068 (2009).

25. B. Mzenda, K. V. Mugabe, R. Sims, G. Godwin and D. Loria, J Appl Clin Med Phys **15** (5), 4787 (2014).

26. M. Snyder, R. Halford, C. Knill, J. N. Adams, T. Bossenberger, A. Nalichowski, A. Hammoud and J. Burmeister, J Appl Clin Med Phys **17** (3), 190-202 (2016).

27. J. L. Bedford, P. J. Childs, V. Nordmark Hansen, M. A. Mosleh-Shirazi, F. Verhaegen and A. P. Warrington, Br J Radiol **76** (903), 163-176 (2003).

28. H. Oguchi and Y. Obata, Med Phys **36** (1), 261-269 (2009).

29. S. Deshpande, V. K. Sathiyanarayanan, J. Bhangle, K. Swamy and S. Basu, J Med Phys **32** (2), 51-55 (2007).

30. I. Eldesoky, E. M. Attalla, W. M. Elshemey and M. S. Zaghloul, J Appl Clin Med Phys **13** (2), 3742 (2012).

31. A. Ahnesjo, M. Saxner and A. Trepp, Med Phys **19** (2), 263-273 (1992).

32. J. W. Wong and R. M. Henkelman, Med Phys **9** (4), 521-530 (1982).

33. R. Jeraj, P. J. Keall and J. V. Siebers, Phys Med Biol **47** (3), 391-407 (2002).

34. X. Jia, X. Gu, J. Sempau, D. Choi, A. Majumdar and S. B. Jiang, Phys Med Biol **55** (11), 3077-3086 (2010).

35. C. Men, X. Gu, D. Choi, A. Majumdar, Z. Zheng, K. Mueller and S. B. Jiang, Phys Med Biol **54** (21), 6565-6573 (2009).

36. O. N. Vassiliev, T. A. Wareing, J. McGhee, G. Failla, M. R. Salehpour and F. Mourtada, Phys Med Biol **55** (3), 581-598 (2010).

37. K. Bush, I. M. Gagne, S. Zavgorodni, W. Ansbacher and W. Beckham, Med Phys **38** (4), 2208-2221 (2011).

38. D. Good, J. Lo, W. R. Lee, Q. J. Wu, F. F. Yin and S. K. Das, Int J Radiat Oncol Biol Phys **87** (1), 176-181 (2013).

39. A. Pugachev and L. Xing, International Journal of Radiation Oncology Biology Physics **54** (5), 1565-1574 (2002).

40. L. Shao, presented at the Proceedings of the 40th Annual Conference of the Operational Society of New Zealand, pp 255–265, 2005 (unpublished).

41. H. Chen, D. L. Craft and D. P. Gierga, Medical Dosimetry **39** (1), 64-73 (2014).

42. T. J. Jordan and P. C. Williams, Phys Med Biol **39** (2), 231-251 (1994).

43. J. M. Galvin, A. R. Smith and B. Lally, International Journal of Radiation Oncology Biology Physics **25** (2), 181-192 (1993).

44. M. S. Huq, I. J. Das, T. Steinberg and J. M. Galvin, Physics in medicine and biology **47** (12), 155-159 (2002).

45. J. M. Paul, R. F. Koch and P. C. Philip, Med Phys **12** (4), 424-430 (1985).

46. J. L. Robar and B. G. Clark, Med Phys **26** (10), 2144-2150 (1999).

47. F. Mihai and A. Gheorghiu, presented at the 7th Conference on Nuclear and Particle Physics, Sharm El-Sheikh, Egypt, 2009 (unpublished).

48. A. Niroomand-Rad, C. R. Blackwell, B. M. Coursey, K. P. Gall, J. M. Galvin, W. L. McLaughlin, A. S. Meigooni, R. Nath, J. E. Rodgers and C. G. Soares, Med Phys **25** (11), 2093-2115 (1998).

49. J. G. Li, G. Yan and C. Liu, J Appl Clin Med Phys **10** (2), 2942 (2009).

50. S. A. Syamkumar, S. Padmanabhan, P. Sukumar and V. Nagarajan, Med Dosim **37** (1), 53-60 (2012).

51. M. Markovic, S. Stathakis, P. Mavroidis, I. A. Jurkovic and N. Papanikolaou, Med Phys **41** (5), 051704 (2014).

52. A. Van Esch, T. Depuydt and D. P. Huyskens, Radiother Oncol **71** (2), 223-234 (2004).

53. J. Thoelking, Y. Sekar, J. Fleckenstein, F. Lohr, F. Wenz and H. Wertz, Z Med Phys **26** (3), 200-208 (2016).

54. J. L. Bedford, Y. K. Lee, P. Wai, C. P. South and A. P. Warrington, Phys Med Biol **54** (9), N167-176 (2009).

55. G. Li, Y. Zhang, X. Jiang, S. Bai, G. Peng, K. Wu and Q. Jiang, Phys Med **29** (3), 295-303 (2013).

56. D. A. Low, W. B. Harms, S. Mutic and J. A. Purdy, Med Phys **25** (5), 656-661 (1998).

57. H. Li, L. Dong, L. Zhang, J. N. Yang, M. T. Gillin and X. R. Zhu, Med Phys **38** (12), 6730-6741 (2011).

58. S. Bresciani, A. Di Dia, A. Maggio, C. Cutaia, A. Miranti, E. Infusino and M. Stasi, Med Phys **40** (12), 121711 (2013).

59. J. H. Song, M. J. Kim, S. H. Park, S. R. Lee, M. Y. Lee, D. S. Lee and T. S. Suh, J Appl Clin Med Phys **16** (6), 263-272 (2015).

60. J. M. Steers and B. A. Fraass, Med Phys **43** (4), 1982 (2016).

61. D. Rajasekaran, P. Jeevanandam, P. Sukumar, A. Ranganathan, S. Johnjothi and V. Nagarajan, Rep Pract Oncol Radiother **20** (1), 57-65 (2015).

62. J. M. Moran, J. Radawski and B. A. Fraass, J Appl Clin Med Phys **6** (2), 62-73 (2005).

63. A. J. Olch, Med Phys **39** (1), 81-86 (2012).

64. B. Allgaier, E. Schüle and J. Würfel, PTW White Pap, D913 (2013).

65. A. Barateau, J. Mesgouez, D. Autret, M. Bremaud, C. Di Bartolo, S. Dufreneix and C. Legrand, Physica Medica **32**, 264 (2016).

66. S. Hughes, J. McClelland, S. Tarte, D. Lawrence, S. Ahmad, D. Hawkes and D. Landau, Radiotherapy and Oncology **91** (3), 336-341 (2009).

67. J. J. Nuyttens, J. B. Prevost, J. Praag, M. Hoogeman, R. J. Van Klaveren, P. C. Levendag and P. M. Pattynama, Acta Oncol **45** (7), 961-965 (2006).

68. R. Wagman, E. Yorke, E. Ford, P. Giraud, G. Mageras, B. Minsky and K. Rosenzweig, International Journal of Radiation Oncology Biology Physics **55** (3), 659-668 (2003).

69. P. Cherry and A. Duxbury, *Practical radiotherapy: Physics and equipment*. (John Wiley & Sons, 2009).

70. A. J. Olch, L. Gerig, H. Li, I. Mihaylov and A. Morgan, Med Phys **41** (6), 061501 (2014).

71. A. Wambersie and T. Landgerg, ICRU Publ Bethesda MD (1999).

72. N. Hodapp, Strahlenther Onkol **188** (1), 97-99 (2012).

73. T. Bortfeld, K. Jokivarsi, M. Goitein, J. Kung and S. B. Jiang, Phys Med Biol **47** (13), 2203-2220 (2002).

74. S. B. Jiang, C. Pope, K. M. Al Jarrah, J. H. Kung, T. Bortfeld and G. T. Chen, Phys Med Biol **48** (12), 1773-1784 (2003).

75. C. X. Yu, D. A. Jaffray and J. W. Wong, Phys Med Biol **43** (1), 91-104 (1998).

76. G. Bouilhol, M. Ayadi, S. Rit, S. Thengumpallil, J. Schaerer, J. Vandemeulebroucke, L. Claude and D. Sarrut, Physica Medica **29** (4), 333-340 (2013).

77. L. A. Dawson, K. K. Brock, S. Kazanjian, D. Fitch, C. J. McGinn, T. S. Lawrence, R. K. Ten Haken and J. Balter, International Journal of Radiation Oncology Biology Physics **51** (5), 1410-1421 (2001).

78. A. N. Pedersen, S. Korreman, H. Nystrom and L. Specht, Radiother Oncol **72** (1), 53-60 (2004).

79. S. B. Jiang, Med Dosim **31** (2), 141-151 (2006).

80. D. A. Jaffray, J. H. Siewerdsen, J. W. Wong and A. A. Martinez, Int J Radiat Oncol Biol Phys **53** (5), 1337-1349 (2002).

81. K. J. Ruchala, G. H. Olivera, E. A. Schloesser and T. R. Mackie, Phys Med Biol **44** (10), 2597-2621 (1999).

82. P. J. Keall, E. Colvill, R. O'Brien, J. A. Ng, P. R. Poulsen, T. Eade, A. Kneebone and J. T. Booth, Med Phys **41** (2), 020702 (2014).

83. C. F. Serago, S. J. Chungbin, S. J. Buskirk, G. A. Ezzell, A. C. Collie and S. A. Vora, Int J Radiat Oncol Biol Phys **53** (5), 1130-1138 (2002).

84. B. W. Raaymakers, J. J. Lagendijk, J. Overweg, J. G. Kok, A. J. Raaijmakers, E. M. Kerkhof, R. W. van der Put, I. Meijsing, S. P. Crijns, F. Benedosso, M. van Vulpen, C. H. de Graaff, J. Allen and K. J. Brown, Phys Med Biol **54** (12), N229-237 (2009).

85. Z. Chang, Z. Wang, J. Ma, J. C. O'Daniel, J. Kirkpatrick and F. F. Yin, Radiother Oncol **95** (1), 116-121 (2010).

86. H. Chung, H. Jin, T. S. Suh, J. Palta and S. Kim, presented at the World Congress on Medical Physics and Biomedical Engineering 2006, 2007 (unpublished).

87. S. Laub, M. Snyder and J. Burmeister, J Appl Clin Med Phys **16** (3), 4836 (2015).

88. J. P. Bissonnette, P. A. Balter, L. Dong, K. M. Langen, D. M. Lovelock, M. Miften, D. J. Moseley, J. Pouliot, J. J. Sonke and S. Yoo, Med Phys **39** (4), 1946-1963 (2012).

89. T. Willoughby, J. Lehmann, J. A. Bencomo, S. K. Jani, L. Santanam, A. Sethi, T. D. Solberg, W. A. Tome and T. J. Waldron, Med Phys **39** (4), 1728-1747 (2012).

90. S. Dieterich, C. Cavedon, C. F. Chuang, A. B. Cohen, J. A. Garrett, C. L. Lee, J. R. Lowenstein, M. F. d'Souza, D. D. Taylor, Jr., X. Wu and C. Yu, Med Phys **38** (6), 2914-2936 (2011).

91. D. A. Low, J. M. Moran, J. F. Dempsey, L. Dong and M. Oldham, Med Phys **38** (3), 1313-1338 (2011).

92. K. M. Langen, N. Papanikolaou, J. Balog, R. Crilly, D. Followill, S. M. Goddu, W. Grant, 3rd, G. Olivera, C. R. Ramsey, C. Shi and A. T. Group, Med Phys **37** (9), 4817-4853 (2010).

93. S. H. Benedict, K. M. Yenice, D. Followill, J. M. Galvin, W. Hinson, B. Kavanagh, P. Keall, M. Lovelock, S. Meeks, L. Papiez, T. Purdie, R. Sadagopan, M. C. Schell, B. Salter, D. J. Schlesinger, A. S. Shiu, T. Solberg, D. Y. Song, V. Stieber, R. Timmerman, W. A. Tome, D. Verellen, L. Wang and F. F. Yin, Med Phys **37** (8), 4078-4101 (2010).

94. E. F. Jackson, M. J. Bronskill, D. J. Drost, J. Och, R. A. Pooley, W. T. Sobol and G. D. Clarke, American Association of Physicists in Medicine. One Physics Ellipse College Park (2010).

95. E. E. Klein, J. Hanley, J. Bayouth, F. F. Yin, W. Simon, S. Dresser, C. Serago, F. Aguirre, L. Ma, B. Arjomandy, C. Liu, C. Sandin and T. Holmes, Med Phys **36** (9), 4197-4212 (2009).

96. G. A. Ezzell, J. W. Burmeister, N. Dogan, T. J. LoSasso, J. G. Mechalakos, D. Mihailidis, A. Molineu, J. R. Palta, C. R. Ramsey, B. J. Salter, J. Shi, P. Xia, N. J. Yue and Y. Xiao, Med Phys **36** (11), 5359-5373 (2009).

97. F.-F. Yin, J. Wong, J. Balter, S. Benedict, J. Craig, L. Dong, D. Jaffray, S. B. Jiang, S. Kim and C. M. Ma, Report of AAPM Task Group **104** (2009).

98. T. C. Zhu, A. Ahnesjo, K. L. Lam, X. A. Li, C. M. Ma, J. R. Palta, M. B. Sharpe, B. Thomadsen, R. C. Tailor and A. T. P. C. T. Group, Med Phys **36** (11), 5261-5291 (2009).

99. I. J. Das, C. W. Cheng, R. J. Watts, A. Ahnesjo, J. Gibbons, X. A. Li, J. Lowenstein, R. K. Mitra, W. E. Simon and T. C. Zhu, Med Phys **35** (9), 4186-4215 (2008).

100. S. Pai, I. J. Das, J. F. Dempsey, K. L. Lam, T. J. Losasso, A. J. Olch, J. R. Palta, L. E. Reinstein, D. Ritt and E. E. Wilcox, Med Phys **34** (6), 2228-2258 (2007).

101. I. J. Chetty, B. Curran, J. E. Cygler, J. J. DeMarco, G. Ezzell, B. A. Faddegon, I. Kawrakow, P. J. Keall, H. Liu, C. C. Ma, D. W. O. Rogers, J. Seuntjens, D. Sheikh-Bagheri and J. V. Siebers, Med Phys **34** (12), 4818-4853 (2007).

102. A. W. Lightstone, S. H. Benedict, F. J. Bova, T. D. Solberg and R. L. Stern, Med Phys **32** (7Part1), 2380-2398 (2005).

103. E. Yorke, R. Alecu, L. Ding, D. Fontenla, A. Kalend, D. Kaurin, M. E. Masterson-McGary, G. Marinello, T. Matzen and A. Saini, Report of Task Group **62** (2005).

104. N. Papanikolaou, J. J. Battista, A. L. Boyer, C. Kappas, E. Klein, T. R. Mackie, M. Sharpe and J. Van Dyk, AAPM Task Group **65**, 1-142 (2004).

105. S. Mutic, J. R. Palta, E. K. Butker, I. J. Das, M. S. Huq, L. N. Loo, B. J. Salter, C. H. McCollough and J. Van Dyk, Med Phys **30** (10), 2762-2792 (2003).

106. M. G. Herman, J. M. Balter, D. A. Jaffray, K. P. McGee, P. Munro, S. Shalev, M. Van Herk and J. W. Wong, Medical Physics **28** (5), 712-737 %@ 2473-4209 (2001).

107. A. R. T. Committee and A. Boyer, *Basic applications of multileaf collimators*. (American Association of Physicists in Medicine Madison, 2001).

108. P. R. Almond, P. J. Biggs, B. M. Coursey, W. F. Hanson, M. S. Huq, R. Nath and D. W. Rogers, Med Phys **26** (9), 1847-1870 (1999).

109. B. Fraass, K. Doppke, M. Hunt, G. Kutcher, G. Starkschall, R. Stern and J. Van Dyke, Med Phys **25** (10), 1773-1829 (1998).

110. W. U. Laub and T. Wong, Med Phys **30** (3), 341-347 (2003).

111. J. U. Würfel, Med Phys Intl J **1** (1), 81-90 (2013).

112. A. J. D. Scott, A. E. Nahum and J. D. Fenwick, Medical physics **35** (10), 4671-4684 (2008).

113. R. Alfonso, P. Andreo, R. Capote, M. S. Huq, W. Kilby, P. Kjall, T. R. Mackie, H. Palmans, K. Rosser, J. Seuntjens, W. Ullrich and S. Vatnitsky, Med Phys **35** (11), 5179-5186 (2008).

114. G. S. Ibbott, D. S. Followill, H. A. Molineu, J. R. Lowenstein, P. E. Alvarez and J. E. Roll, Int J Radiat Oncol Biol Phys **71** (1 Suppl), S71-75 (2008).

115. A. Molineu, N. Hernandez, T. Nguyen, G. Ibbott and D. Followill, Med Phys **40** (2), 022101 (2013).

116. S. McClelland, 3rd, C. Degnin, Y. Chen, G. A. Watson and J. J. Jaboin, J Neurooncol **145** (1), 159-165 (2019).

117. B. Sidiqi, N. Sheth, A. Lee, J. Safdieh and D. Schreiber, J Radiosurg SBRT **5** (3), 201-207 (2018).

118. H. S. M. Park, E. H. Wang, C. E. Rutter, C. D. Corso, V. L. Chiang and J. B. Yu, International Journal of Radiation Oncology• Biology• Physics **93** (3), E62 %@ 0360-3016 (2015).

119. C. D. Corso, H. S. Park, A. C. Moreno, A. W. Kim, J. B. Yu, Z. A. Husain and R. H. Decker, Am J Clin Oncol **40** (4), 358-361 (2017).

120. E. E. Klein, J. Hanley, J. Bayouth, F. F. Yin, W. Simon, S. Dresser, C. Serago, F. Aguirre, L. Ma, B. Arjomandy, C. Liu, C. Sandin, T. Holmes and A. A. o. P. i. M. Task Group, Med Phys **36** (9), 4197-4212 (2009).

121. E. Borzov, A. Nevelsky, R. Bar-Deroma and I. Orion, BJR| Open **1** (1), 20180026 %@ 20182513-20189878 (2019).

122. P. Rowshanfarzad, H. L. Riis, S. J. Zimmermann and M. A. Ebert, Br J Radiol **88** (1051), 20140581 (2015).

123. A. Clivio, E. Vanetti, S. Rose, G. Nicolini, M. F. Belosi, L. Cozzi, C. Baltes and A. Fogliata, Radiat Oncol **10**, 97 (2015).

124. W. Du, S. Gao, X. Wang and R. J. Kudchadker, Med Phys **39** (4), 2156-2162 (2012).

125. P. Rowshanfarzad, C. K. McGarry, M. P. Barnes, M. Sabet and M. A. Ebert, Radiat Oncol **9**, 249 (2014).

126. Y. Zhang, K. Ding, G. Cowan, E. Tryggestad, E. Armour and K. K. Wang, J Appl Clin Med Phys **16** (6), 314-324 (2015).

127. W. Lutz, K. R. Winston and N. Maleki, Int J Radiat Oncol Biol Phys **14** (2), 373-381 (1988).

128. P. Wootton, P. R. Almond, J. G. Holt, D. B. Hughes, D. Jones, C. J. Karzmark and R. J. Schulz, Medical Physics **2** (3), 110-121 %@ 0094-2405 (1975).

129. G. Narayanasamy, D. Saenz, W. Cruz, C. S. Ha, N. Papanikolaou and S. Stathakis, J Appl Clin Med Phys **17** (1), 179-191 (2016).

130. D. Letourneau, M. Gulam, D. Yan, M. Oldham and J. W. Wong, Radiotherapy and Oncology **70** (2), 199-206 (2004).

131. O. A. Zeidan, S. A. L. Stephenson, S. L. Meeks, T. H. Wagner, T. R. Willoughby, P. A. Kupelian and K. M. Langen, Medical Physics **33** (11), 4064-4072 (2006).

132. A. Van Esch, T. Depuydt and D. P. Huyskens, Radiother Oncol **71** (2), 223-234 (2004).

133. D. A. Low, W. B. Harms, S. Mutic and J. A. Purdy, Medical Physics **25** (5), 656-661 (1998).

134. A. C. Cohen Jr., Journal of the American Statistical Association **44** (248), 518-525 (1949).

135. G. W. Weibull, Cc/Eng Tech Appl Sci (10), 18-18 (1981).

136. A. C. Cohen Jr., Technometrics **1** (3), 217-237 (1959).

137. I. J. Myung, J Math Psychol **47** (1), 90-100 (2003).

138. I. D. Currie, Appl Stat-J Roy St C **44** (3), 379-394 (1995).

139. A. C. Cohen Jr., Technometrics **7** (4), 579-588 (1965).

140. J. Venselaar, H. Welleweerd and B. Mijnheer, Radiotherapy and Oncology **60** (2), 191-201 (2001).

141. J. Palta, S. Kim, J. Li and C. Liu, *Intensity-Modulated Radiation Therapy: The State of the Art*. (2003).

142. H. Lilliefors, Journal of the American Statistical Association **62** (318), 399-402 (1967).

143. J. W. Evans, R. A. Johnson and D. W. Green, edited by U. S. D. o. Agriculture (U.S. Government Printing Office, 1989).

144. B. R. Billmann, C. E. Antle and L. J. Bain, Technometrics **14** (4), 831-840 (1972).

145. H. Hirose, Ieee T Dielect El In **6** (1), 66-68 (1999).

146. A. Gago-Arias, L. Brualla-Gonzalez, D. M. Gonzalez-Castano, F. Gomez, M. S. Garcia, V. L. Vega, J. M. Sueiro and J. Pardo-Montero, Physics in medicine and biology **57** (7), 2005-2020 (2012).

147. Z. Allibhai, M. Taremi, A. Bezjak, A. Brade, A. J. Hope, A. Sun and B. C. Cho, International journal of radiation oncology, biology, physics **87** (5), 1064-1070 (2013).

148. I. J. Das, G. X. Ding and A. Ahnesjo, Medical physics **35** (1), 206-215 (2008).

149. G. Wickman and H. Nystrom, Physics in medicine and biology **37** (9), 1789-1812 (1992).

150. K. J. Stewart, A. Elliott and J. P. Seuntjens, Physics in medicine and biology **52** (11), 3089-3104 (2007).

151. B. Johansson, G. Wickman and J. Bahar-Gogani, Physics in medicine and biology **42** (10), 1929-1938 (1997).

152. E. Chung, S. Davis and J. Seuntjens, Medical physics **40** (6), 062104 (2013).

153. E. Johansson, J. Andersson, L. Johansson and H. Tolli, Physics in medicine and biology **58** (12), 4225-4236 (2013).

154. J. Pardo-Montero and F. Gomez, Physics in medicine and biology **54** (12), 3677-3689 (2009).

155. H. Tolli, R. Sjogren and M. Wendelsten, Physics in medicine and biology **55** (15), 4247-4260 (2010).

156. J. Andersson, E. Johansson and H. Tolli, Medical physics **39** (8), 4775-4787 (2012).

157. C. Martens, C. De Wagter and W. De Neve, Physics in medicine and biology **46** (4), 1131-1148 (2001).

158. B. Poppe, T. S. Stelljes, H. K. Looe, N. Chofor, D. Harder and K. Willborn, Medical physics **40** (8), 082106 (2013).

159. C. K. McGarry, B. F. O'Connell, M. W. Grattan, C. E. Agnew, D. M. Irvine and A. R. Hounsell, Med Phys **40** (9), 091707 (2013).

160. K. B. Pulliam, J. Y. Huang, R. M. Howell, D. Followill, R. Bosca, J. O'Daniel and S. F. Kry, Medical physics **41** (2), 021710 (2014).

161. S. H. Benedict, K. M. Yenice, D. Followill, J. M. Galvin, W. Hinson, B. Kavanagh, P. Keall, M. Lovelock, S. Meeks, L. Papiez, T. Purdie, R. Sadagopan, M. C. Schell, B. Salter, D. J. Schlesinger, A. S. Shiu, T. Solberg, D. Y. Song, V. Stieber, R. Timmerman, W. A. Tome, D. Verellen, L. Wang and F. F. Yin, Medical physics **37** (8), 4078-4101 (2010).

162. J. I. Kim, S. Y. Park, H. J. Kim, J. H. Kim, S. J. Ye and J. M. Park, Radiation oncology **9** (2014).

163. B. E. Nelms, H. Zhen and W. A. Tome, Med Phys **38** (2), 1037-1044 (2011).

164. P. R. Storchi, L. J. van Battum and E. Woudstra, Phys Med Biol **44** (12), 2917-2928 (1999).

165. G. M. Clark, R. A. Popple, P. E. Young and J. B. Fiveash, Int J Radiat Oncol Biol Phys **76** (1), 296-302 (2010).

166. Y. Mori, N. Kaneda, M. Hagiwara and T. Ishiguchi, Cureus **8** (11), e882 (2016).

167. T. Gevaert, F. Steenbeke, L. Pellegri, B. Engels, N. Christian, M. T. Hoornaert, D. Verellen, C. Mitine and M. De Ridder, Radiat Oncol **11**, 13 (2016).

168. Y. Huang, K. Chin, J. R. Robbins, J. Kim, H. Li, H. Amro, I. J. Chetty, J. Gordon and S. Ryu, Radiother Oncol **112** (1), 128-132 (2014).

169. I. J. Das, C. W. Cheng, R. J. Watts, A. Ahnesjo, J. Gibbons, X. A. Li, J. Lowenstein, R. K. Mitra, W. E. Simon, T. C. Zhu and T. G. o. t. T. P. C. o. t. AAPM, Med Phys **35** (9), 4186-4215 (2008).

170. S. Dieterich and G. W. Sherouse, Med Phys **38** (7), 4166-4173 (2011).

171. I. Paddick, J Neurosurg **93 Suppl 3**, 219-222 (2000).

172. I. Paddick and B. Lippitz, J Neurosurg **105 Suppl**, 194-201 (2006).

173. M. Chea, K. Fezzani, J. Jacob, M. Cuttat, M. Croisé, J.-M. Simon, L. Feuvret, C.-A. Valery, P. Maingon and M.-A. Benadjaoud, Radiation Oncology **16** (1), 1-16 (2021).

174. H. Liu, D. W. Andrews, J. J. Evans, M. Werner-Wasik, Y. Yu, A. P. Dicker and W. Shi, Front Oncol **6**, 26 (2016).

175. P. K. Sneed, J. Mendez, J. G. Vemer-van den Hoek, Z. A. Seymour, L. Ma, A. M. Molinaro, S. E. Fogh, J. L. Nakamura and M. W. McDermott, J Neurosurg **123** (2), 373-386 (2015).

176. J. C. Flickinger, D. Kondziolka, L. D. Lunsford, A. Kassam, L. K. Phuong, R. Liscak and B. Pollock, Int J Radiat Oncol Biol Phys **46** (5), 1143-1148 (2000).

177. J. Hofmaier, R. Bodensohn, S. Garny, I. Hadi, D. F. Fleischmann, M. Eder, Y. Dinc, M. Reiner, S. Corradini, K. Parodi, C. Belka and M. Niyazi, Radiat Oncol **14** (1), 103 (2019).

178. M. Taylor, J. Williams and J. F. Gleason, Jr., Cureus **12** (8), e9833 (2020).

179. H. Palmans, P. Andreo, M. S. Huq, J. Seuntjens and K. Christaki, Vienna: International Atomic Energy Agency (2017).

180. B. Casar, E. Gershkevitsh, I. Mendez, S. Jurkovic and M. S. Huq, Med Phys **46** (2), 944-963 (2019).

181. H. Chung, H. Jin, T. Suh, J. Palta and S. Kim, presented at the World Congress on Medical Physics and Biomedical Engineering 2006, 2007 (unpublished).

182. J. Roper, V. Chanyavanich, G. Betzel, J. Switchenko and A. Dhabaan, Int J Radiat Oncol Biol Phys **93** (3), 540-546 (2015).

183. T. Gevaert, D. Verellen, B. Engels, T. Depuydt, K. Heuninckx, K. Tournel, M. Duchateau, T. Reynders and M. De Ridder, Int J Radiat Oncol Biol Phys **83** (1), 467-474 (2012).

ABSTRACT

AN INVESTIGATION OF UNCERTAINTIES IN INTENSITY MODULATED RADIATION THERAPY

by

CORY KNILL

December 2021

Advisor: Dr. Jay Burmeister

Major: Medical Physics

Degree: Doctor of Philosophy

Introduction: The treatment of cancer using intensity modulated radiation therapy (IMRT) is complex, involving many sub-processes to commission a treatment platform and treat patients. Uncertainties within the individual sub-process can lead to inaccurate treatments and sub-optimal patient outcomes. This research focused on minimizing uncertainties throughout IMRT commissioning and treatments. **Methods:** Five sub-processes were selected for uncertainty reduction: 1) optimizing radiation-imaging coincidence of the treatment machine, 2) improving the statistical model used to analyze IMRT commissioning data, 3) reducing the effect of ion recombination in IMRT quality assurance measurements, 4) improving the correlation between IMRT quality assurance results and patient-specific delivery inaccuracies, 5) commissioning of cranial stereotactic radiosurgery treatments. **Results:** Uncertainty reduction was achieved in all five sub-processes. Although the effect of this work on any single patient's treatment is difficult to quantify, it is expected that the improvement in the sub-process accuracy will have a beneficial effect on the overall IMRT treatment delivery accuracy. **Conclusion:** Reducing uncertainties is an important aspect of radiotherapy quality assurance and should continue to be investigated for current and future treatment techniques.

AUTOBIOGRAPHICAL STATEMENT

Cory Knill is the Lead Medical Physicist at Beaumont Health's Dearborn campus. He has worked as a medical physicist in radiation oncology for over 10 years. His areas of interest include the commissioning, quality assurance, and delivery of IMRT treatments with a focus on SRS/SBRT. He led the development and implementation of a linac-based cranial SRS service at Beaumont that includes: single-target multi-isocenter, cranial VMAT, and cones treatments. Cory Knill holds a B.S. degree in Physics and a B.A. degree in Mathematics from the University of Michigan, Ann Arbor. He earned his M.S. degree in Radiological Physics from Wayne State University, Detroit in 2010 and his board certification in Therapeutic Medical Physics in 2014.